Study of functional metallic nano/microstructures for photonics applications

A thesis submitted for the degree of
Doctor of Philosophy

by

Md Muntasir Hossain

Centre for Micro-Photonics
Faculty of Engineering and Industrial Sciences
Swinburne University of Technology
Melbourne, Australia

Principal supervisor: Professor Min Gu

2012

Dedicated to my beloved parents

Declaration

I, Md Muntasir Hossain, declare that this thesis entitled:

"Study of functional metallic nano/microstructures for photonics applications"

is my own work and has not been submitted previously, in whole or in part, in respect of any other academic award.

Md Muntasir Hossain

Centre for Micro-Photonics
Faculty of Engineering and Industrial Sciences
Swinburne University of Technology
Australia

Dated this day, August 24, 2012

Abstract

The manipulation of electromagnetic (EM) radiation and moulding its flow at the nanoscale dimensions are some of the pioneering research fields of physics in the current century. Photonics has now emerged as the vital medium for the development of photovoltaics and future information communication systems. For the rapid progress in these fields of photonics, efficiently manipulating light at the nanoscale dimensions is the primary issue. Artificially designed novel photonic nano/microstructures can serve as the key elements for controlling EM radiations in a desired manner, which have potential applications in the rapid development of photovoltaics.

Photonic crystals (PCs) are such kind of photonic dielectric microstructures which are able to control and manipulate the flow of light and are very promising materials in nanophotonics applications. These artificially designed periodic microstructures possess photonic band gaps (PBGs) and are optical equivalent to semiconductors comprising electronic energy band gaps. When one of the constituent materials of PCs is replaced with a metal rather than a dielectric they form metallic photonic crystals (MPCs). The optical properties of MPCs are quite distinctive than those of PCs. MPCs contain large and complete PBGs along with resonant optical absorption within the photonic band edge. These attractive

features have made MPCs very promising materials for tailored thermal radiation and their potential application lies within thermo-photovoltaics.

However, to efficiently exploit the promising aspects of MPCs it is very important to thoroughly characterise the intriguing optical properties of MPCs with structural and material parameters. Thorough theoretical studies of EM interactions of light within the MPC environment and band structure properties can explain their dispersive properties and resonant absorption. The tunability of the strength and spectral position of the enhanced absorption within the MPCs is a crucial condition for achieving modified thermal emission.

To realise the potential applications of MPCs for tailored thermal emission, the fabrication of high quality three-dimensional (3D) MPCs is essential. However, the fabrication of such quality of MPCs with low fabrication cost is also another important challenge. Although there are several methods available for achieving 3D MPCs with state-of-the-art lithographic technologies, stringent and expensive fabrication processes have limited them to be considered for practical applications in thermo-photovoltaics. Some less expensive fabrication methods were also demonstrated; however, limitations of realising MPCs of arbitrary geometries and inability of shifting the operating wavelength of the microstructures into the optical wavelengths were the major drawbacks.

As one of the major aim of this thesis, the resonant absorptive properties of 3D woodpile MPCs have been thoroughly investigated for their potential applications in thermo-photovoltaics. We have presented a detailed theoretical work on the optimisation of the bandwidth, magnitude and spectral position of the resonant absorptions in 3D woodpile MPCs based on extensive numerical simulations and band structure calculations. Our results could be of importance for the design of efficient thermal emitters.

We have also demonstrated a novel and low cost fabrication method for realising 3D MPCs operating in the optical wavelength region. Our fabrication method has

also the ability to realise MPCs with arbitrary geometries and a range of different metals. To achieve high quality 3D MPCs we have employed a direct laser writing (DLW) method for the fabrication of 3D woodpile dielectric PCs. Using the multiple laser scanning method with experimentally determined fabrication conditions dielectric woodpile PC templates with appropriate filling ratio were achieved. The electrodeposition method was successfully employed for the infiltration of metals into the 3D dielectric templates. This combination of a DLW method and an electrochemical method allowed us realising high quality 3D inversed woodpile MPCs. The developed MPC structures possess resonant optical absorption peaks which can be of significance for modified thermal radiation emission.

The optical properties of the fabricated high quality 3D MPCs were also investigated experimentally. The MPC structures possess unique features of multiple enhanced absorption peaks in the optical wavelengths over a broad wavelength range along with high reflection spectra. The optical properties of the fabricated MPCs were further analysed with detailed theoretical calculations and good agreements were found with the experimental results. Our fabrication method is thus very promising for realising high quality MPCs for modified thermal radiation applications. In addition, the MPC structures possess optical absorptions with plasmon resonances which could be interesting for applications in plasmonic solar cells.

Information and communication are vital parts of the modern world where photonics can definitely play an intriguing role for the future development. The demand for faster telecommunications devices is increasing at a much higher rate than the current technology can offer. The semiconductor electronics based current telecommunications technology will clearly not be able to accept the challenge. On the other hand, photonics offer to revolutionise the information communications sector with ultrafast speed. However, it is difficult to manipulate photons, (i.e. EM radiations) at the nanoscale for information processing.

To employ photons as the information carrier introduction of novel artificial plasmonic nanostructures is one of the most promising solutions. Plasmonics is the novel field of photonics which deals with the interactions of light with the free charge oscillations on a metal surface. Plasmonics allows the control of EM radiation even at the deep subwavelength scale and has received great attention within the wider photonics community. Subwavelength plasmonic waveguides are very promising to be used as the platform for developing miniaturised nanophotonic chips.

However, to utilise the promise of plasmonics for desired nanophotonic applications, one needs to design plasmonic waveguides with the combination of some unique optical properties such as subwavelength mode confinement, complete energy confinement and high nonlinearity. Total energy confinement within subwavelength plasmonic waveguides ensures the zero cross-talk between adjacent nanophotonic components. Optical nonlinearity is another crucial feature for the realisation of all-optical signal processing. However, the major problem of most of the plasmonic waveguides demonstrated is the inability of combining all these important criteria. Unfortunately, the scope of the nonlinearity within plasmonic waveguides is even rarely discussed in the earlier research studies.

As the other major aim of this thesis, a new kind of plasmonic waveguide geometries comprising a subwavelength nonlinear core and a metallic nanoshell has been reported theoretically. The nanoshell plasmonic waveguide exhibits deep subwavelength mode confinement with nearly 100% energy residing within the waveguide. Another important aspect is the demonstration of an ultrahigh Kerr nonlinearity up to $4.1\times10^{4}W^{-1}m^{-1}$ at the telecommunication wavelength of 1.55 μm within this subwavelength nanoshell plasmonic waveguides. The ultrahigh nonlinear nature was also analysed in terms of the vectorial mode profiles and the dispersive properties of the plasmonic waveguide. The combination of the complete mode confinement properties and the ultrahigh Kerr nonlinearity within

a single device has made the nonlinear nanoshell plasmonic waveguide an ideal candidate as a primary element in integrated nanophotonic circuits.

Along with the theoretical studies, we have also provided the experimental demonstration of nanoshell plasmonic waveguides. For the fabrication of such waveguides we have adopted the DLW method to fabricate dielectric nanorods and electroless silver deposition method to deposit a thin layer of silver film on to the dielectric nanorods. The propagation of plasmon modes within the nanoshell plasmonic waveguides has been experimentally demonstrated.

The theoretical and experimental works conducted in this thesis have focused on the studies of functional metallic nano/microstructures for applications in two major areas of photonics. Firstly, the resonant absorptive properties of 3D MPCs have been thoroughly investigated for their potential applications in thermo-photovoltaics. Secondly, a novel class of nonlinear nanoshell subwavelength plasmonic waveguides comprising total energy confinement and ultrahigh nonlinearity has been studied which has promising applications in future high speed telecommunications systems.

Acknowledgements

After completing my undergraduate studies in physics I decided to perform higher studies by research. My own interest in optics and nanoscale physics drove me to choose nanophotonics as my research area. While I was looking for a postgraduate research opportunity in a suitable topic in nanophotonics I came to know about the pioneering photonics research in the Centre for Micro-Photonics (CMP) at Swinburne University of Technology (SUT) from their website. I contacted the Director of the CMP, Professor Min Gu informing him my research interest. I was privileged to get a doctoral research opportunity at the CMP under the supervision of Professor Min Gu. I would like to thank and express my sincere gratitude to him for not only for accepting my PhD candidature under his supervision but also for the continuous guidance, invaluable supervision and encouraging me to think independently.

I would like to express my gratitude to my co-supervisors Dr. Guangyong Zhou and Dr. Baohua Jia for assisting me with their valuable experiences and expertise. Many thanks go to Dr. Michael James Ventura for his helps on laboratory equipment and useful discussions at the early stage of my PhD studies. I would like to thank Dr. Dario Buso, Dr. Joel Van Embden and Dr. Alessandro Antonello for their help and useful discussions on laboratory works related to chemistry. My thanks go to our collaborators Mr. Gengyan Chen and Professor Xue-Hua Wang for their contributions to the theoretical characterisation of metallic photonic

crystals and to Dr. Alessandro Antonello for his contribution to the electroless silver coating.

I would like to thank all the members of the Centre for Ultrahigh-bandwidth Devices for Optical Systems (CUDOS) for useful discussions and help during my entire PhD studies. Special thanks go to Dr. Jiafang Li for his help on laboratory equipment training and useful discussions. I would like to express my special thanks to Mr. Mark Turner for many useful discussions on physics during my doctoral research. I would like to thank Dr. Elisa Nicoletti for her assistance in writing with LATEX. Thanks go to all the other CUDOS students (Mr. Benjamin Cumming, Mr. Han Lin, Mr. Zongsong Gan) for sharing their valuable experiences and knowledge.

My thanks also go to all the CMP student colleagues (Dr. Peter Zijlstra, Dr. Brendan Chick, Dr. Jing Wu, Mr. Wei Tao, Ms. Hong Kang, Mr. Stephen Weber, Dr. Xingyu Gao, Mr. Adam Taylor, Mr. Jingzhi Wu) and staff members (Dr. Xiangping Li, Dr. Dru Morrish, Dr. James Chon, Associate Prof. Xiaosong Gan, Dr. Betty Kouskousis, Dr. Jing Liang Li, Dr. Hongchun Bao, Dr. Daniel Day) for providing a friendly and learning environment.

I would also like to express my acknowledgement to SUT, the CMP, and the CUDOS for providing scholarship, other financial supports and world class laboratory facilities for my doctoral studies. I would like to thank the Swinburne Optics and Laser Laboratories (SOLL) technician Mr. Mark Kivinen for all the custom opto-mechanical works. Thanks go to the administrative staff Ms. Johanna Lamborn, Ms. Jia Lou and Ms. Barbara Gillespie for their help with the official paperwork and other general tasks during my PhD candidature.

In particular, I would like to express my earnest gratitude to my beloved family for their support, understanding and great encouragement. My PhD research would not have been possible without the support of my parents. My special thanks go to my mom for her continuous support and endless love. Thanks go to

my elder brother Mr. Mohammad Monzur Hasan for strongly supporting my endeavour for higher studies by research after completing my undergraduate studies.

Finally, my thanks go to all of those who supported my research studies by any means during my PhD candidature.

Md Muntasir Hossain
Melbourne, Australia
August 24, 2012

Contents

List of Figures

List of Tables

List of abbreviations

EM	Electromagnetic
PC(s)	Photonic crystal(s)
PBG	photonic band gap
MPC(s)	Metallic photonic crystals(s)
3D	Three-dimensional
DLW	Direct laser writing
SP(s)	Surface plasmon(s)
DOS	Photonic density of states
NIR	Near infrared
FCC	Face-centred-cubic
SEM	Scanning electron microscope
SPP(s)	Surface plasmon polariton(s)
SNOM	Scanning near-field optical microscope
DC	Direct current
PWE	Plane-wave expansion
FDTD	Finite-difference time-domain
FIT	Finite integration technique

FDFD	Finite-difference frequency-domain
CVD	Chemical vapour deposition
CPP	Channel plasmon polariton
WPP	Wedge plasmon polariton
FCT	Face-centred-tetragonal
IR	Infrared
FTIR	Fourier transform infrared
2PP	Two-photon polymerisation
2PA	Two-photon absorption
NA	Numerical aperture
NIR	Near infrared
OPO	Optical parametric oscillator
CCD	Charge-coupled device
ALD	Atomic layer deposition
ITO	Indium-tin-oxide
RPHT	Retarded plasmon hybridisation theory
VNSE	Vectorial-based nonlinear Schrodinger equation

Chapter 1

Introduction

Over the last few decades the applications of photonics in the energy and communications sectors have seen a revolutionary progress. Photonics, i.e. the science of generation and manipulation of light has emerged as one of the most rapidly increasing areas of science and engineering. The use of photons in the renewable energies; i.e. photovoltaics, is a rapidly expanding resource in the energy sector. The ever increasing demand of global energy consumption has steered the necessity of renewable energy sources, of which photovoltaics is one of the most potential candidates. Photovoltaics is a method where photon energies are converted to electrical energy via semiconductor photovoltaic cells. Photovoltaics is now a very attractive and active research branch of photonics.

On the other hand, although semiconductor electronics have played a breakthrough role in information and communication technology in the 20^{th} century, its current progress for faster communication speed and higher energy efficiency is quickly approaching saturation. To achieve a breakthrough in these fields, photonics is a potential solution. Photons (light) are faster information carriers with the capability of possessing ultrahigh bandwidth and higher energy efficiency in comparison to electrons. Artificially engineered photonic nano/microstructures and their assembly on a single platform are believed to be

able to realise the so called integrated photonic chips which could replace the semiconductor electronic chip and revolutionise the telecommunications sector with ultrahigh communication speed, large optical band width, nanoscale photonic components, diverse functionality, and higher energy efficiency.

One of the key points for the development of functional photonic nano/microstructures is the applications of photonics to achieve rapid progress in photovoltaics and telecommunications. Photonics crystals (PCs) are such a class of novel microstructures which has the capability to mould the flow of light. PCs are a special kind of structures which are composed of a periodic modulation of dielectric materials. When wavelengths of the electromagnetic (EM) radiations (photons) are comparable to the length scale of the periodicity, it can introduce photonic band gaps (PBGs) and thus inhibit the propagation of light. In 1987, individual theoretical researches by Yablonovitch [1] and John [2] have predicted, for the first time, the special optical properties of PCs for manipulating photons. Since then, immediate attention has been paid by the researchers from around the world on PCs to explore their potential applications. The ability to control the flow of light enables PCs to offer prospective applications in communications, biophotonics, and quantum optics etc. PCs were later on realised with metals rather than dielectrics and named as metallic PCs (MPCs). MPCs contain some more distinctive features than PCs such as resonant optical absorption along with large PBGs. This provides MPCs the ability of tailoring thermal radiation emission and enables potential applications in thermo-photovoltaics.

Plasmonics, i.e. surface plasmons (SPs) based nanophotonics, on the other hand, is another exciting branch of photonics which deals with the interaction of light with the free conduction electronic charges at the metal surfaces. SPs are the collective and bound oscillations of electrons at a metal surface [3]. SPs can couple with light and propagate along the metal-dielectric interface. SPs are even able to surpass PCs for manipulating light at nanoscale dimensions. The bound nature of SPs to the metal surfaces enables plasmonic nanostructures to confine

EM waves beyond the diffraction limit. Plasmonics is thus the true element to realise subwavelength integrated nanophotonic components i.e. the photonic circuits. One major aspect of plasmonics is that it offers the possibility of merging photonics and electronics on the same platform in nanoscale dimensions [4]. Plasmonics also allows localising and focusing EM modes in small area or volume which has potential applications for nanoscale biosensors [5]. Efficient light trapping by nanoplasmonic structures can also yield resonant optical absorption which is also promising for solar energy harvesting in photovoltaic applications [6].

MPCs and plasmonics are very exciting research areas within photonics. This chapter is a basic introduction to PCs and plasmonics with a brief theoretical introduction of their background. A brief comparison between the dielectric PCs and MPCs is discussed and followed by the potential applications of MPCs. A brief discussion on SPs of flat metal-dielectric interfaces is presented and also the diverse applications of plasmonic waveguides are also provided. The objective and outline of this thesis are presented at the end of this chapter.

1.1 Introduction to photonic crystals

Two immediate applications that were proposed directly after the discovery of PCs were inhibition of spontaneous emission [1] and localisation of photons [2]. However, the unique optical property of PCs to control the flow of light enables them to have many possible applications, for example, superprisms [7, 8], photonic chips for integrated optics [9, 10], beam splitters and waveguides [11, 12] etc. Another promising aspect of PCs is that they are not fundamentally limited to any length scale. As long as the length scale of the periodic dielectric modulation of the PC structure is comparable to the operating wavelength it preserves its unique properties i.e. the PBGs [13].

1.1.1 Basics of photonic crystals

PCs are periodic microstructures of alternating low and high dielectric constants [13]. When propagating through the PCs, EM waves face the periodic refractive index mismatches, which produce a forbidden frequency band for EM waves. The photonic density of states (DOS) vanishes for that spectral band and creates a PBG [2, 14-16]. When EM radiations within the band are not allowed to propagate for all the incident directions, the PC possesses a complete PBG [13]. Within the photonic allowed or pass bands, oscillations in photonic DOS lead to transmission resonances inside the PC [17, 18]. PCs are in somewhat analogous to semiconductors that exhibit electronic band gaps where electrons experience periodic Coulomb potential through the interactions with atomic nuclei. However, the main differences are the structural sizes and the operating wavelengths. For semiconductors the scale of the lattice constant for the atoms or molecules is on the order of angstroms for electronic band gaps in the visible to near infrared (NIR) wavelengths where PCs have their lattice constants on the order comparable to the operating wavelengths.

For an isotropic, nondispersive and nonmagnetic media without any nonlinear contribution of the dielectric response, solving the corresponding macroscopic Maxwell's equations lead to the wave equation

$$\nabla \times \left(\frac{1}{\varepsilon(\mathbf{r})} \nabla \times \mathbf{H}(\mathbf{r}) \right) = \left(\frac{\omega}{c} \right)^2 \mathbf{H}(\mathbf{r}), \tag{1.1}$$

where $\mathbf{H}(\mathbf{r})$ is the macroscopic magnetic field and $\varepsilon(\mathbf{r})$ is the relative permittivity or dielectric constant of the media. Equation 1.1 governs the EM wave propagation within the media. For any composite material or arbitrary structure with known $\varepsilon(\mathbf{r})$ solving the wave equation results in the modes $\mathbf{H}(\mathbf{r})$ and the corresponding frequencies.

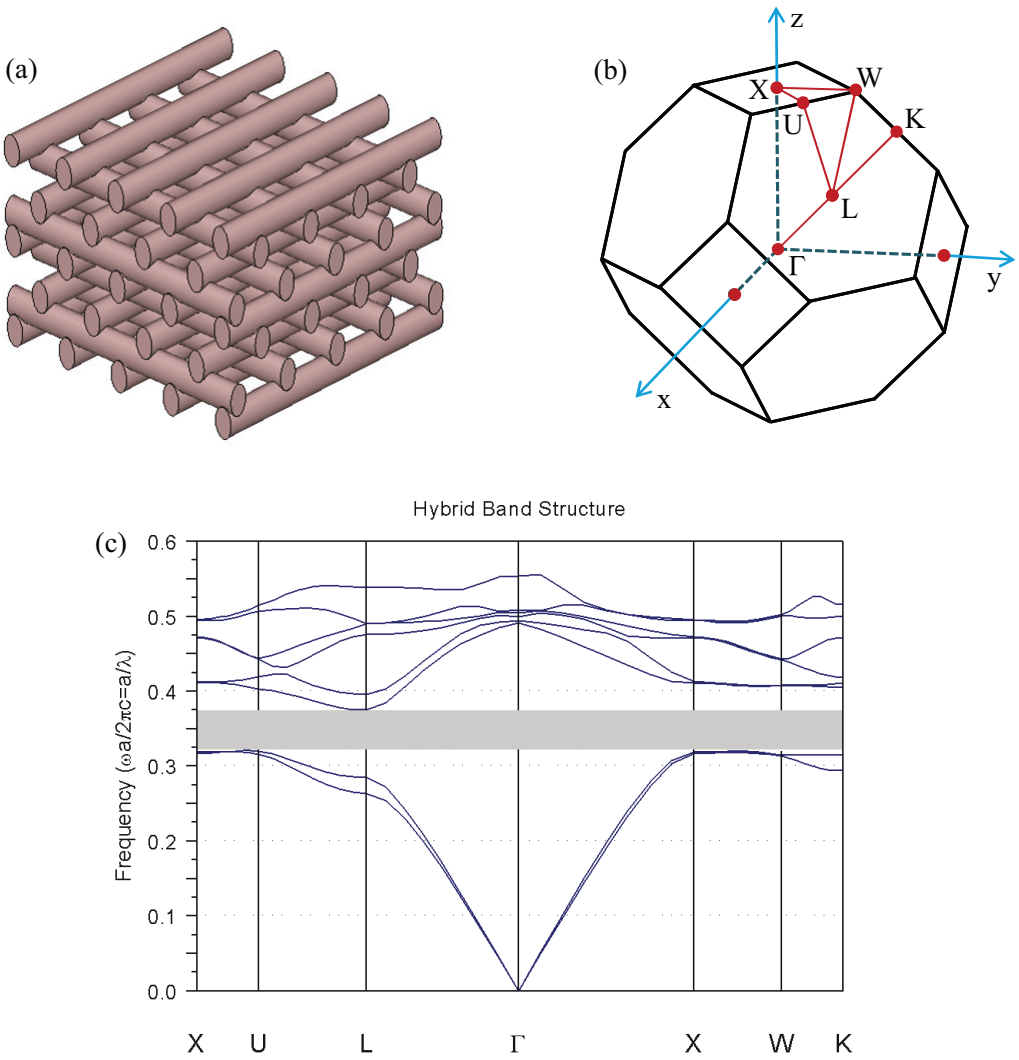

Fig. 1.1 (a) Sketch of a 3D dielectric woodpile PC. (b) The first Brillouin zone for a face-centred-cubic (FCC) structure. (c) The calculated band structure of a woodpile PC. The structure consists of dielectric elliptic rods with 0.3 µm width and 0.5 µm height. The dielectric refractive index is 3.45 and the background is air. The in-layer lattice constant is 1 µm. The structure exhibits a complete PBG where the normalised frequency of the mid-gap position is about 0.35. The band diagram was calculated with the commercially available R-Soft software.

The dielectric constant inside the PC is distributed in a periodic form. Thus this can be expressed as $\varepsilon(\mathbf{r}) = \varepsilon(\mathbf{r}+\mathbf{R})$, where is the **R** the lattice vector in real space which defines the periodic properties inside the PC. PCs are classified as one-dimensional (1D), two-dimensional (2D) and three-dimensional (3D) according to the dimension of **R**. This is analogous to the case of semiconductors where

electrons experience periodic potentials. For semiconductors, the crystal lattice is specified by the Fourier space i.e. the wavevector (**k**) space and the Coulomb potential is expressed with Bloch periodic function. The electronic states are analysed by the quantum mechanical treatment and electronic band gaps are defined with the so called Brillouin zones formed by the reciprocal lattice vectors in the Fourier space [19]. The same conventions are adopted in electrodynamics to find out the modes inside the PCs because of the periodic nature of the dielectric properties of the constituent materials of the PCs. The mode profile of the PCs can be described by the first Brillouin zone, i.e. the primitive cell within the reciprocal lattice [13]. The modes of 3D PCs can be labelled by the Bloch wavevector **k**. The wavevector **k** is associated with the eigenvector $\mathbf{H_k}$ of the form $\mathbf{H_k} = e^{i\mathbf{k}.\mathbf{r}}\mathbf{u_k}(\mathbf{r})$ [13]. The wave equation 1.1 inside the PC thus leads to

$$(i\mathbf{k} + \boldsymbol{\nabla}) \times \frac{1}{\varepsilon(\mathbf{r})} (i\mathbf{k} + \boldsymbol{\nabla}) \times \mathbf{u_k}(\mathbf{r}) = \left(\frac{\omega(\mathbf{k})}{c}\right)^2 \mathbf{u_k}(\mathbf{r}). \quad (1.2)$$

The above equation states an eigen value problem and solutions of the equation results in the eigen modes inside the PC. The first Brillouin is even further reduced by symmetry operations and is termed an irreducible Brillouin zone [13]. Solutions of the above equation within the irreducible Brillouin zone gives rise to discrete sequence of eigenfrequencies $\omega_n(\mathbf{k})$ (n = 1,2,…) for a fixed value of **k**. These eigenfrequencies form series of bands where **k** varies inside the Brillouin zone. The discrete properties of the bands can lead to PBGs i.e. where no propagating modes (ω) can be found. A complete PBG is formed for a range of frequencies when no propagating solutions to Maxwell's equations for all **k** can be found. The PBG properties of a PC mainly depend on the dielectric constant contrast of the materials, geometry and symmetry of the structure and filling ratio (the volume ratio of the high refractive index dielectric material with respect to the whole composite structure).

1.1.2 Metallic photonic crystals

Although PCs are generally fabricated of dielectric materials, there is also emerging interest on the fabrication of metallic photonic crystals (MPCs) and characterisation of their properties. Metals are in general highly dispersive. In case of dielectric material based PCs, the bulk dielectric materials are optically transparent and their dispersive properties are insignificant in general. However, Metals are not optically transparent and the dielectric constant is a complex quantity and a function of frequency. The real part of the permittivity is negative and describes the dielectric properties. The positive imaginary part defines the intrinsic material absorption which leads to an evanescent mode of the propagating EM wave incident on the surface of the metal from a dielectric medium [20, 21]. Thus PCs composed of metals are highly dispersive and contain distinctive features compared to their dielectric counterparts.

Some recent metallic microstructures have attracted attention due to their ability of possessing unusual thermal emission properties [22, 23]. These MPCs, usually woodpile like pattern are found to have large complete PBGs due to high dielectric constant contrast and also enhanced absorption is observed in the photonic band edge. In terms of optical properties MPCs possess some unique features compared to dielectric PCs:

- Highly dispersive in contrast to dielectric PCs
- Extraordinary large and complete band gap
- Finite MPC structures composed with only few layers are capable of complete inhibition of photon propagation
- Possess unusual enhanced absorption in the photonic band edge

1.1.3 Applications of metallic photonic crystals

MPCs have prospective applications in many areas of photonics. In particular, the intriguing feature of MPCs for tailored thermal emission by spectral redistribution has allowed them to be very attractive in energy applications [22, 24]. MPCs were first experimentally realised with ultrawide band gab and enhanced absorption in the photonic band edge by J. G. Fleming *et al*. [25]. It was proposed that these artificial microstructures are capable of suppressing thermal emission completely in the band gap frequency region and recycle the photons in the band edge to have enhanced narrow band thermal emission. Such a kind of MPCs is termed as modified black body emitter. These unique properties allow them to be used as efficient thermal emitters for thermo-photovoltaics. The highly enhanced thermal emission in a selected narrow spectral window thorough the MPC structure can be matched to the electronic band gap of the photovoltaic cell materials and can lead to high efficiency thermo-photovoltaic system. Later, this exceptional thermal emission property of MPCs was experimentally confirmed by several research groups [22, 26]. It was theoretically estimated that with thermal excitation in combination of a woodpile tungsten MPC and a low temperature thermal photovoltaic cell a conversion efficiency of optical to electrical energy of 34% is possible [22].

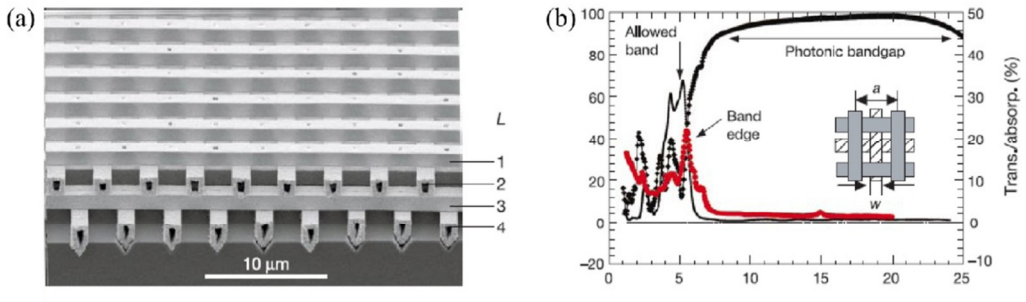

Fig. 1.2 (a) Scanning electron microscope (SEM) image of a 3D tungsten MPC. (b) The measured reflectance (black diamonds), transmission (black circles) and absorption (red circles) spectra for light propagating along the 001 axis. Absorption peak is observed at the band edge of ~ 6 µm [25].

3D MPCs were also demonstrated to act as an efficient light emitter. By electrically heating a tungsten MPC sample S.Y Lin *et al*. demonstrated electrical to optical energy of 44% [27]. Later it was also demonstrated that MPCs can work as efficient incandescent light sources with their unmatchable photon-recycling characteristics [28, 29]. MPCs can also be useful for achieving functional photonic devices. Theoretical studies have demonstrated that MPCs can be useful for realising frequency selective optical filters [30].

MPCs thus have potential applications in areas of photonics. However, the functionality of MPCs depends completely on the control of the resonant absorption peaks associated with the PBGs. Theoretical analysis of the dissipative properties of MPCs related to the geometrical and material properties is thus essential. Moreover, for realistic applications, the development of low cost and efficient novel fabrication methods of MPCs is necessary.

1.2 Introduction to plasmonics

Plasmonics is the field of resonant interactions of light with free surface charges of metal in a metal-dielectric interface. Plasmonics allows the confinement of light into nanoscale dimensions. Plasmonics waveguides are considered as the one of the key elements for the future integrated nanophotonic devices. The recent state-of-the-art advanced micro-fabrication technologies have opened the potential applications of plasmonics in the areas of nanophotonics, biophotonics and materials engineering etc.

1.2.1 Surface plasmons

Metals contain free electron charges (electron gas or plasma) surrounding their atomic lattices. These conduction electrons exhibit collective oscillations which

are termed as plasma oscillations or plasmons [31, 32]. When SPs (i.e. the coherent plasma oscillations at the metal-dielectric interface which are bound to the metal surface [33]) couple with an external EM radiation, the resulting propagating mode emerges as surface plasmon polaritons (SPPs). SPPs are one of the most attractive approaches to achieve subwavelength optical waveguides. While dielectric waveguides are fundamentally limited to have EM mode confinement not beyond the diffraction limit, plasmonic waveguides allow localisation of modes in the subwavelength scale [3].

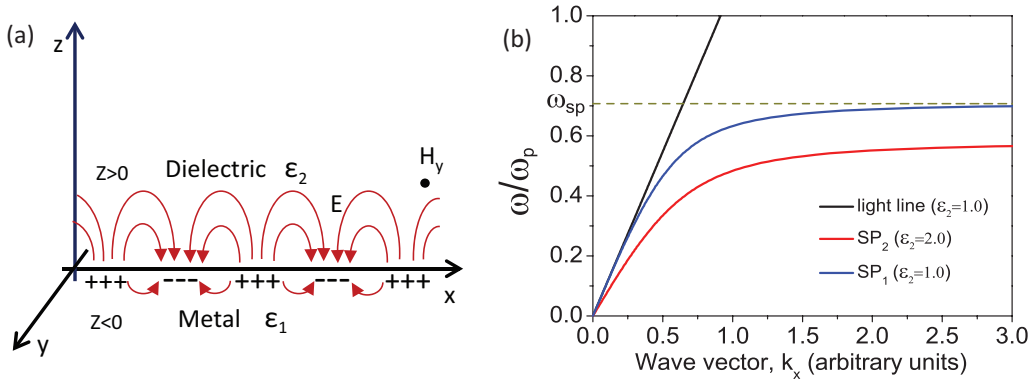

Fig. 1.3 (a) Schematic of the charge distribution and the EM field of the SPs propagating in the x direction at the metal-dielectric interface. The normal component of the field, E_z, is enhanced near the metal surface and decays exponentially with increasing distance from the surface. (b) Dispersion curves for the SPs at the metal surface with two different dielectric media of dielectric constants of 1.0 and 2.0, respectively. The dashed curve shows the maximum SP frequency at the metal-air interface. The SP curve reaches the ω_{sp} limit for large k_x.

In a metal-dielectric interface the field for the surface mode with TM polarisation (as to generate surface charge oscillations in the propagating direction requires electric field normal to the surface) can be described by

$$\mathbf{E} = \mathbf{E}_0^{\pm} \exp\left[i\left(k_x x \pm k_z z - \omega t\right)\right] , \tag{1.3}$$

where + for $z \geq 0$ and – for $z \leq 0$. The imaginary k_z determines the exponential decay of the field component E_z and k_x is parallel to and continuous thorough the

interface [3]. Fig. 1.3(a) shows the schematic of the formation of SPs at the metal dielectric interface with a transverse characteristic of the magnetic field and a mode propagation direction along the x axis. Solving Maxwell's equations with appropriate boundary conditions results in the dispersion relation for the surface mode i.e. the SP mode at the metal-dielectric interface [3, 34]

$$k_x = \frac{\omega}{c}\left(\frac{\varepsilon_1 \varepsilon_2}{\varepsilon_1 + \varepsilon_2}\right)^{1/2}. \tag{1.4}$$

Equation 1.4 states that to achieve real valued k_x with negative permittivity of metal, the condition $|\varepsilon_1|>\varepsilon_2$ needs to be satisfied. Furthermore, the magnitude of the SP wavevector, $k_x>\omega/c$, where, c is the speed of light in the dielectric medium. Hence, to generate SPs in the metal surface, the missing portion of the SP wavevector needs to be supplied along with the incident EM wave [35]. A number of methods are demonstrated to supply the missing the portion of the SP wavevector [35]. These include (a) use of prisms as coupling media for the excitation of SPs which was developed by Kretschmann and Otto [36, 37], (b) scattering from a topological defect on the metal surface [38, 39], and (c) use of periodic corrugation in the metal surface [40]. Fig. 1.3(b) demonstrates the dispersion relation of SPs at the metal-dielectric interfaces for two different dielectric media. The SP curve for the metal-air interface lies at the right side of the light line in air showing the non-radiative nature of the SP. At a low value of k_x, the SP behaves like EM radiation in the dielectric medium with monotonic increase of the SP frequency ω; however, reaches to the asymptotic limit for large k_x. Equation 1.4 states that at a large value of k_x the SP frequency approaches to the maximum value [3]

$$\omega_{sp} = \frac{\omega_p}{\sqrt{1+\varepsilon_2}}, \tag{1.5}$$

where ω_p is the bulk plasma frequency of the metal (see section 2.2.2). For a SP mode at the metal-air interface the relation comes to

$$\omega_{sp} = \frac{\omega_p}{\sqrt{2}}. \tag{1.6}$$

As the dielectric function of metal is a complex quantity, the propagating mode wavevector is also a complex quantity and the imaginary part of k_x determines the propagation length of the SP mode.

For metallic nano/microstructures with specific geometries the plasmon mode can differ than the SPs in the flat metal-dielectric interfaces. Metallic nanostructures can also support localised plasmon modes [41, 42] along with the propagating plasmon modes depending on the structural geometries. For metallic nanoshells, plasmons at the inner and outer surfaces can couple and result hybridisation of plasmons [42, 43] and causes plasmonic extinction. Highly confined plasmon modes are also observed in metallic nanocavities [41].

1.2.2 Plasmonic waveguides and applications in photonics

Over the last decade there has been a surge on SP based nanophotonics. Because of the supreme characteristic of SPs of confining EM modes beyond the diffraction limit plasmonic waveguide based devices have brought unique prospects in integrated nanophotonics [44-46], high resolution optical sensors and imaging systems [47], biophotonics, and photovoltaics [48] etc. The capability of the SPs of channelling light with concentrated EM energies at subwavelength scale has led to the development of planar metallic nanostructures for miniaturised waveguides [49-51]. Plasmonic waveguides are thus ideal for use in photonic chips.

Plasmonic waveguide based devices are currently being explored for nanophotonic components such as optical switches [46, 52], resonators [51], modulators [53, 54] and couplers [55].

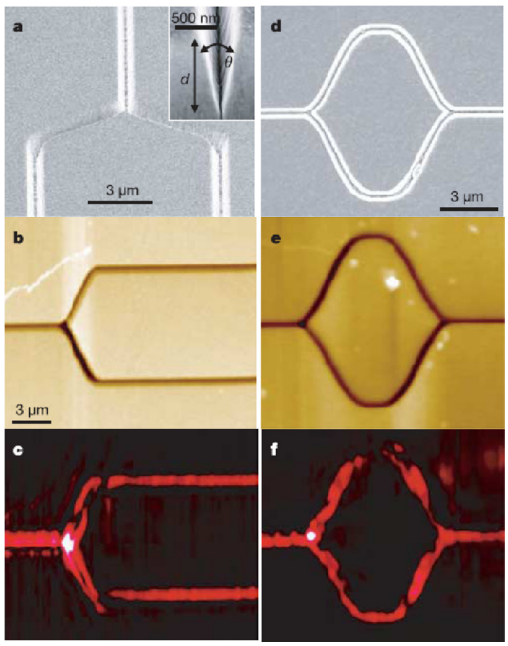

Fig. 1.4 Channel plasmon waveguide components (a) SEM image (b) Topographical image and (c) scanning near-field optical microscope (SNOM) images of a Y-splitter (d–f) Same type of images as (a–c) but for a Mach–Zehnder (MZ) interferometer [51].

Due to the high EM mode confinement, subwavelength plasmonic waveguides are also successfully used to realise plasmonic nano-lasers [56, 57]. Such nanoscale plasmonic structures can lead to the realisation of true integration of nanophotonic components i.e. the integrated nanophotonic circuit.

Miniature plasmonic devices are also very promising for localising light into nanoscale regions. Propagating plasmons are concentrated on specially engineered devices such as tapered plasmonic waveguides [58-60], metallic wedge plasmonic waveguides [50, 61, 62], tapered nanogap plasmonic waveguides [63-65], and tapered transmission lines [5] to yield nanofocusing with highly enhanced fields. Such plasmonic nanofocusing is promising in sensing and imaging applications.

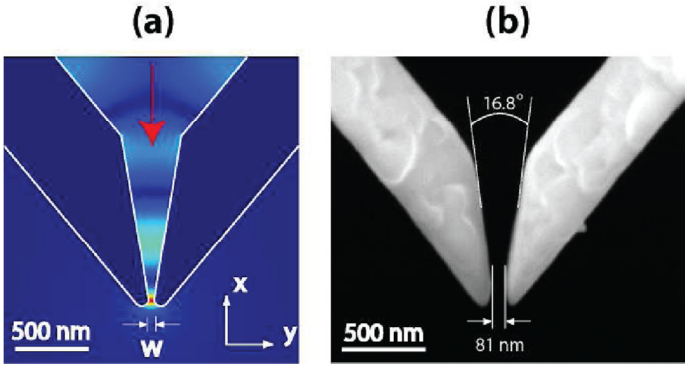

Fig. 1.5 Nanofocusing of light. (a) Calculated electric field intensity, $|\mathbf{E}|^2$, enhancement during nanofocusing in a tapered gap plasmon waveguide. (b) SEM image of the tapered gap plasmon waveguide's cross-section showing the nanogap at the narrow lower region where nanofocusing takes place [63].

Active plasmonics is another emerging field where SPP signals are modulated on plasmonic waveguide based devices. It was first introduced by Krasavin *et al*. [66] where the researchers demonstrated that inducing structural phase change of the plasmonic waveguide can yield effective controls over the SPP signal. The switching time for the SPP signal modulation was estimated to be on the order of picosecond-microsecond scale [66]. Other methods provided optical modulation based on plasmonic excitation of quantum dots [67] and thermo-plasmonic modulation [46] with nanosecond and millisecond switching times respectively.

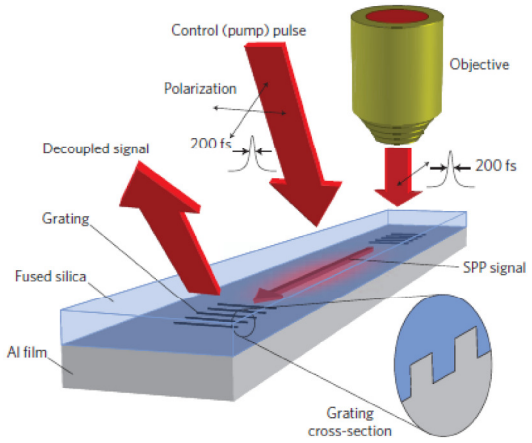

Fig. 1.6 Ultrafast optical modulation of propagating SPP signal. The femtosecond pulses were successfully generated, transmitted, modulated and decoupled for detection on a single device by the researchers [68].

Recently, experimental demonstration of femtosecond modulation of plasmon pulses was achieved on a planar plasmonic waveguide based device where optical pump fluence of about 10 $mJcm^{-2}$ led to around 7.5% modulation of the plasmon wave intensity on an aluminium/silica interface [68].

Plasmonic waveguides have the potential to be used as the building blocks for the realisation of the future nanophotonic chips for ever faster information communication technology. Promising plasmonic waveguide designs with subwavelength confinement have also been successfully demonstrated [49-51, 55, 58]. However, some crucial features such as the total energy confinement for zero-crosstalk and high optical nonlinearity for all-optical signal processing need to be addressed for the successful applications of plasmonic waveguides in integrated nanophotonics.

1.3 Thesis objective

MPCs and plasmonic waveguides have emerged as very attractive areas of nanophotonics research recently for their potential applications in energy and communications. One of the main objectives of this thesis is to thoroughly investigate the optical properties of 3D MPCs by theoretical studies and to realise 3D MPCs by a state-of-the-art nanofabrication method. This is followed by the characterisation of novel plasmonic waveguides for telecommunications applications. The novelty of this thesis lies within the optimisation of the resonant absorption of 3D woodpile MPCs related to their dispersive features and realisation of high quality 3D MPC structures operating in the optical wavelength regime. This is accompanied by the innovation of demonstrating the ultrahigh nonlinearity and the total energy confinement in a novel class of nanoshell subwavelength plasmonic waveguides. We identify some major criteria to be studied thoroughly in achieving our goal:

- Although some theoretical researches to characterise the optical properties of MPCs have been performed in the past, more detailed investigation is necessary to illustrate the optimisation of the band width, magnitude and spectral positions of the enhanced absorption in 3D MPCs for realising practical applications.

- The fabrication method for realising 3D MPCs should be able to produce high quality and promising structures and also cost effective compared to the existing fabrication technologies. Furthermore, most prominent applications of MPCs lay in the infrared (IR) to near infrared (NIR) region. Our fabrication method needs to be able to realise MPCs operating in the NIR region.

- Subwavelength mode confinement in plasmonic waveguides has been demonstrated theoretically and experimentally. However, the total energy confinement within these subwavelength devices is a critical issue to realise zero cross-talk nanophotonic integration which has not been addressed earlier. We demonstrate the total energy confinement in our novel nanoshell plasmonic waveguide.

- The high field confinement within plasmonic waveguides is definitely attractive for nonlinear optics applications but this is not extensively explored. We take this opportunity for investigating the highly nonlinear optical properties of the novel nanoshell plasmonic waveguides.

- Experimental demonstration of nanoshell plasmonic waveguides is also an important issue which needs to be addressed.

1.4 Outline of the thesis

The research conducted in this thesis includes the investigation of the promising optical properties of MPC structures and intriguing features of novel plasmonic waveguides. Experimental studies are focused on the fabrication of 3D and 2D metallic nano/microstructures and their optical characterisation.

Chapter 2 presents a brief review on the optical properties of metals, theoretical modelling and available computational tools for the characterisation of the optical properties of metallic microstructures and existing techniques for the fabrication of metallic microstructures. In particular, Section 2.3 reviews the theoretical investigations on PBG properties and resonant absorptions in 3D MPCs. Section 2.4 discusses the fabrication methods for 3D periodic metallic microstructures. Section 2.5 outlines the novel and functional plasmonic waveguide based devices investigated for telecommunications applications.

Chapter 3 demonstrates the optimisation method for controlling the enhanced optical absorption in 3D woodpile MPCs along with the complete PBG. Section 3.2 introduces the designs of band gap structures considered in this chapter and demonstrates the basic optical properties with numerical calculations. Section 3.3 outlines the theoretical methods used here to calculate the PBG of 3D woodpile MPCs and discusses the effects of dispersive properties on group velocities within the MPCs. Section 3.4 presents the characterisation of the resonant absorption within finite sized 3D MPCs with detailed numerical simulations which relates the results with the dispersive properties and provides the optimisation of the enhanced absorption for different structural and material properties.

Chapter 4 presents the proposed fabrication method in detail for achieving 3D MPCs. Section 4.2 introduces the direct laser writing (DLW) method for realising high quality 3D woodpile polymer PC template structures. This section serves as an introduction for the organic photosensitive resin used here and also provides

the fabrication parameters i.e. the laser power associated with the two-photon polymerisation method and the fabrication speed to realise 3D polymer templates.

The infiltration of metals in polymer PC template structures to realise 3D MPC structures is described in Section 4.3. Particularly, the deposition of nickel by electrodeposition method in conductive substrates and the control of the metal growth for desired nickel film thickness are discussed. Section 4.4 characterises the optical properties of the inversed woodpile 3D MPCs resulting from the metal deposition into the polymer PC templates. In particular, the experimental results for optical absorptions in a wide optical frequency range are compared with the theoretically calculated results. The origin of the enhanced optical absorption within the MPCs is explained in terms of the localised plasmon resonances and the enhanced light-matter interaction at the photonic band edge.

As an important step towards novel plasmonic devices for telecommunications, Chapter 5 investigates the optical properties of a new class of subwavelength plasmonic waveguide based on a metallic nanoshell with an embedded nonlinear dielectric core. Section 5.2 provides the fundamental mode confinement properties of the nanoshell plasmonic waveguide compared to their dielectric counterparts. The unique property of the nanoshell plasmonic waveguide for total energy confinement and the ability of being used as a zero cross-talk subwavelength plasmonic device in integrated nanophotonics are discussed. In Section 5.3.1 we compare the dispersive properties of plasmon modes within the nanoshell plasmonic waveguides with respect to the SPPs in flat metal-dielectric interfaces. The effects of the variation of the metallic nanoshell thickness on the field confinement of the plasmon mode are discussed in Section 5.3.2 and the propagation length characteristics of the nanoshell plasmonic waveguide are presented in Section 5.3.3.

Optical nonlinearity is one of the most intriguing features in emerging small core waveguides. The Kerr nonlinearity strictly depends on the mode confinement of

the waveguide and the nonlinear index coefficient of the constituent waveguide bulk materials. Although plasmonic waveguides possess subwavelength mode confinement by its nature, their potential applications in optical nonlinearity are rarely explored. In Section 5.3 we investigate the scope of the nanoshell plasmonic waveguide as a highly nonlinear optical device. We theoretically demonstrate that the nanoshell plasmonic waveguide with a nonlinear silicon core can possess an ultrahigh Kerr nonlinearity up to $4.1\times10^{4}W^{-1}m^{-1}$.

Chalcogenide glasses are one of the highest nonlinear optical materials. Particularly, arsenic trisulphide (As_2S_3) can be easily structured to yield subwavelength features by the DLW fabrication technique. Chalcogenide glasses are thus could be very attractive for realising nonlinear plasmonic waveguides. In Section 5.4 we investigate the nonlinear optical properties of a nanoshell plasmon waveguide based on a nonlinear chalcogenide glass subwavelength core.

We provide an experimental demonstration of the nanoshell plasmonic waveguides in chapter 6. Sections 6.2 and 6.3 describe the fabrication of 1D polymer nanorod arrays on glass substrate by the DLW method and achieving a thin silver coating on top of the polymer nanorods by electroless silver deposition method. The plasmon modes were characterised with different linearly polarised incident lights. The experimental results were also compared with the theoretical calculations performed with numerical simulations.

Chapter 7 summarises the results obtained in this thesis and provides an outlook into the future work in these fields.

Chapter 2

Review

2.1 Introduction

Photonic crystals (PCs) are specially designed artificial photonic microstructures with periodic variation of refractive indices. When one of the dielectric materials of a PC structure is replaced with a metal, it turns as a metallic photonic crystal (MPC). MPCs and plasmonic waveguides are photonic micro/nanostructures that provide unique properties to control and manipulate the electromagnetic (EM) radiation. These artificially engineered materials have the ability to play significant role in the next generation nanophotonics applications. MPCs have potential applications in thermo-photovoltaics with their unique ability of resonant optical absorption along with complete and wide photonic band gap (PBG). On the other hand, plasmonic waveguides are capable of subwavelength manipulation of light which can act as the building blocks for the development of the future high speed information and communication processing systems and other areas of nanophotonics.

A vast number of theoretical and experimental researches on characterising the optical properties of MPCs and plasmonic waveguides have been undertaken over the last few decades. In this chapter a brief overview on the theoretical and

experimental work performed on characterising the optical properties of MPCs and plasmonic waveguides are presented. The fabrication methods for realising three-dimensional (3D) periodic metallic microstructures operating in the optical wavelengths have been discussed.

2.2 Theoretical tools for metallic microstructures

2.2.1 Optical properties of metals

In the case of dielectric material based PCs, the dispersive properties of the bulk dielectric materials are generally insignificant and material absorption properties is not that substantial. However, metals are not optically transparent and the dielectric constant is a complex quantity and a function of frequency. The real part of the permittivity is negative and describes the dielectric properties. The positive imaginary part defines the intrinsic material absorption which leads to an evanescent mode of propagating electromagnetic (EM) wave incident on the surface the metal from a dielectric medium[20, 21].

The dielectric constant for metals is defined as

$$\varepsilon(\omega) = \varepsilon_r(\omega) + i\varepsilon_i(\omega), \tag{2.1}$$

where $\varepsilon_r(\omega)$ is the real part and $\varepsilon_i(\omega)$ is the imaginary part. The refractive index of a metal is defined as a complex quantity

$$\hat{n} = n + ik, \tag{2.2}$$

where n and k are called the optical constants. The 'Skin depth' of a metal is defined as [20]

$$\delta = c/k\omega, \tag{2.3}$$

where δ is the distance within which the EM field falls to 1/e (63%) of its original value when incident on a metal surface from air. n and k can be expressed by computing real and imaginary parts of complex dielectric constant as [20]

$$n = \sqrt{\frac{1}{2}\left[\varepsilon_r + \sqrt{\varepsilon_r^2 + \varepsilon_i^2}\right]} \tag{2.4}$$

and

$$k = \sqrt{\frac{1}{2}\left[-\varepsilon_r + \sqrt{\varepsilon_r^2 + \varepsilon_i^2}\right]}. \tag{2.5}$$

The real and imaginary parts of the complex dielectric constants vary strongly with frequency. Generally at the microwave and far-infrared frequencies metals act like perfect reflectors with no significant absorptions. However, in the high frequency region, especially in the near infrared (NIR) and visible wavelength regions, rapid change of these dielectric functions is observed and absorption in the material becomes significant. As the optical properties of metals directly depend on these dielectric constants it is desirable to use a theoretical model which fits best with experimentally measured values of the dielectric constants.

2.2.2 Drude model

Drude model describes the features of metals nearly accurate over a wide frequency range and it considers the electrons belonging to the outer atomic orbits of metals are not bound but are free to contribute to direct current (DC) conduction [20]. The real and imaginary parts of the dielectric constants of conductive metals according to this model are [20]

$$\varepsilon_r(\omega) = 1 - \frac{\omega_p^2}{\omega^2 + \omega_\tau^2}, \tag{2.6}$$

and

$$\varepsilon_i(\omega) = \frac{\omega_p^2 \omega_\tau}{\omega\left(\omega^2 + \omega_\tau^2\right)}, \tag{2.7}$$

where ω_p is the plasma frequency, defined as

$$\omega_p = \sqrt{\frac{Ne^2}{\varepsilon_o m}}, \tag{2.8}$$

where N is the density of electrons, e is the electric charge, m is the mass of the electron, and ε_o is the permittivity of free space. ω_τ is the damping frequency or damping constant which is reciprocal of the electron collision time τ in a particular metal,

$$\omega_\tau = \frac{1}{\tau}. \tag{2.9}$$

This classical model characterises the free electrons of the metal as damped harmonic oscillators. The damping rate comes from the collisions of the free charged particles. While oscillating electrons reflect any incident radiation with frequency below the plasma frequency ω_p, the damping causes dissipation of energy over the mean decay time of the oscillating electrons which results absorption of a fraction of the incident radiation. The Drude model fits well for measured experimental data over a wide frequency range in the infrared (IR) and NIR but gives substantial error in the visible region [30, 69]. It has been demonstrated that for visible wavelength region (≥500 nm) the Drude-Lorentz model gives much improved but not perfect result for gold [69]. In this thesis, where more appropriate, experimentally measured optical constants of metals are used for the characterisation of metallic structures.

2.2.3 Computational tools

Solving the eigenvalue problem in the form of equation 1.2 gives rise to eigenmodes and band diagrams. However, numerical tools are needed to solve

Maxwell's equations to achieve such solutions for band diagrams. One common and popular numerical technique is the plane wave expansion (PWE) where the mode function (electric or magnetic fields) is represented in terms of the Fourier series expansion of plane waves from the reciprocal lattice [16]. In a periodic system using the Bloch boundary conditions in the reciprocal lattice this method accurately and efficiently calculates the modes to generate the band diagrams of a three-dimensional (3D) system. However, the operator used in the eigenvalue problem for PWE is Hermitian which yields real and positive values for the calculated modes. In such a case, only materials can be considered which do not have loss as Hermitian operators cannot be used for complex functions. Furthermore, PWE cannot handle material dispersion. As PWE method solves a set of eigenstates (eigenvalues for a number of frequencies) at a certain wavevector **k**, it assumes the refractive index distribution as identical for all the frequencies and thus restrains to consider the material dispersion.

To overcome the limitations of the PWE method the finite-difference time-domain (FDTD) band solver is a good choice. The FDTD method can simultaneously handle the material dispersion and loss.

Band diagrams are useful tools for optical characterisation of MPCs as they provide information about the allowed and forbidden gaps (band gaps). However, certain important features, such as, transmission/reflection and absorption cannot be investigated via band structure calculations. Transmission/reflection spectra are very useful calculations to characterise the MPC structures of finite sizes. For our purpose we use CST MWS Studio which is a commercially available electromagnetic simulator. CST provides both time domain and frequency domain solvers which uses a finite integration technique (FIT) for a finite calculation domain and provides a universal spatial discretisation scheme applicable to various electromagnetic problems. The time domain solver utilises a staircase (hexahedral) mesh cells for computations whereas frequency domain solver can utilise both staircase and tetrahedral mesh cells. The frequency domain solver

with tetrahedral mesh cells is used in this project for all the calculations performed by CST Microwave Studio software.

2.3 Optical properties of three-dimensional metallic photonic crystals

2.3.1 Wide band gap and enhanced absorption

Within the MPC environments, the large discontinuity of the permittivity of the periodic elements and the highly dispersive nature of metals opens ultrawide and complete PBG. It was theoretically demonstrated [70] that in the photonic band edge a gain enhancement is possible. In the band gap region there exists no EM Bloch mode, but in the flat band region i.e. where **k** approaches the band edge or near the band edge, the EM Bloch wave is still extended throughout the structure, its group velocity is low and photonic density of states (DOS) is greatly enhanced. Later N. A. R. Bhat *et al.* [71] theoretically showed that in this frequency regime where the band flattens out, the group velocity is near to zero and the EM waves can behave like standing waves. Such extremely slow light will pass much more time throughout the structure than conventional propagating modes. In such a situation, an enhanced light-matter interaction is expected. In the MPC environment, the result of this phenomenon can lead to the enhanced absorption of light [71, 72]. MPCs later were found to have unusual enhanced absorption in the band edge [25].

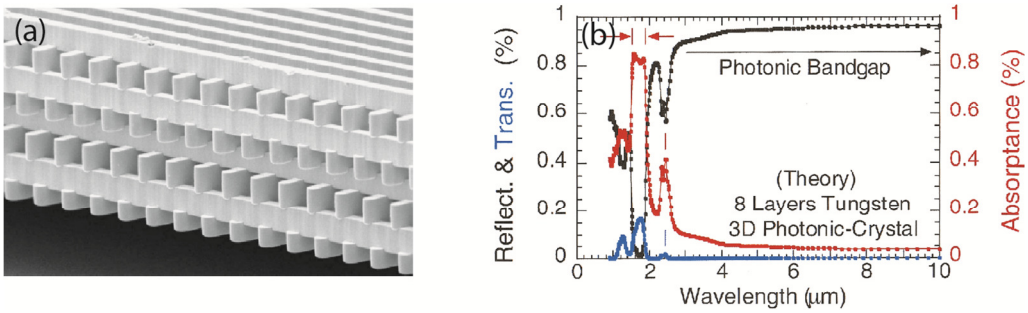

Fig. 2.1 (a) Scanning electron microscope (SEM) image of a 3D tungsten MPC. The rod width is 0.5 μm and the in-layer lattice constant is 2.0 μm. (b) Calculated reflection, transmission and absorption spectra for the 3D tungsten MPC presented in (a). A wide band gap exists starting from 3.0 μm and multiple absorption peaks also arise near the photonic band edge [27].

MPCs were first experimentally realised to have complete PBG and enhanced narrow absorption peak in the band edge by J. G. Fleming *et al.* [25]. The fabricated MPC was made of tungsten and possessed a large band gap with the transmission band at 5 μm. A high absorption peak was found near the band edge at 6 μm. The spectral properties were also compared by theoretical calculations with transfer matrix method. An idea [25] was proposed that if the MPC structure is heated to certain temperature for thermal emission it can suppress the black body thermal emission in the band gap region. Moreover, according Kirchhoff's law of thermal radiation [73], an absorption in a specified region is suggestive to an emission in that region. Therefore, the narrow absorption peak of the MPC in the band edge can act as a selective thermal emission radiation channel with a specified band width. When the MPC is heated to a certain temperature it can suppress the thermal emission in the band gap region and recycle the photons of that band gap region into the band edge or the near band edge resonant absorption region. Such a spectral redistribution of photons can greatly enhance the thermal emission in a selective narrow bandwidth region. Later this unique phenomenon was confirmed by S. Y. Lin *et al.* [22, 23, 74]. MPC structures made of tungsten were heated electrically [22, 74] and thermally [23] and enhanced thermal emission was observed near the photonic band edge. An energy conversion efficiency of 40% was reported from one side of the MPC sample when heated

electrically with external bias voltage [74]. Such a MPC can act as an effective thermal emitter in thermo-photovoltaic system. In a thermo-photovoltaic system the emission properties of the absorber can be modified by placing a MPC with that in thermal contact and the enhanced emission in a narrow selective spectral region by the MPC emitter can be matched with the photovoltaic cell material electronic band gap to significantly increase the conversion power efficiency of the photovoltaic cells.

2.3.2 Characterisation of enhanced absorption in metallic photonic crystals

Optical characterisation of MPCs by theoretical studies is very important for practical applications. For tailored thermal emission, strict control of the resonant absorption and the PBG is necessary. The origin of the resonant absorption and its dependence on the MPC structural parameters, number of layers, and intrinsic dispersive properties of metals were first demonstrated by S. Y. Lin *et al.*

S. Y. Lin *et al.* [72] explained several reasons for the enhancement of the selective narrow band absorption in MPC. The first reason was the anomalous absorption at the photonic band edge or near the band edge. A transmission/reflection calculation was carried out for a tungsten woodpile MPC with finite layers. For a variation of the tungsten metallic rod height h in the MPC structure the absorption and reflection were computed and it was shown that for increasing values of h the band edge position shifted to longer wavelengths. However, over the entire of the variation of h, the absorption resonance was always found to be highly enhanced in the corresponding band edge position. This was attributed to the low group velocity of light at the photonic band edge and longer light-matter interaction.

The second factor which was found to be responsible for the enhanced absorption in MPCs was the number of layers N in the MPC structure. From transfer matrix calculation it was found that the enhanced absorption was independent of the skin

depth of the metal and was attributed to the extended nature of the EM Bloch wave within the greater thickness (layers) of the entire MPC structure. However, the absorption followed an exponential trend for increasing N and was saturated to 60% in magnitude for thickness of 21 μm (14 layers). The saturation of the absorption was attributed to the finite reflection from the air-metal interface of the MPC structure.

The origin of the enhanced absorption within the MPC was attributed to the intrinsic absorption of the bulk metal [72]. As the imaginary part of the dielectric constant $\varepsilon_i(\omega)$ is responsible for the intrinsic absorption within metals, by computing a transfer matrix calculation $\varepsilon_i(\omega)$ was varied from 0 to 100% (its actual value) and the absorption was computed for the tungsten MPC structure [72]. It was found that within the tungsten MPC, the peak absorption in the band edge of the crystal was maximum in the region where $\varepsilon_i(\omega)$ was taken 100% and completely vanishing for $\varepsilon_i(\omega)= 0$ (ignoring the imaginary part of the dielectric constant value). Furthermore, in other previous work [16] the same dependence of the enhanced absorption at the band edge on the variation of $\varepsilon_i(\omega)$ was predicted.

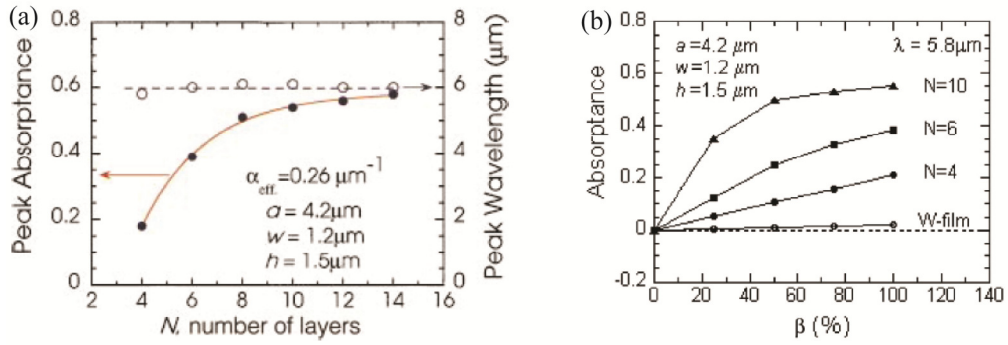

Fig. 2.2 (a) Computed peak absorption of the tungsten MPC as a function of the number of layers N. α_{eff} is the attenuation coefficient in the tungsten MPC. The absorption amplitude increases sharply for increasing layers and saturates for N>12 which demonstrates the continuous absorption of light while propagating through the MPC structure. (b) Peak absorption versus $\beta\varepsilon_i(\omega)$ for different tungsten MPCs. β is a coefficient varied from 0 to 100% and $\varepsilon_i(\omega)$ is the imaginary part of the dielectric constant of tungsten. The open circles indicate the absorption of a uniform tungsten film [72].

G. Veronis *et al.* [75] theoretically showed that flat band or the band edge is necessary but not sufficient for introducing highly enhanced absorption. They have analysed 2D square lattice of metallic cylinders in air with a finite-difference frequency-domain (FDFD) method for a wide range of incident angles. It was demonstrated that such 2D MPCs with metallic cylinders of smaller diameter have more absorption because of the small filling fraction [impedance matching]. This can eventually reduce the finite air-metal reflection and can lead to 99% absorption in the photonic band edge.

Inclusion of dielectrics within the MPCs and their effects on the optical properties was discussed later by H-Yi Sang et al [76]. The dependence of the magnitude and the position of the resonant absorption with respect to the dielectric spacer thickness between the metallic layers of the MPC and the refractive indices of the dielectrics were addressed in their work.

A number of theoretical investigations have been performed on the enhanced absorptions of MPCs. However, the relation of the resonant absorption with the dispersive properties of the MPC itself and its modifications by the alteration of geometrical parameters have not been investigated. Furthermore, the variations of the optical properties of the MPCs for different bulk materials have not been discussed before. We have investigated these thoroughly in Chapter 3.

2.4 Realisation of three-dimensional metallic photonic crystals

There are many experimental approaches which successfully realised 3D MPCs. Among them the main method is to use a 3D dielectric PC as a template and infiltrate metal within it to realise a 3D MPC. There are other approaches which use thin metallic coating onto the dielectric PCs to realise metallodielectric PCs rather than pure MPCs. For practical applications the fabrication cost, structure

quality, ease of operation and capability of large scale fabrication are the important features of the fabrication method. In this section, some of the fabrication methods which were able to realise pure MPC and metallodielectric PC structures are discussed (Table 2.1).

Table 2.1 *3D periodic metallic microstructures fabrication techniques*

Fabrication Techniques	Materials and Structures	Features
Modified silicon process A mould was created by patterning and etching SiO2 layer. Then it was filled with 500 nm thick tungsten film by chemical vapour deposition (**CVD)** and the resulting structure was planarised by chemical mechanical polishing process. The same process was repeated several times to form a multilayer structure. The SiO_2 was removed chemically and a freely standing thin tungsten MPC film remained [27].	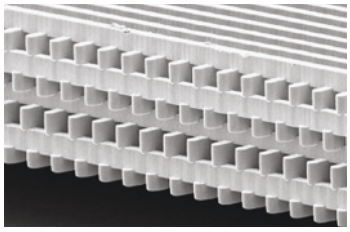 8 layer tungsten woodpile MPC.	1) Structures of different metals and different highly symmetric structures are realisable. 2) Large scale fabrication possible in the woodpile structure. 3) Slow and multi-step time consuming process. 4) Intricate experimental set-up. 5) Expensive fabrication method.

Metal deposition in inverse opal template by electrodeposition Gold was deposited by electrochemical deposition into the fabricated inverse titania opal. Selective removal of titania from the structure forms Opaline gold MPCs [77].	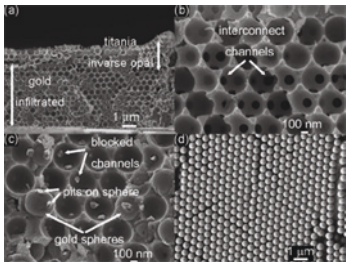 (a) Titania inverse opal template partially filled with gold, (b) unfilled region, (c) gold filled region and (d) Gold opal.	1) Uniform gold infiltration achieved with electrodeposition process. 2) Structures of different metals are realisable. 3) Relatively cheap. 4) Structure contains uncontrolled, unwanted entire defects.
Metal deposition by electrodeposition in polymer woodpile PC structures A polymer woodpile PC template was fabricated by soft lithography. Nickel was deposited into the structure by electrodeposition and the polymer PC template was removed by chemical etching [26].	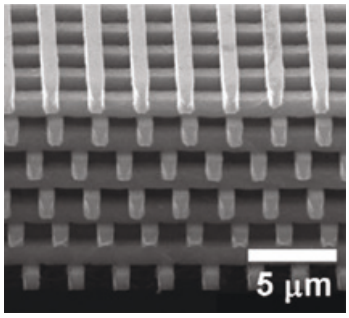 11 layer nickel woodpile MPC structure.	1) A low-cost and large scale fabrication method with sufficient layers in the woodpile MPC structure. A nickel backplane provided durability of MPC the structure. 2) Template fabrication method is time consuming. 3) It is unclear whether the template fabrication method would support fabricating MPCs operating in the NIR to visible region.

Metallodielectric PCs Silicon processed 3D microstructure was used as template. Less than 10 nm thick cobalt was deposited by CVD method as seed layer and then 70 nm of copper was deposited on cobalt layer by electroless deposition [78].	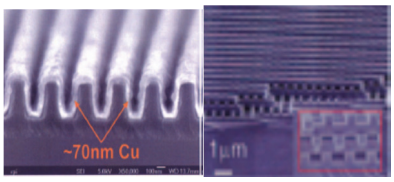 (a) 70 nm copper coating on the template sample grating (b) the metallodielectric PC structure	1) Structure is very small feature sized and contains complete PBG in the NIR region. 2) First band edge position is close to the visible region (around at 750 nm). 3) High fabrication cost. 4) Imperfections occur in the PC structure.
Metallodielectric PC Thin copper layer was deposited by electroless deposition on 3D polymer PC templates fabricated by direct laser writing (DLW) within SU-8 photosensitive resin [79].	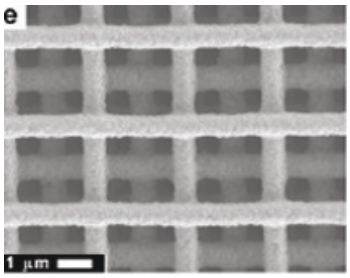 3D PC with copper coating	1) Controlled and homogeneous metal coating can be achieved. 2) The metal surface produces rough surfaces due to finite sized metallic nanoparticles.
3D metallodielectric metamaterials structures 3D microstructure template was fabricated by DLW within SU-8 resin and coated by thin layer of SiO_2 for mechanical stability. Silver was coated by CVD method [80]	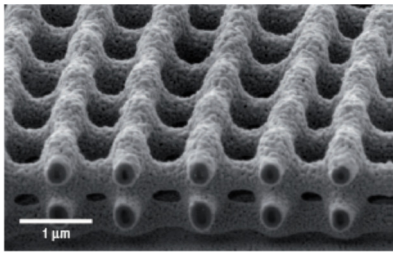 3D metamaterials structure	1) Homogeneous, thin and smooth metal coating can be achieved on the dielectric PC templates. 2) Expensive metal film deposition method. 3) The ability for complete metal infiltration within a multilayer 3D dielectric structure is uncertain.

3D periodic plasmonic microstructures Self-assembled polystyrene latex spheres were synthesised on gold coated surface. Gold film was deposited into the latex spheres by electrodeposition. Finally the latex sphere templates were removed by chemical method [41]	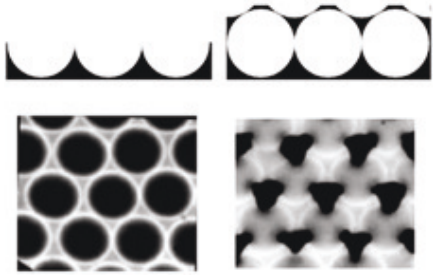 Plasmonic microstructure	1) A low cost fabrication method. 2) Self-assembly method for the dielectric template fabrication ensures high quality metallic microstructure; however, limits the realisation of arbitrary geometries.
3D metallic metamaterials structures DLW was performed within a positive-tone photoresist. After the development, an array of air helices in a block of polymer formed. Electrodeposition method was used to deposit gold into the air helices. The polymer block was removed by plasma etching which led to a square array of 3D gold helices [81].	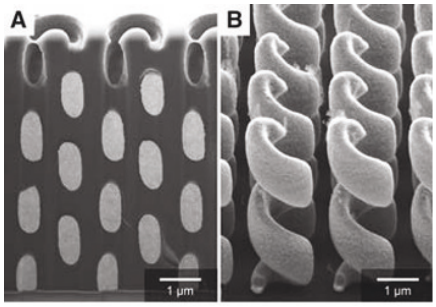	1) A low cost and effective fabrication method. 2) Electrodeposition enables to realise high quality 3D metallic microstructures. 3) Incorporation of a negative photoresist instead of the positive photoresist with the combination of electrodeposition has the potential to realise 3D inversed microstructures.

2.5 Plasmonic waveguides with subwavelength confinement

For the realisation of the truly integrated nanophotonics, manipulation and guiding light in subwavelength scale with complete energy confinement and high optical nonlinearity is a very significant issue. Optical fibres, in some ways, can manipulate light by their excellent waveguiding properties. However, they are totally unfit to be incorporated in miniaturised photonic chips.

PCs offer partial solutions to address this issue by their excellent ability of moulding the flow of light; however, they are also constrained to the diffraction limited guiding properties. In fact, to be able to show the periodicity induced band gap properties the PC structure itself has to be several wavelengths large [4]. Such limitations appear to be making PCs not very promising candidates for manipulating light on the nanoscale.

On the other hand, plasmonics is the most promising approach to offer the unique feature of subwavelength manipulation of EM radiation. Plasmonic waveguides provide the ability to confine modes beyond the diffraction limits. There are several theoretical and experimental demonstrations which were able to realise highly confined and long propagation length plasmonic waveguides. Most of them are surface plasmons (SPs) based planar plasmonic waveguides which localises the surface mode within a flat metal-dielectric interface with a very small cross-section. Other examples are based on hybridisation of SP modes and dielectric modes and thus forming a hybrid plasmon mode.

Among the most promising SPP based subwavelength plasmonic waveguides within the last few decades channel plasmon polariton (CPP) waveguides have emerged as efficient plasmonic waveguides with their strict mode confinement properties. CPPs for EM radiation guiding were first theoretically investigated in

the electrostatic regime by J. Q. Lu *et.al.* [82]. Later on, the retardation effects within the CPP modes were considered by I. V. Novikov *et al*. [83].

The propagation characteristics of the CPP modes within finite and infinite triangular metallic grooves were also discussed by D. K. Gramotnev *et al.* [84, 85]. The first realisation of the CPP modes in subwavelength metal grooves and characterisation of their modal properties such as the mode confinement and propagation distances with metal groove depth and groove angles were demonstrated. A high propagation length (~100μm) with tight mode confinement was demonstrated at the telecommunications wavelength regime.

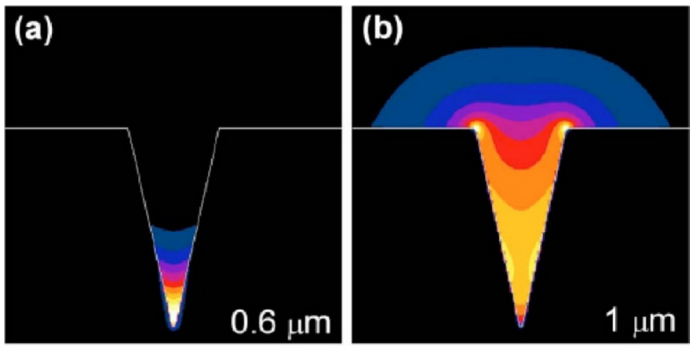

Fig. 2.3 Mode profiles of the CPP waveguide within a truncated metallic (Gold) groove. The semiangle within the groove is 12.5^{o} and the height of the groove is 1.2 μm. (a) The mode profile of the fundamental CPP mode at 0.6 μm (b) The mode profile of the fundamental CPP mode at 1.0 μm [86].

The modal shapes and dispersive properties of the CPPs modes within the finite and infinite metallic grooves and the corresponding propagation losses were discussed thoroughly via detailed numerical simulations by E. Moreno *et al.* [86] The existence of the cut-off wavelength within the metal groove for the fundamental and higher order CPP modes were also investigated. The hybridisation of the CPP modes with the wedge plasmon modes was studied. It was demonstrated that for relatively shallow metallic grooves the CPP mode is guided at the groove opening and is hybridised with the plasmon modes at the groove edges [86].

The wedge plasmon polaritons (WPP) waveguides were found to possess even more distinctive features than the CPP waveguides. WPP and CPP waveguide geometries are exactly identical with the exchange of the metallic and vacuum regions between each other.

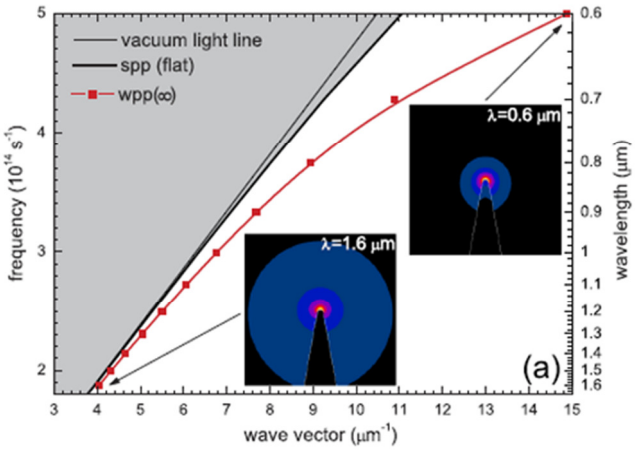

Fig. 2.4 Dispersion relation of the WPP mode supported by a nontruncated wedge with a wedge angle of 20°. Inset: time averaged electric fields of the WPP mode at wavelengths λ =0.6 μm and λ=1.6 μm. The lateral size of the inset plots is 0.5 μm showing its ability of high mode confinement [50].

While possessing the similar propagation loss as the CPP waveguides, WPP waveguides show higher mode confinement [50]. Fig. 2.4 shows the mode characteristics of the WPP modes in metallic wedges with infinitely long edges and surrounded by vacuum. It was shown that focusing of the WPP mode is also possible by decreasing the metallic wedge angle.

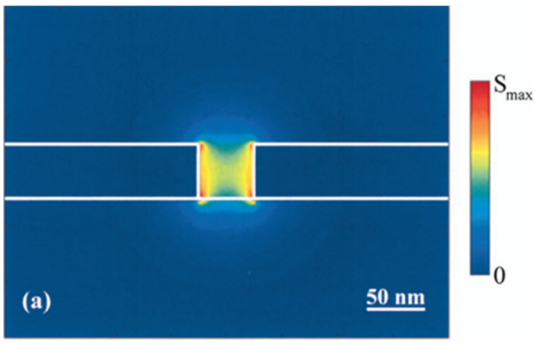

Fig. 2.5 Power density profile of the slot waveguide at λ=1.55 µm which shows that the mode is highly confined within the dielectric slot. The slot material was considered as silica (refractive index = 1.44) and the metal was considered as silver. The slot width and metal film thickness was set to 50 nm [87].

Another type of promising plasmonic waveguide geometry with high mode confinement is the dielectric slot within thin metallic film geometry [87]. The slot within the thin metallic film can be much smaller than the operating wavelength. The mode size is mainly dominated by the near field of the dielectric slot and it was found to be very small compared to the wavelength. The group velocity of the mode was calculated to be close to the speed of light in the substrate. Fig. 2.5 depicts the mode confinement of the slot waveguide. The waveguide possesses a propagation length of ~ 20 µm at the telecommunication wavelength of 1.55 µm [87].

Hybrid plasmonic waveguides can also be very interesting for nanophotonic applications. A hybrid geometry was proposed by R. F. Oulton *et al.* [88] where a high refractive index semiconductor nanowire is surrounded by a low refractive index dielectric medium and placed near a metal surface. The hybridisation of the cylinder mode within the semiconductor nanowire and the SPP mode of the metal surface results in a hybrid mode which stores the EM energy within the low refractive index dielectric spacer between the cylinder and the metal surface. Tuning the semiconductor nanowire diameter d and the low refractive index dielectric gap thickness h very high mode confinement with propagation length

longer than the SPP propagation length at flat metal surfaces was theoretically demonstrated [88].

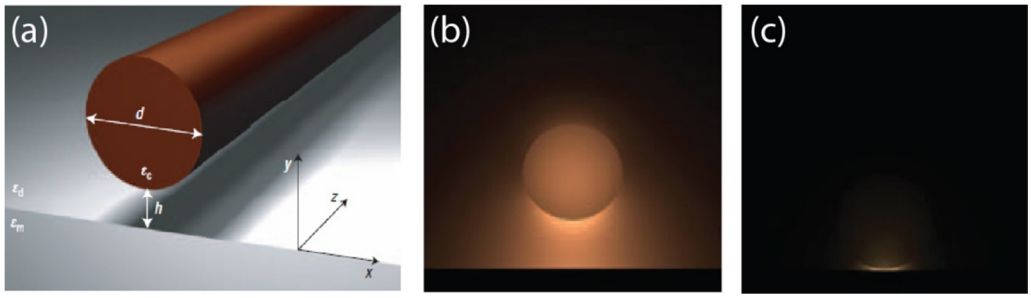

Fig. 2.6 (a) Schematic of the hybrid plasmonic waveguide. The dielectric cylinder nanowire and the low index dielectric gap have permittivity of 12.25 (GaAs) and 2.25 (SiO_2) respectively. (b, c) Mode energy distributions for [d, h] = [200, 100] nm and [d, h] = [200, 2] nm respectively [88].

Although there are several examples of plasmonic waveguides with subwavelength mode confinement, clearly, almost all of the plasmonic waveguides lack the essential feature of total energy confinement i.e. they possess spatial leakage of mode energy. Total energy confinement is a crucial issue for the realisation of integrated photonic devices with zero-crosstalk nanophotonic elements.

Nonlinearity in optical waveguides is also another important feature for the future all-optical communications technology. Highly nonlinear photonic components are very promising for all-optical high speed signal processing. However, dielectric waveguides are unable to provide enhanced nonlinearity due to their inability of mode confinement beyond the diffraction limit. Plasmonic waveguides are thus can be very attractive for realising high optical nonlinearity for their ability of subwavelength mode confinement; however, they are rarely explored in this field.

2.6 Chapter conclusions

MPCs offer intriguing applications in tailored thermal radiation. A number of theoretical studies have been performed on the optical properties of 3D MPCs. The origin of the enhanced absorption within MPCs has been discussed and some effects of the structural parameters and the bulk material properties were analysed. However, the ability of a certain structural design of MPCs for modifying thermal radiation in a desired manner explicitly depends on the optimisation of the resonant absorption within the MPCs maintaining the unique PBG features. For the optimisation of the enhanced absorption within MPCs comprehensive theoretical investigations on the dispersion with structural alterations and the induced effects of the reduced group velocities play a crucial role. Along with these, the effects of the intrinsic dispersive properties of different bulk metals on the MPC resonant absorptions are also vital. Although some theoretical studies were done discussing the optical properties of MPCs, less attention was paid for the optimisation procedures of enhanced absorptions within MPCs. In addition, 3D MPCs are still challenging to be realised for the successful application in the field of modified thermal radiations. Although several researches have demonstrated the fabrication of high quality MPCs with state-of-the-art lithographic technologies, expensive and intricate procedures, limitation of fabricating only certain geometries and inflexibility for tuning the structure in the optical wavelengths region are the major drawbacks. In this thesis, we have presented a detailed theoretical analysis for the optimisation of enhanced absorption in 3D woodpile MPCs in Chapter 3 and demonstrated a novel, low cost fabrication method of realising high quality 3D MPCs operating in the optical wavelengths in Chapter 4.

Plasmonic waveguides have been extensively investigated within the last few decades. Promising plasmonic waveguides with subwavelength confinement and long propagation lengths have been demonstrated. However, complete energy

confinement within subwavelength waveguides is important for realising zero cross-talk nanophotonic elements which is not addressed yet in the currently available plasmonic waveguide geometries. Moreover, optical nonlinearity in plasmonic waveguides is also very important for the optical signal processing. Optical waveguides with high mode confinement produce high Kerr nonlinearity. Highly nonlinear plasmonic waveguides can act as the key elements for the realisation of plasmonic switches, modulators etc. However, plasmonic waveguides are rarely investigated for optical nonlinearity although they contain the unique property of subwavelength mode confinement. We address these issues in a novel class of nonlinear nanoshell plasmonic waveguide which are discussed in Chapter 5 and we have also provided some experimental demonstrations in Chapter 6.

Chapter 3

Optimisation of enhanced absorption in three-dimensional woodpile metallic photonic crystals

3.1 Introduction

Three-dimensional (3D) metallic photonic crystals (MPCs) are of increasing interest due to their unique electromagnetic (EM) features such as a complete and large photonic band gap (PBG) and enhanced optical absorptions [25, 30, 77, 89-93]. In this work, we seek to investigate the alterations of the physical properties that induces for structural modifications of the woodpile MPCs by means of band structure calculations with the use of the finite-difference-time-domain (FDTD) method [94, 95] and demonstrate a detailed picture of the modifications of the enhanced absorption through numerical calculations. We choose the woodpile MPCs for our theoretical study as these MPC geometries have been demonstrated to be very promising over other MPC geometries for their resonant absorption peaks with wide PBGs [25-27]. We also consider the MPC structures are made of

silver and gold as these noble metals have the most promising optical properties (minimal loss in the optical wavelengths) and this also allows to investigate the effects of intrinsic dispersive properties of different bulk metals of the MPCs. We present a detailed theoretical analysis which reveals a useful insight to understand the resonant dissipative behaviour of 3D woodpile MPCs in the spectral response. We show that the magnitude and band width of the absorption resonance in woodpile MPCs can simply be optimised and that the spectral position can widely be tuned by performing small structural modifications. We observe that a small amount of structural parameter modifications can induce great flexibility to alter the properties of the absorption resonance with even an extremely narrow band width of ~13 nm. Analysing the dispersive properties of the 3D woodpile metallic photonic crystals and performing thorough numerical simulations for the finite number of layers we found that the magnitude, band width, and tunability of enhanced absorption can be easily optimised, which can be of significance to design an efficient photonic crystal thermal emitter [96].

This chapter is divided into six sections. Section 3.2 introduces the band gap structures of the MPCs considered in this chapter and demonstrates their basic optical properties i.e. the wide PBG and enhanced absorption at the band edge for finite number of layers via numerical simulations. Section 3.3 analyses the dispersive properties of the woodpile MPC structures with extensive band structure calculations for geometrical alterations. The effect of the flat dispersion bands on group velocities of the propagating modes inside the MPCs has been discussed.

Section 3.4 presents the optimisation of the enhanced absorption within the 3D woodpile MPCs. The dispersive properties of the MPCs analysed with the band structures in Section 3.3 are compared to the spectral properties of the MPCs of finite number of layers calculated with detailed numerical simulations. The optimisation of the magnitude, band width and spectral position of the resonant absorption for different structural and material conditions has been demonstrated.

Section 3.5 introduces a new class of inversed woodpile MPCs with novel optical properties. The enhanced absorption features of the inversed woodpile MPCs are analysed in terms of localised plasmon resonances and also periodicity induced enhanced light-matter interactions. This is followed by the chapter conclusion in Section 3.6.

3.2 Band gap structures of a silver metallic photonic crystal

The basic formation of the MPC structure discussed here is presented in Fig. 3.1(a). We consider a four layer MPC consisting of rectangular metallic rods where the adjacent metallic layers are touching with one another [25]. The background of the metallic components is air. The formation of the structure is a face centred tetragonal (FCT) lattice and the stacking direction (001) is set to be the propagation direction of the incident wave. The metallic part in this MPC is considered as silver. Silver is highly reflective in the optical wavelengths regime form near infrared (NIR) to visible wavelengths with minimal intrinsic optical absorption. Hence, we consider silver an ideal metal for the theoretical investigations of periodicity induced resonant absorption. The corresponding optical properties are defined with the classical Drude model taking the plasma frequency as $\omega_p=1.37\times10^{16}s^{-1}$ and the collision rate $\omega_c=8.5\times10^{13}s^{-1}$ [80]. The width and height of the rectangular rods are defined as *w* and *h*, respectively, and the in-layer rod spacing is *d*. MPCs produce a broad band gap beyond a cut-off wavelength where the transmission resonance occurs along the stacking direction, which is strongly dependent on the overall structural geometry formed by the metallic parts [72, 92]. There also exists a resonant enhanced absorption peak at the photonic band edge due to the dispersive properties of the MPCs. The alteration of the metallic portion of the MPCs can greatly influence the propagation and interaction of the incident wave within the MPC environment and

thus can play an effective role to properly control the anomalous enhanced absorption.

We start with numerical calculations for a silver woodpile MPC of only four layers (one unit cell) with $w=h=300$ nm and in-layer lattice constant $a=d+w=1$ µm. The finite integration technique (FIT) in frequency domain with tetrahedral mesh elements (CST MWS) is used for the calculations. The incident wave is a TE polarised (here, E parallel to the top metallic layer i.e. parallel to y axis) plane wave through the stacking direction (001). Fig. 3.1(b) shows the MPC possesses a wide band gap starting from wavelength 1.5 µm and the first transmission resonance arises at wavelength 1.3 µm. We observe the noticeable enhanced absorption at the band edge near the 1st transmission peak. Almost the same result is obtained for TM polarisation. These calculations are analogous to previous results reported by other studies [25, 72] for a similar kind of the structural geometry, which validate our calculated results.

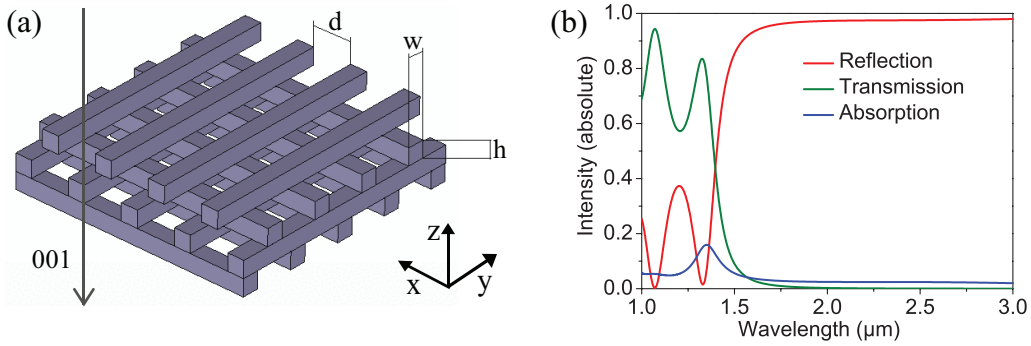

Fig 3.1 (a) A schematic diagram of the silver woodpile MPC. (b) Calculated reflection, transmission and absorption spectra for a silver woodpile MPC with $w=h=300$ nm, and $a=1$ µm. The peak absorption of the MPC occurs at wavelength 1.36 µm where a high pass band exists.

This enhanced absorption is attributed to longer EM wave-matter interaction at the band edge where the EM mode is allowed but propagates with a reduced group velocity [72]. In other words these effects make the spatial decay length of the EM wave short within the MPC structure [97, 98] and thus cause resonant damping (proportional to $1/V_g$) of the propagating modes. To gain the physical

insight of the resonant interaction of the EM wave inside the MPC we simulate the field distribution throughout the structure.

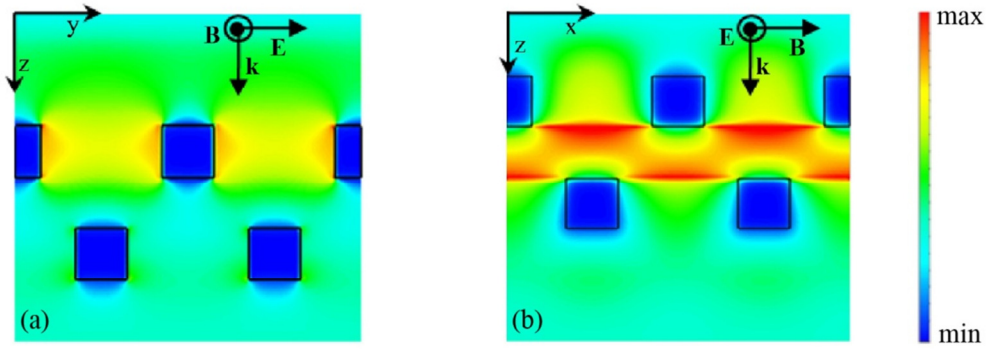

Fig. 3.2 (a) Calculated amplitude plot of the electric field inside the MPC at the band edge of wavelength 1.36 µm in the y-z plane across the 2nd and 4th layers. The strong field enhancement is observed in the 2nd layer near the metallic rod surfaces. (b) Calculated amplitude plot at the band edge across the 1st and 3rd layers in the x-z plane near the metallic rod edges of the 2nd layer. Field plots are on the same scale.

Fig. 3.2(a) shows the amplitude plot of the electric field within the MPC in the y-z plane across the 2nd and 4th layers for the TE polarised plane waves at the band edge of wavelength 1.36 µm which shows strongly enhanced field in the 2nd layer. We then take the snapshot for the TE polarised wave at the x-z plane across the 1st and 3rd layers and near the metallic surface of the 2nd layer and Fig. 3.2(b) clearly shows the multiple orders of the field enhanced near the edges of the metallic rods. This clearly indicates the enhanced light-matter interactions for periodicity induced slowly propagating modes near the band edge. E field enhancement was also demonstrated in two layers of periodic rectangular metallic gratings [99]. However, it should be noted that to experience a periodicity induced photonic crystal dispersive properties at the photonic band gap edge along the propagation direction at least a single unit cell (for FCT woodpile MPC four layers construct a single unit cell as shown in Fig. 3.1(a)) of the MPC is necessary. We also notice the field enhancement occurs at the surfaces of metallic rods which are only perpendicular to the incident electric field direction. For this kind of the field

distribution it was also suggested that the surface plasmon polariton propagation is not supported in such complex metallic networks. Instead the enhanced interaction of propagating light is a result of the photonic band gap effect formed by the waveguide cutoff and the coupling of the inter-layer waveguide modes [92].

3.3 Dispersive properties of three-dimensional woodpile metallic photonic crystals

To investigate the modifications of dispersive properties for different structural parameters we calculate the band diagrams of 3D silver woodpile MPCs by using finite-difference time-domain (FDTD) method on the unit cell of woodpile structures with Bloch boundary condition [94, 95]. The calculation is performed along the Γ- X (001) direction taking the h=0.6 μm, the in-layer lattice constant a=1 μm and varying the w from 0.1 to 0.48 μm. To calculate the eigenfrequencies of each wavevector (**k**) point in the band structure, the Bloch boundary conditions were applied to each **k** point. A dipole moment of a form of Gaussian pulse is placed in an appropriate position in the unit cell to excite all the eigenmodes. A monitor point within the unit cell is selected to record the time evolution of electric field E(t) and the frequency spectrum of electric field E(ω) is obtained by performing discrete Fourier transform. The peaks in the frequency response E(ω) correspond to the eigenfrequencies. To avoid missing some eigenfrequencies whose eigenmodes accidentally have a node at or near the monitor point, we appropriately select several monitor points instead of just one monitor point, and then combine all the frequency spectrums afterwards [95]. We notice that the band structures can be divided into two kinds of band groups, the one with strong electric field amplitude E(ω) while the other with a much weaker field amplitude. The weak bands are ignored and their contribution will be discussed elsewhere. The calculated band structures are shown in Figs. 3.3(a)-3.3(d). We notice from

Fig. 3.3(a) that for *w*=180 nm the lowest energy band ends (band edge) at 136.11 THz. No allowed bands exist below that range. As the rod width *w* increases the band edge of the lowest band shifts to higher frequency. Also, the width of the first allowed band becomes narrower making the band flatten out which indicates the rapid change of the group velocities of the eigenmodes inside the structure. The second band gap between the 1st and 2nd allowed bands becomes wider for increasing *w*.

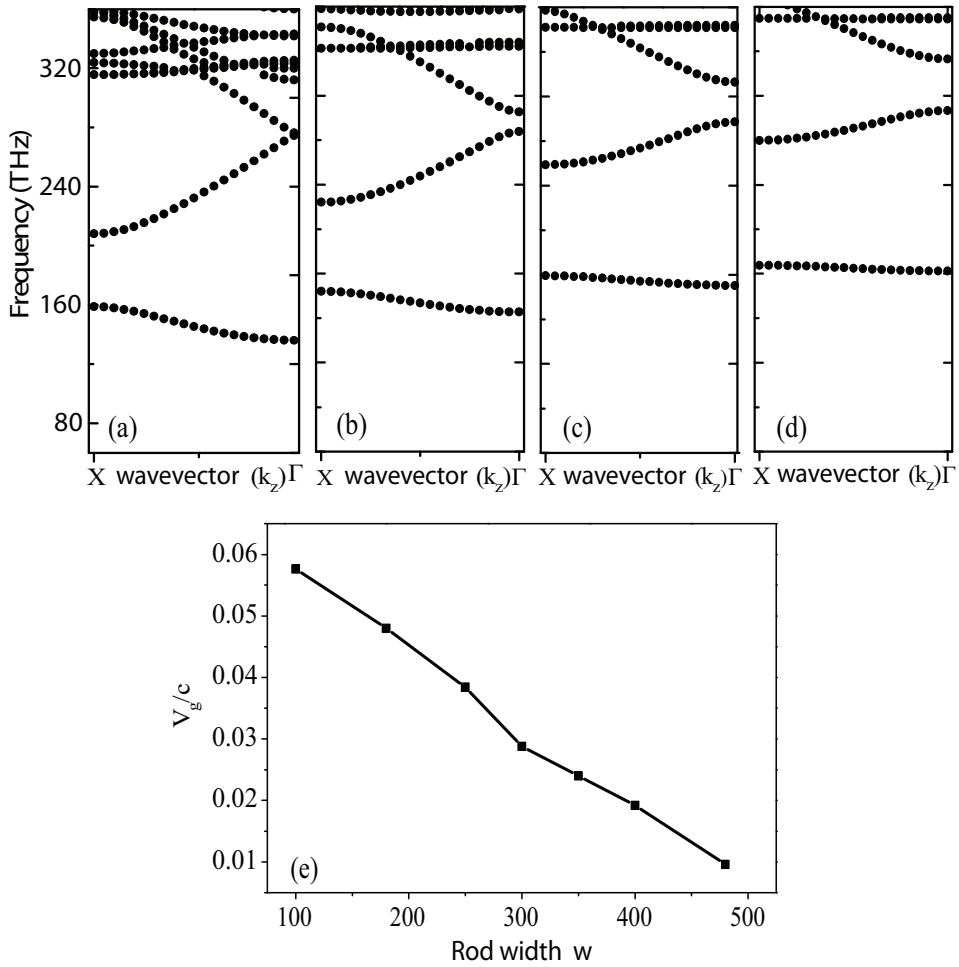

Fig. 3.3 (a-d) Calculated band diagrams of silver woodpile MPCs in the 001 (X-Γ) direction for *w*=0.18, 0.30, 0.42 and 0.48 µm, respectively, with a fixed rod height *h*=0.6 µm. The lowest energy pass band continuously shifts to higher frequency and the band width decreases gradually for increasing *w*. (e) Extracted group velocity profile from the band diagrams.

To understand the physical process of the wave propagation through the MPC we extract the group velocities at the photonic band edges of the lowest energy bands for the different values of *w*. Fig. 3.3(e) shows the variation of the group velocity (V_g) profile of the MPC for increasing *w*. V_g decreases gradually for increasing rod width. It is known that the enhanced absorption at the band edge is inversely proportional to the V_g of the EM radiation [72, 97]. This suggests that in this case the absorption should increase for large *w*. This feature indicates that the enhanced absorption can be optimised through the alteration of the structural parameters.

3.4 Optimisation of the enhanced absorption

For a direct comparison of the results obtained and to investigate the dependence of the resonant absorption with the group velocities we calculate the optical spectra for varying structural parameters of MPCs. Numerical calculations are performed along the 001 direction for four layers of the silver woodpile MPCs keeping the *h* fixed at 0.6 µm. Fig. 3.4(a) shows as we increase the filling ratio by increasing *w* from 0.12 to 0.30 µm, the absorption spectra are found to be blue-shifted and the absorption magnitudes become strong gradually. The absorption reaches its maximum at *w*=0.3 µm but then starts to decrease for the further increase of *w*. However, the group velocity profile depicted in Fig. 3.3(e) suggests that the absorption should gradually increase for greater *w* as the absorption is proportional to $1/V_g$. To understand the possible physical reason underlining this phenomenon, we look at the transmission properties of the MPCs as the absorption is nothing but the damping of the resonant eigenmodes of the pass band near the band edge.

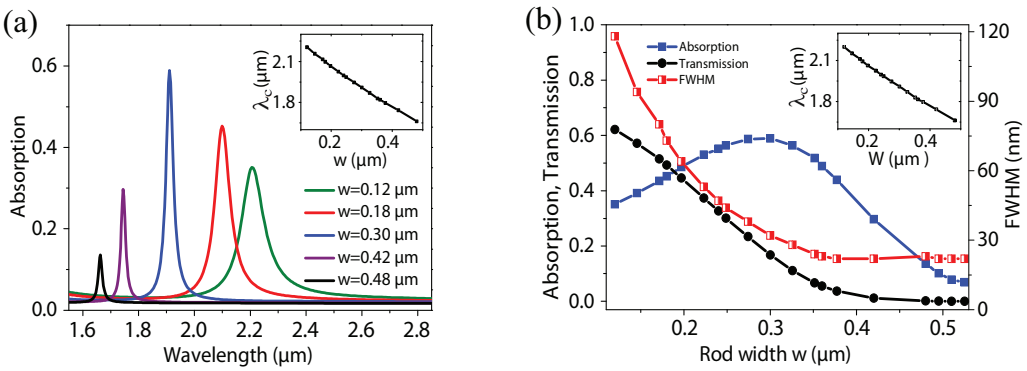

Fig. 3.4 (a) Calculated absolute absorption spectra for different values of *w* of the metallic rods in MPCs with the given value of *a*=1 μm. Inset: The linear relation of the peak absorption wavelength and *w*. (b) Calculated absorption peaks, transmission peaks and the FWHM of the absorption as a function of *w*. Inset: The linear relation of the transmission peak position and *w*.

Fig. 3.4(b) shows that the transmission peaks shift continuously to short wavelengths and their positions agree well with the pass bands predicted by the band diagrams depicted in Figs. 3.3(a)-3.3(d), confirming the validity of both calculations. It should be noted that the inset of Fig. 3.4(b) resembles the inset of Fig. 3.4(a) as the resonant absorption appears at the vicinity of the transmission peak. For increasing w the absorption peak completely overlaps the transmission peak position. The magnitude of the transmission falls off for increasing the filling ratios. From the band diagrams we can clearly see the widths of the lowest energy pass bands decreases for increasing *w* which resembles the transmissions peaks predicted by the numerical calculations. This suggests that for large values of *w*, the narrow air openings between the metallic gratings make the incident radiation difficult to penetrate and results in smaller transmission [100]. Fig. 3.4(b) indeed shows that for increasing *w* the corresponding pass bands blue-shifts and their finite transmission decreases rapidly in magnitude. Thus for larger *w* only a small portion of the incident field can propagate with the periodicity induced extremely reduced group velocity and results in weaker absorption. It can also be noticed from Fig. 3.4(b) that the band widths of the absorption decrease exponentially for increasing the filling ratios, which result from the narrowing of the pass bands. Fig. 3.4(b) shows that the full width at half maximum (FWHM) of

the absorption peak for w=0.42 µm is 23 nm, which is more than five times smaller than the FWHM of 118 nm for w=0.12 µm while the peak absorptions for both do not differ too much. This feature suggests that the absorption peak position can be tuned over a broad wavelength range with a desired FWHM. As can be found in Fig. 3.4(b), the absorption is the maximum (59%) at wavelength 1.91 µm for w=0.3 µm while the FWHM is remarkably narrow (only 32 nm).

We further investigate the magnitude, and position of the absorption spectra of MPCs with respect to the height of the metallic rods for the same values of a as that used in the previous case. We increase the height of the metallic rods gradually for a broad range from h=0.3 µm to 0.9 µm with taking w=0.3 µm in our simulations for TE waves. It can be seen from Fig. 3.5(a) that the absorption peaks shift to longer wavelengths for increasing h and this can be attributed to the red shift of the corresponding pass band due to the increase of the lattice constant in the propagation direction [72, 92].

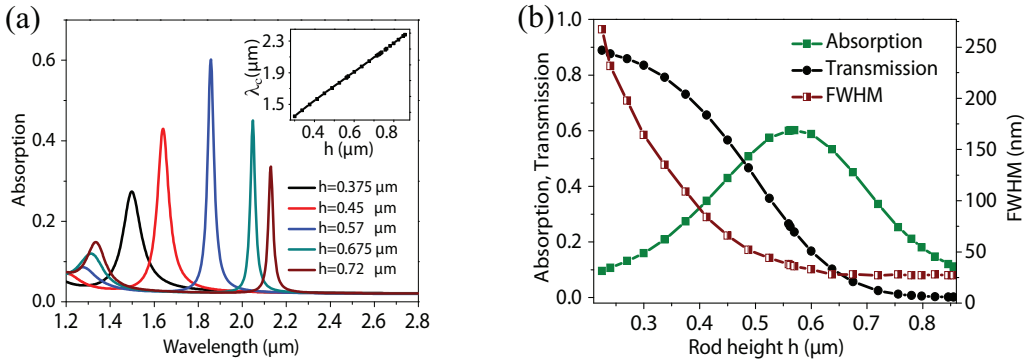

Fig. 3.5 (a) Calculated absorption and transmission spectra as a function of h. Inset: The linear relationship of the peak absorption wavelength and the rod thickness h. The curve follows the opposite trend to that of figure 3.4a. (b) Calculated absorption, transmission and the FWHM of the absorption as a function of h.

The magnitude of the absorption peak increases for large h as predicted before [72]. However, for further increase of h the absorption peak reaches its maximum (~ 60%) at around h =0.57 µm and then surprisingly falls in magnitude keeping the red-shift as can be seen in Fig. 3.5(a). The decreasing value of the

transmission peak for increasing *h* suggests that only a fraction of the incident field can propagate through the structure and results in less absorption for large value of *h*. The peak absorption wavelength follows a linear relation with *h* as can be seen in the inset of Fig. 3.5(a) but shows an opposite trend to that of Fig. 3.4(a) for varying *w*. The detailed spectral behaviour can be seen in Fig. 3.5(b) which depicts that the FWHM of the absorption resonance falls exponentially for increasing *h,* which resembles the case in Fig. 3.4(b) for increasing *w*. The FWHM of the maximum absorption peak at 1.86 μm is only 36 nm. The transmission peak magnitude does not follow the trend of the absorption magnitude rather it gradually decreases for increasing *h*. An interesting feature of the considered MPC is that the transmission has a high peak value for $h<w$ (maximum 88.9 % for h=0.225 μm). This is reasonable, as the propagation length along the 001 direction effectively decreases for the small value of *h*, which yields less damping of the incident radiation. For MPC applications where high transmission is required such structural configuration may be useful. It is remarkable that both *h* and *w* can play a significant role to alter the resonant dissipative behaviour of the woodpile MPCs. For increasing *h*, we also observe that the absorption peak vanishes from a finite value (only the intrinsic absorption of the metal remains) when the 1st order transmission peak completely disappears for h>0.9 μm. The same behaviour was also observed for increasing *w* where the absorption peak disappears for vanishing transmission resonance. These observations clearly support the argument that the enhanced absorption occurs only when there exists a pass band with finite transmission to allow the enhanced EM wave-matter interaction inside the MPC introduced by a smaller group velocity.

As the origin of the absorption resonance depends on the intrinsic absorption defined by the finite value of the imaginary part of the $\varepsilon(\omega)$ [72] it is expected that the resonant spectral properties of woodpile MPCs should vary for different bulk materials. We consider a four layer MPC of gold with bulk parameters defined by the Drude model with plasma frequency $\omega_p = 1.3647\times10^{16}$ /s and collision rate

3.65×10^{13} /s [100]. The collision rate of the bulk gold is quite different from that of silver, which can influence the dispersive properties of the MPCs.

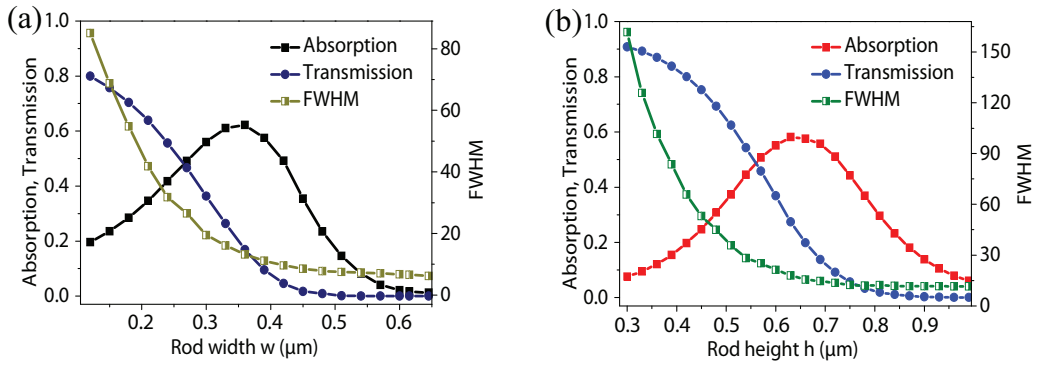

Fig. 3.6 (a) Calculated intensity spectra of a gold woodpile MPC for different values of *w*. (b) Calculated intensity spectra for different values of *h*. Gold MPCs show more distinctive features than silver MPCs.

We calculate the spectral properties of the gold woodpile MPCs for the same structural parameters used in the case of silver MPCs. Figs. 3.6(a) and 3.6(b) show the complete optical properties of the gold MPCs for different values of *w* and *h*. Gold MPCs show even more distinctive features than that of the silver MPCs. Both Figs. 3.6(a) and 3.6(b) show the similar trends of the spectral behaviour to the silver woodpile MPCs but with even narrower band widths. Fig. 3.6(a) shows that for changing *w* the maximum absorption (62.2%) appears for *w*=0.36 μm at wavelength 1.82 μm with a FWHM of only 13.2 nm. This band width is more than two times narrower than the FWHM of the maximum absorption of the silver MPC for varying *w*. Fig. 3.6(b) shows for increasing *h* the maximum absorption (58.2%) for the gold MPC appears for *h*=0.63 μm at wavelength 1.96 μm with a small value of the FWHM of 18 nm. These structural parameters and bulk material dependent resonant spectral behaviours of 3D woodpile MPCs can be very advantageous for enhanced absorption related applications.

3.5 Inversed woodpile metallic photonic crystal as a new structural design.

In the previous sections we have provided the optimisation of enhanced absorption in 3D woodpile MPCs. The enhanced absorption in these MPCs only occurs at the photonic band edge which is solely caused by the enhanced light-matter interaction due to the low group velocity of light. However, incorporation of more absorption peaks into MPCs could be even more useful for applications in tailored thermal radiations. Here, we present a new MPC structure which supports multiple enhanced absorption peaks caused by robust plasmon resonances along with low group velocity interactions at the photonic band edge.

We consider a woodpile dielectric photonic crystal (PC) fabricated by the direct laser writing (DLW) method [101, 102] and assume an infiltration of metal into this dielectric PC by any scientific methods. After the infiltration, we further assume that the dielectric portions are removed and only the metallic portions remained. The metallic skeleton assumes an inversed geometry compared to the original dielectric PC structure geometry. We name it an inversed woodpile MPC structure. The assumed fabrication process scheme is presented in Fig. 3.7.

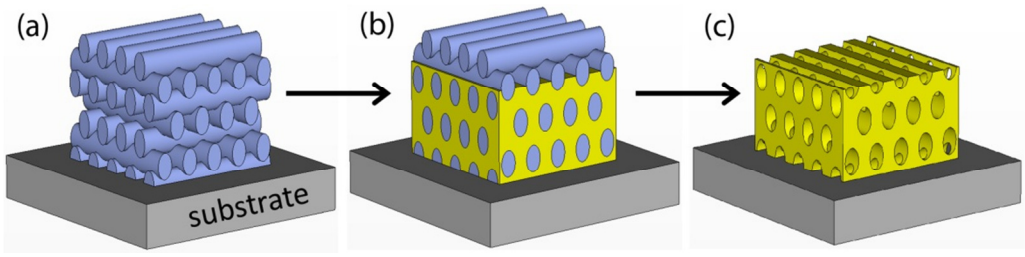

Fig. 3.7 Schematic of the assumed fabrication of an inversed woodpile MPC. (a) Dielectric PC fabricated by DLW fabrication method. (b) Metal deposition into the dielectric PC (c) Removal of the dielectric portion results in inversed woodpile MPC.

We consider that the infiltrated metal into the dielectric PC is gold. We carry out numerical simulations for gold inversed woodpile MPC structure and analyse the optical properties. Fig. 3.7(c) shows the schematic of the gold inversed woodpile MPC assuming the dielectric portions of the PC has been removed. The height of the gold film is considered as 2.8 µm thick which roughly covers four layers and the lattice constant of the air cylinders was set to 1.0 µm. The width of the air cylinders was considered as 580 nm with an aspect ratio of 1.5. Fig. 3.8 shows the calculated reflection, transmission and absorption spectra of the gold inversed MPC for perpendicular incidence of excitation.

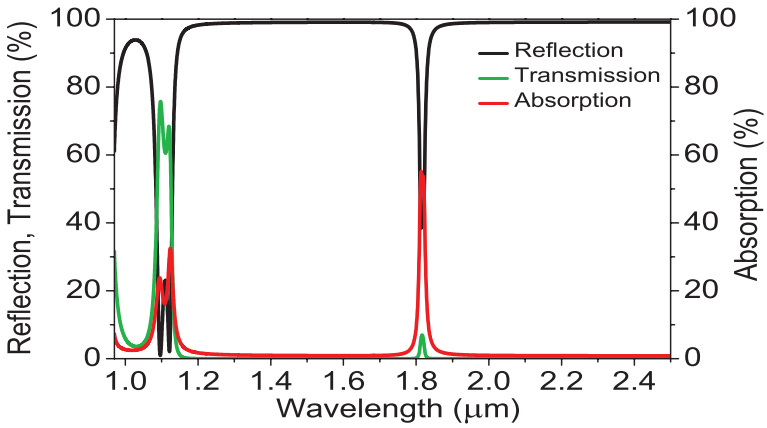

Fig. 3.8 Calculated reflection, transmission and absorption spectra of the inversed woodpile MPC.

The gold inversed woodpile MPC structure exhibits a large PBG starting from ~1.16 µm with doublet transmission peaks (pass bands) near the photonic band edge. The enhanced absorption can also be noticed near the transmission peaks which can be attributed to the damping of the propagating modes at the photonic band edge due to low group velocity. These results are consistent with the characteristics of MPCs (as discussed in previous sections in this chapter). However, a sharp absorption peak with 55% absorption magnitude can also be noticed at ~1.81 µm which is far beyond the photonic band edge. Also, the corresponding transmission peak has very weak magnitude (6%) as opposed to the strong transmission peak near the band edge. For further clarification we took the field plots at these wavelengths of the enhanced absorptions.

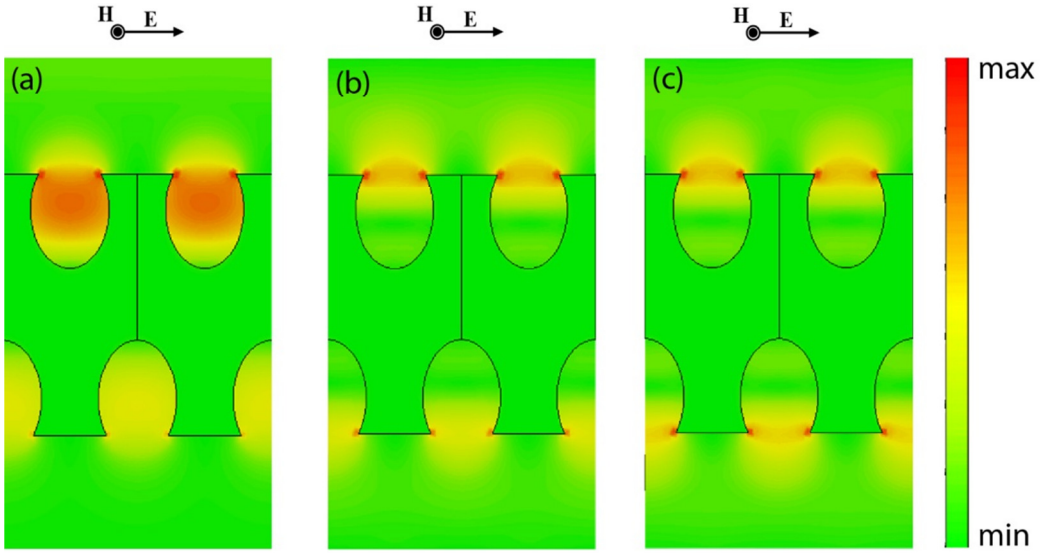

Fig. 3.9 (a) Amplitude plot of the electric field at 1.81 µm corresponding to the sharp resonance (b, c) Amplitude plots of the electric fields at 1.12 µm and 1.10 µm respectively for the doublet absorption peaks near the band edge.

Fig. 3.9(a) depicts the strong localised field enhancements within the air cylinders formed inside the inversed MPC. This field enhancement resembles cavity plasmon resonances with their highly localised nature within the cavity. The cylindrical cavities within the metallic portion of this inversed woodpile MPC assisted to generate these plasmon resonances. Unlike this localised field enhancement at the plasmon resonance, the field enhancements of the absorption peaks near the band edge do not show such strict confinement within the cavity. Indeed, it can be clearly seen from Figs. 3.9(b) and 3.9(c) that the modes at the band edge highly interact with the metallic surface resulting in enhanced absorption and also decouple from the cavities at the bottom layer of the MPC indicating their propagating nature.

These results suggest that inversed woodpile gold MPC structures fabricated by the DLW method in combination with a chemical method have the potential for realising large band gap and multiple enhanced absorption peaks which can be very useful for tailored thermal emission. Also, such novel structures can support localised plasmon resonances with a strong local field enhancement which may

also be attractive for plasmonic solar cells. The reason behind is that for plasmonic solar cells with metallic nanostructures/particles, the strong near field enhancement at the plasmon resonances can induce enhanced light absorption in the solar cells [6, 48, 103, 104]. In Chapter 4, we will present an experimental method to realise the inversed woodpile MPCs.

3.6 Chapter conclusion

We have theoretically investigated the resonant absorption and transmission spectra and demonstrated the inter-relation in detail for different structural conditions for 3D woodpile MPCs. We have shown that properly altering the filling ratio and the metallic rod thickness can lead to flexibly tuneable absorption peak over wide spectral range with desired absorption magnitude and FWHM. We have demonstrated the optimisation of enhanced absorption of silver and gold woodpile MPCs. For silver woodpile MPCs, a maximum absorption of 60% with FWHM of 36 nm was demonstrated while for gold woodpile MPCs at the maximum absorption of 62.2% a very narrow FWHM of 13.2 nm was revealed.

As Kirchhoff's law directly relates thermal emission to absorption, the potential application of MPCs for tailored thermal emission depends on the control of resonant absorption peak along with the band gap. MPCs of finite absorption magnitude with a thin band width can lead to highly efficient recycling of thermal radiation into a selected narrow emission channel.

We have also introduced a new class of inversed woodpile MPCs which show multiple enhanced absorption peaks including localised plasmon resonances. These multiple absorption peaks with their different spectral positions within the PBGs could assist further for tailored thermal radiation in the desired wavelengths. Furthermore, the near field enhancement caused by the robust localised plasmon resonances has potential applications in plasmonic solar cells.

Chapter 4

Realisation of three-dimensional metallic photonic crystals and optical absorption

4.1 Introduction

Realisation of high quality metallic photonic crystals (MPCs) with a spectral tunability and low fabrication cost is still challenging. The aim of this chapter is to experimentally demonstrate the realisation of high quality three-dimensional (3D) MPCs and investigate their enhanced optical absorptions due to the periodicity induced enhanced light-matter interaction at the photonic band edge. Resonant optical absorption can also exist in 3D metallic microstructures due to the localised plasmon resonances with strong field enhancement [41, 42, 105]. However, such optical absorptions with plasmon resonances are rarely explored in experimental studies for 3D MPC structures. In this chapter, we have experimentally demonstrated enhanced optical absorption by the excitation of localised plasmon resonances in 3D inversed woodpile MPCs. We have also demonstrated a novel fabrication method for the experimental realisation of 3D inversed woodpile MPCs operating in the optical wavelengths. This fabrication

method depends on the infiltration of metals into 3D polymer photonic crystal (PC) templates which eventually results in inversed MPCs. We report on the enhanced optical absorption over a wide range of optical frequencies in these novel MPC structures. We support our experimental findings with numerical simulations which confirm the high quality of our 3D inversed woodpile MPCs.

Although there are many fabrication methods to realise MPCs not all of them are efficient for realising high quality and cost-effective 3D MPCs. On the other hand, the functionality of the fabrication method also depends on the ability of realising 3D MPCs with arbitrary geometries, which is also hard to achieve. The fabrication method proposed in this chapter has the potential to realise arbitrary 3D metallic microstructures. Here we demonstrate the realisation of the 3D inversed woodpile MPCs with the unique combination of the state-of-the-art direct laser writing (DLW) fabrication method (for dielectric woodpile PC template fabrication) and the electrodeposition method (for metal deposition into the dielectric PC). We characterise the optical properties of the 3D inversed woodpile MPCs with Fourier transform infrared (FTIR) microscopy techniques and compare the results with numerical simulations.

This chapter is divided into five sections. Following the introduction in section 4.1 we introduce the 3D polymer woodpile PC template fabrication in Section 4.2. The DLW method for microfabrication is discussed in section 4.2.1. The basic set up of our DLW system and the structural geometry of interest with the multiline laser scanning approach for achieving appropriate filling ratio are presented in Sections 4.2.2 and 4.2.3 respectively.

Section 4.3 describes the detailed method for the realisation of the inversed woodpile MPC structures. The treatment of the polymer 3D PC templates with electrolyte solution and infiltration of metal into the template by electrodeposition method with a controlled growth rate of the metal film are discussed. Section 4.4 focuses on the optical characterisation of the 3D inversed woodpile MPCs. The

enhanced optical absorptions are investigated experimentally with FTIR microscopy measurements and the results are compared with numerical simulations. Section 4.5 presents the chapter conclusions.

4.2 Fabrication of three-dimensional woodpile photonic crystal templates by direct laser writing

In this section we provide a brief introduction about the DLW fabrication in photosensitive resins for 3D polymer PC microstructure template fabrication and discuss our basic DLW fabrication set up.

4.2.1 Direct laser writing

To realise our polymer PC microstructure template we employ the two-photon polymerisation (2PP) process which is provided by using a DLW fabrication method. In a 2PP process photosensitive resins undergo phase transition by inducing photopolymerisation upon the exposure of a tightly focussed laser beam. The photosensitive resin is generally a polymer matrix which is composed of a small fraction of an initiator and a maximum portion of a monomer. In such a process simultaneous absorption of two photons into the photoinitiator molecules turn them into free radicals which react with the monomers to form monomer radicals. The active monomer radicals form a cross-linked solid phase of the monomer [106, 107].

To initiate the 2PP process, a tightly focused laser beam with ultrashort laser pulses is used to expose the photosensitive resin. To supply high peak power within the tight focus, femtosecond laser pulses are in generally used for 2PP. Only the exposed portion of the photosensitive resin within the tight focal volume

of the laser beam undergoes the two photon absorption (2PA) process and yields photopolymerisation. 2PA is also fundamentally different from single-photon absorption process in the sense that the strength of the absorption is proportional to the square of the laser light intensity and hence operates in a nonlinear process. On the other hand, the laser irradiation frequency has to be lower than the single photon absorption frequency of the photosensitive resin to guarantee the 2PA as the only contributing process for photopolymerisation [108]. With a computer controlled piezoelectric scanning stage based DLW system the polymerisation process can be precisely controlled to expose the photosensitive resin in full 3D manner. The scanning stage contains extreme precisions in its dynamic range for 3D scanning and in combination with appropriately written computer programs it is possible to perform DLW with desirable lattice sizes and fabrication speed. Because of the different chemical bonding of the exposed and unexposed molecules of the photosensitive resin the unpolymerised portion can be selectively washed away through post chemical process and the remaining part of the sample comes out as a true 3D microstructure.

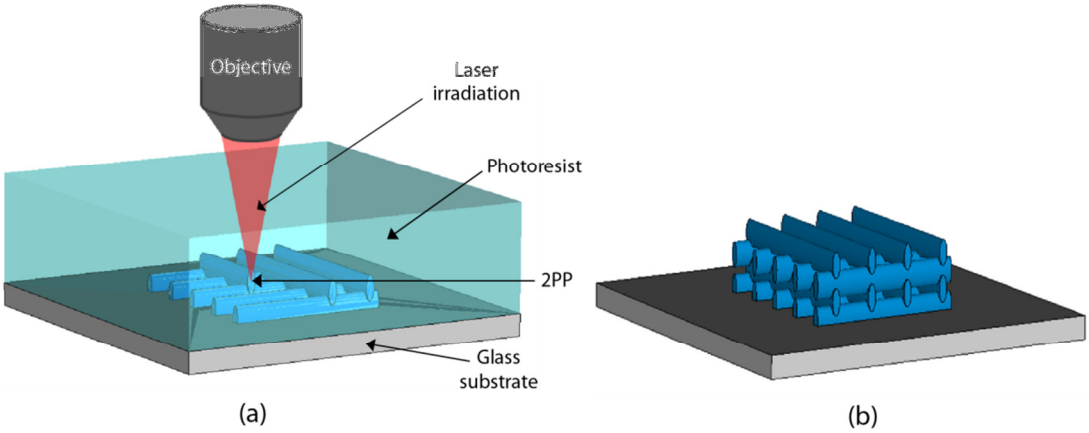

Fig. 4.1 Schematic presentation of the 2PP fabrication process. (a) 2PP is initiated by DLW. (b) Polymer microstructure after the removal of the unexposed portion of the polymer.

DLW is a very efficient, convenient and precise method to realise photonic microstructures with arbitrary geometries and sizes. The DLW fabrication system has been extensively used within the photonics community for micro-fabrication in photosensitive resins [101, 102, 109, 110]. The resolution of the DLW fabrication system depends on the spatial resolution i.e. the numerical aperture (NA) of the objective lens, the associated operating femtosecond laser wavelength and also on the photosensitivity of the resins to laser pulse energy and repetition rate [111]. Besides, the mechanical strength of the fabricated polymeric microstructure depends on the polymer material composition and on the proximity effect of the polymer [112].

4.2.2 Fabrication set up for direct laser writing

The basic fabrication method for 2PP used in this thesis for fabricating polymer microstructure templates is similar to the one used for DLW fabrication of dielectric photonic crystals [101]. In this set up a beam of Ti:Sapphire laser (Mira 900-F, Coherent) operating with a pulse width of ~150 fs, a wavelength of 800 nm and a repetition rate of 76 MHz was used to pump an optical parametric oscillator (OPO). The OPO with output pulses of the 580 nm wavelength is used for 2PP microfabrication.

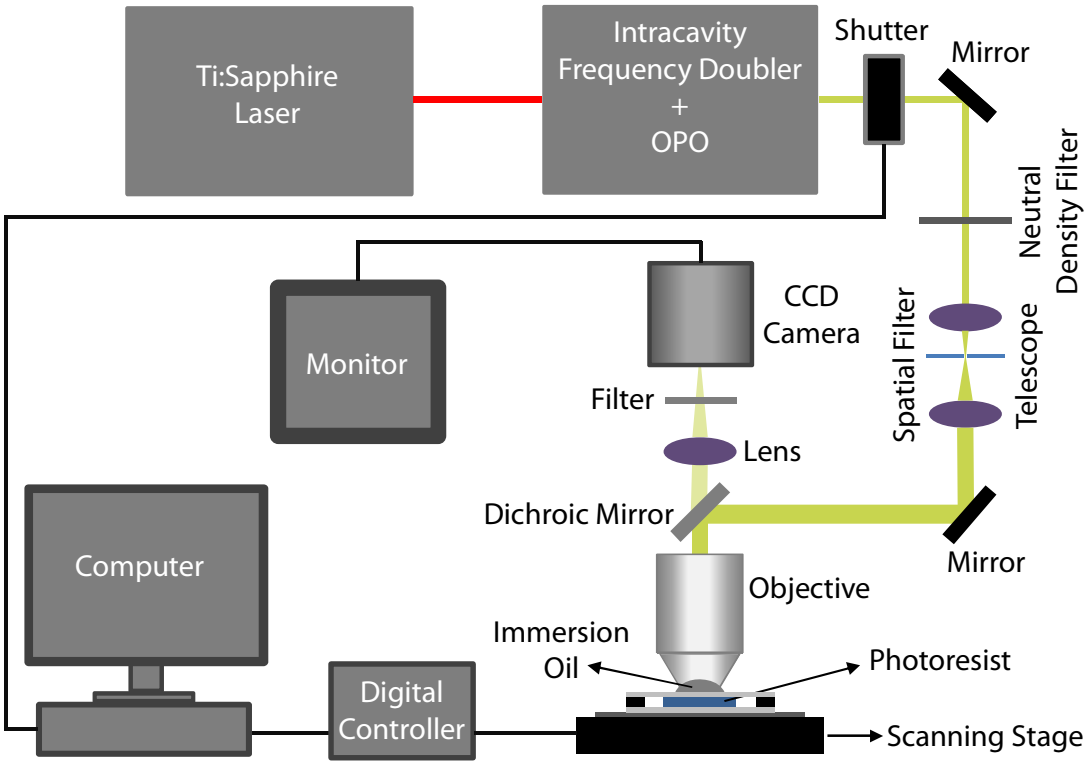

Fig 4.2 Schematic of the DLW set up

The laser power was controlled manually by a neutral density filter. A telescope system in combination with a spatial filter was used for the magnification and collimation of the beam with a uniform illumination. The femtosecond pulses were focused into the liquid photosensitive resin with an oil-immersion high NA objective (Planapo, Olympus, NA=1.4, 100×). The liquid IP-L photoresist (Nanoscribe Gmbh) was sandwiched between two coverslip glass substrates and mounted on a three-axis 200 µm×200 µm×200 µm piezoelectric scanning stage (P562, Physik Instrumente). A mechanical shutter for the laser beam and the scanning stage were synchronised together and were controlled by a computer which is operated with programmed design files for desired microstructures fabrication. The photo-polymerising process in the resin was monitored in real-time with a charge-coupled device (CCD) camera.

4.2.3 Fabrication of woodpile dielectric photonic crystal templates

The DLW fabrication method is extensively and successfully used for the fabrication of microstructures including PCs and metamaterials. The supreme feature of the DLW over other fabrication methods is its ability of fabricating microstructures with arbitrary geometries [80, 101, 102, 109, 110, 113]. Among these, woodpile geometry for PCs was first proposed independently by Ho et al. [114] and Sözüer and Dowling [115] both in 1994 [13]. Later this geometry was employed to realise woodpile PCs operating in the near infrared (NIR) to visible region [101, 102, 116]. Here, we adopted this woodpile geometry as a template for realising MPC microstructures rather than using it for dielectric PC applications.

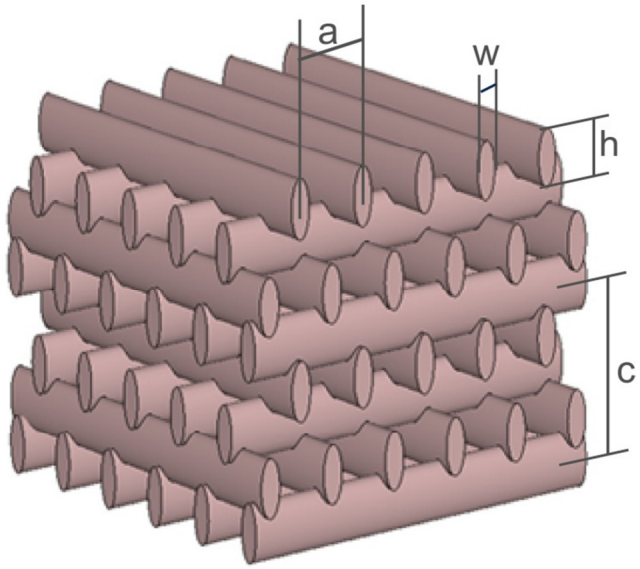

Fig. 4.3 Schematic of a 3D woodpile PC. Each layer in the structure is consisted of solid and parallel dielectric rods with structural parameters: *w*, rod width; *h*, rod height; *a*, in-layer lattice constant; and *c*, height of one unit cell (four times vertical layer spacing).

Fig. 4.3 shows the geometry of the woodpile PC. The structure consists of layers of parallel one-dimensional (1D) rods where within each layer the rods have a periodicity or a lattice constant of *a*. The adjacent layers are rotated by 90^0 and the

second nearest-neighbour layers are shifted by *a*/2 relative to each other. The interlayer spacing is *dz* and four layers construct a unit cell which has a height of *c*. A finite woodpile structure is formed with just repeating the unit cells multiple times as required. The resulting structure possesses a face-centred-tetragonal (FCT) lattice symmetry.

There are a number of photoresists available for realising microstructures with the DLW method and among them SU-8 (MICROCHEM), Ormocer (the Fraunhofer Institute for Silicate research) and IP-L (Nanoscribe Gmbh) are some of the most commonly used and commercially available ones. In this thesis, we have used the commercially available IP-L (fully organic acrylic resin) photoresist. IP-L photoresist has been demonstrated to provide better resolution for polymerised feature sizes with enhanced mechanical stability than other photoresists. IP-L also provides very little proximity effects within the adjacent photo-polymerised elements fabricated by DLW [112].

The IP-L photoresist sandwiched between two coverslips is approximately 50 µm thick. The structures were fabricated from the surface of the bottom glass coverslip. We fabricate structures with both solid supporting frames (frame surrounding the four sides of a single woodpile structure) and without frames to check the shrinkage effects which generally occur during the photopolymerisation and post process. The polymer rods within the woodpile structure were fabricated with a scanning speed of 30 µm/s and the frames were fabricated with a speed of 150 µm/s. The laser power for fabricating rods was varied according to desired size and lattice parameters of the rods and the power for fabrication of frames was kept fixed. After the DLW fabrication the liquid IP-L photoresist with the polymerised microstructure was washed with isopropanol. After 20 minutes of exposure in the isopropanol, only the polymerised portion of the resin remained and the microstructure was achieved. Fig. 4.4 shows the top view images of our fabricated woodpile PC structures (12 layers) by the DLW method in IP-L. It was noticed that even without the frames the PC microstructure possesses high quality

with very insignificant amount of shrinkage whereas significant shrinkage problems were previously reported for microstructures fabricated with liquid photoresist other than IP-L [101, 102].

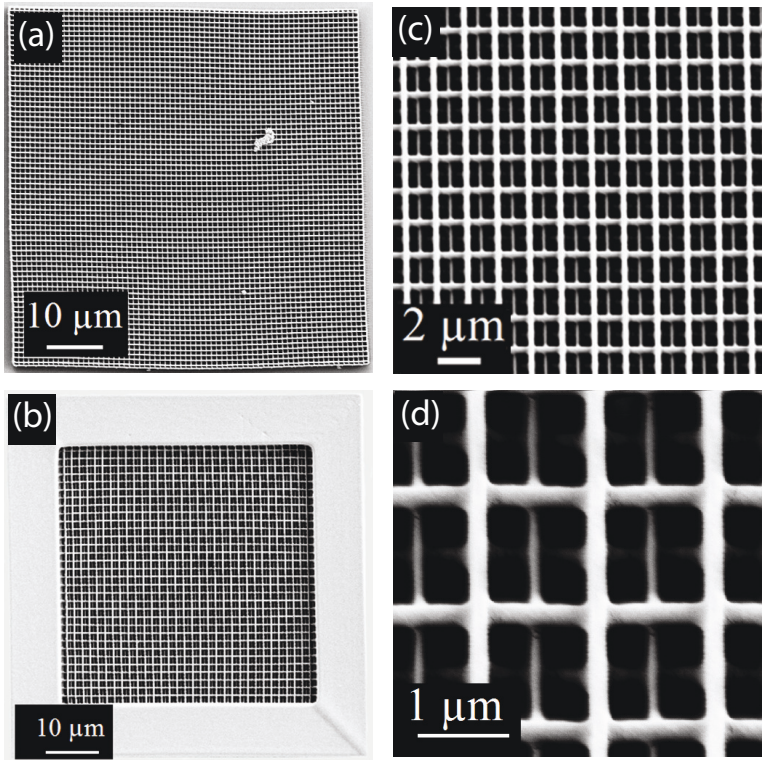

Fig. 4.4 SEM images (Top views) of woodpile PC microstructures fabricated by DLW in IP-L photoresist. (a) A frameless 60×60 µm structure with 1.0 µm in-layer lattice constant. (b) Woodpile structure with 1.5 µm in-layer lattice constant and supported with 10 µm wide frames. (c), (d) Magnified views of the structure shown in (b). The fabricated rods in the bottom layers appear thinner than those of the top layer as the SEM focussed on the top layer provided lower resolution for the bottom layers.

4.2.4 Multiple line fabrication for high filling ratios

To achieve an inversed MPC structure with an appropriate filling ratio of metal the polymer template also needs to possess a right filling ratio for the polymer portion. However, the polymer rods in the fabricated woodpile template are unable to create high filling ratio due to the elongated nature of the rod cross-

section (i.e. the voxel shape). The optical intensity distribution in the focal spot of the high NA objective creates elongated shape in the axial (z) direction (in our case the voxel cross-section has an aspect ratio of ~2.9). Furthermore, the spacing between adjacent in-layer rods needs to be minimised for our operating wavelength of interest (NIR). Increase of laser power can increase the rod width; however, maintains the same aspect ratio i.e. the elongated voxel shape persists. Hence, we need to employ other methods to increase the lateral size of the voxel compared to the axial size. Here, we follow the multiline laser scanning method for the DLW microfabrication [112, 117]. We employ five parallel laser exposures with a lateral displacement of 100 nm to achieve thick polymerised rods with low aspect ratio. In combination with different fabrication power and multiline laser scanning with a fixed displacement a lowest aspect ratio of ~1.24 with a polymerised line width of 700 nm was realised. The in-layer lattice parameter for the polymer PC template was kept as 1.5 µm for a constant interlayer spacing *dz* of 0.6 µm.

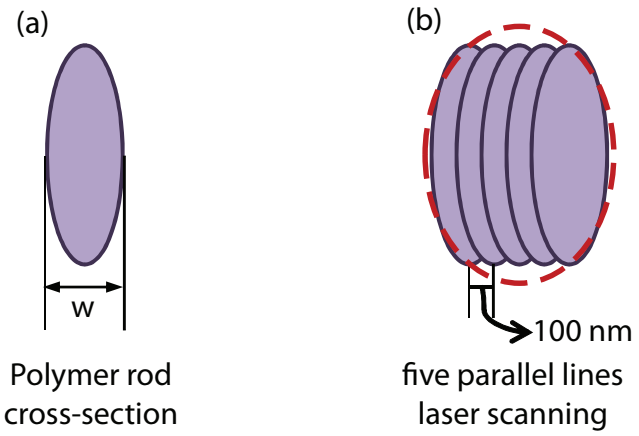

Fig. 4.5 Schematic of fabricating thick and low aspect ratio polymer rods. (a) The rod cross-section with an aspect ratio of 2.9. (b) Multiline laser scanning.

4.3 Metal infiltration into three-dimensional woodpile polymer photonic crystal templates

4.3.1 Electrodeposition

In this section, we discuss the chemical method for infiltrating metal into the polymer template. We employ electrodeposition method which is a well-known branch of electrochemistry and are explained in any standard text book of electrochemistry. In brief, in this process an electrolyte solution (made of any salts of the corresponding metal to be deposited) is exposed to an external electric field to reduce metallic ions. The electrodeposition process can be started with an external direct current (DC) source in conjunction with two electrodes. The metal atoms at the anode plate (generally made of the corresponding metal to be deposited onto the cathode) can oxidise to form cations and these cations can associate with the anions in the electrolyte solution. The cations in the electrolyte solution can reduce at the cathode to deposit neutral atoms and can form a metal layer over the cathode. The process can be continued until a desired thick homogeneous layer over the cathode is formed. Electrodeposition is a very inexpensive method compared to other methods such as the chemical vapour deposition (CVD) and the atomic layer deposition (ALD) for depositing metals into microstructures.

4.3.2 Metal deposition into photonic crystal templates

Electrodeposition has been previously used to deposit metals into the dielectric microstructure templates [77, 118, 119]. Electrodeposition has also been used to infiltrate metal into the woodpile PCs fabricated by soft lithography [26]. However, it should be noticed that the operating wavelength of those fabricated

metallic microstructure lies within 2-10 µm which is longer than the wavelength region we are interested in. Moreover, the reported metallic microstructure does not support any plasmon resonances in which we are also interested in. The combination of our DLW based dielectric PC template fabrication and electrodeposition based metal infiltration method allows us to realise metallic MPCs operating in the NIR region. In addition, our fabrication method has the potential to realise MPCs operating even in the visible region. Fig. 4.6 shows the basics of our experimental procedures to achieve 3D inversed woodpile MPC structures.

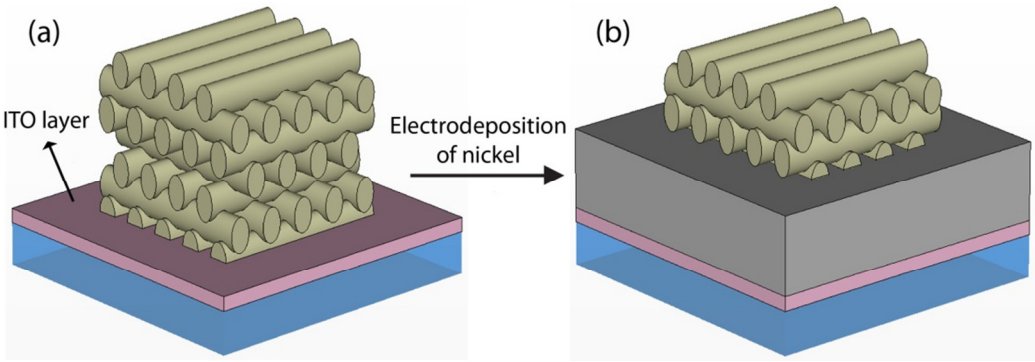

Fig. 4.6 Schematic diagram of the fabrication of inversed woodpile MPCs (a) Woodpile dielectric PC template on the ITO coated cover slip. (b) Metal infiltrated woodpile template.

We fabricate our polymer PC templates on the indium-tin-oxide (ITO) coated glass coverslips (70-100Ω, SPI Supplies). The conductive ITO layer works as cathode during the electrodeposition process. ITO layered glasses are also highly transparent in the optical region. The transparency drops in the longer wavelengths with higher conductivity of the ITO coating. Our ITO coated glass coverslips have high transmission of around 70-80% in the 1.0 µm to 3.5 µm wavelengths region which perfectly fits our experimental requirements. Before the DLW fabrication, the ITO glass coverslips were cleaned with ethanol and then thoroughly rinsed with distilled water. The glass coverslips were then heated to 75^0C into a commercially available water-based detergent (Caswell) for 5 minutes for further cleaning and followed by rinsing with distilled water. After the DLW

fabrication the ITO glass coverslips were again thoroughly rinsed with distilled water.

In our experiment, we choose nickel metal to be electrodeposited into our polymer PC templates. Nickel is highly reflective (weak absorption) in the mid-infrared and fairly reflective in the NIR wavelength (>1.0 μm) regions. However, the main benefit of nickel is that compared to other metals (which can be electrodeposited) such as gold, nickel is very inexpensive which makes nickel an ideal candidate to realise MPCs for practical applications. For electrodeposition of nickel, we use commercially available (Bright Nickel Plating Kit, Caswell) electrodeposition kit. The nickel salts provided from Caswell contains mixed components of Nickel Sulfate Hexahydrate ($NiSO_4.6H_2O$) and Nickel Chloride Hexahydrate ($NiCl_2.6H_2O$). Both of the salts are sources of Ni^{2+} ions for electrodeposition. An aqueous electrolyte solution of 20% weight in concentration of nickel salts was prepared for electrodeposition. The pH value was for 4.0. The electrolyte solution was heated to 77^{o}C for activation by using a hotplate with an in-built thermometer and then cooled down to room temperature. To ensure successful infiltration of metal into the polymer woodpile PC template during electrodeposition we followed some steps for treating the PC microstructure template with the electrolyte solution as employed in the previous works [26]. The polymer PC templates fabricated on the ITO glass coverslips were immersed into the electrolyte solution in a vacuum chamber at room temperature and the inside air pressure was slowly reduced to ~ 1 mmHg. In such low pressure the electrolyte solution started to boil. We kept the solution in such low pressure for around 5 minutes and then set the environment back to the standard atmospheric pressure. We followed this procedure for 8-9 cycles for each sample. Such pressure control steps made the polymer PC template surfaces wet by the electrolyte solution due to the volume expansion of the trapped air within the template and reduction of the dissolved air in the electrolyte solution as reported earlier [26]. Effectively, this pressure recycling process ensured free fluidic motion of the electrolyte solution within the polymer PC template during the electrodeposition.

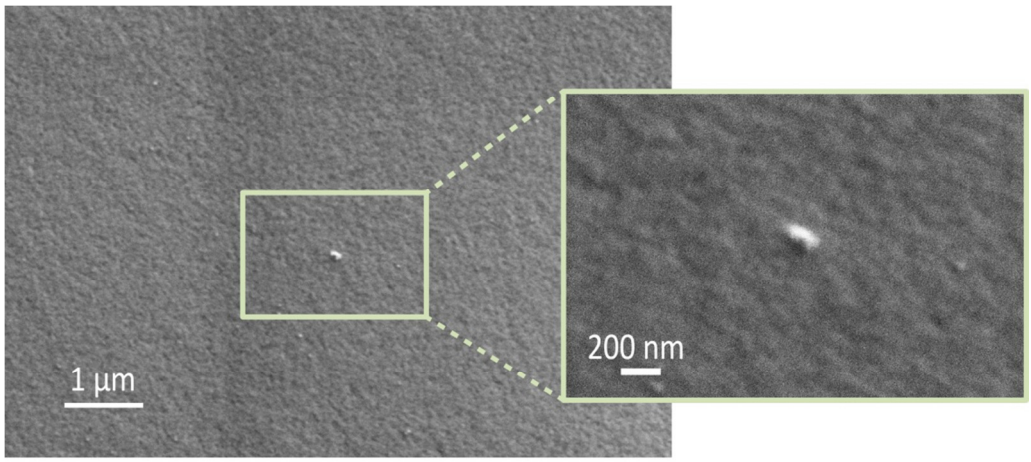

Fig. 4.7 SEM images of an electrodeposited nickel film on an ITO coated glass substrate. Inset shows the magnified view of the high quality nickel film with a dust particle in the middle.

After the pressure cycling procedure, the electrodeposition was performed with an average current density of 1.23 mA/cm^2. Continuous stirring of the electrolyte solution was used during the entire period of electrodeposition. A useful criterion of electrodeposition is that the growth of the nickel film thickness can be controlled as the amount of deposited nickel directly relates with the current density. The electrodeposition was carried out for a period of time when the nickel film thickness reached almost half of the PC template height (as depicted in Fig. 4.6(b)). This made sure that the template was not overfilled by the nickel film. A film thickness of ~1.8 µm was deposited for all the fabricated PC template samples. After the electrodeposition the polymer PC template was left unremoved. Fig. 4.7 shows SEM images (top view) of the high quality electrodeposited nickel films. It should be noted that the quality of the electrodeposited nickel film was much better than that of an electroless metal coating and metal film deposition by the chemical vapour deposition (CVD) technique [43, 80].

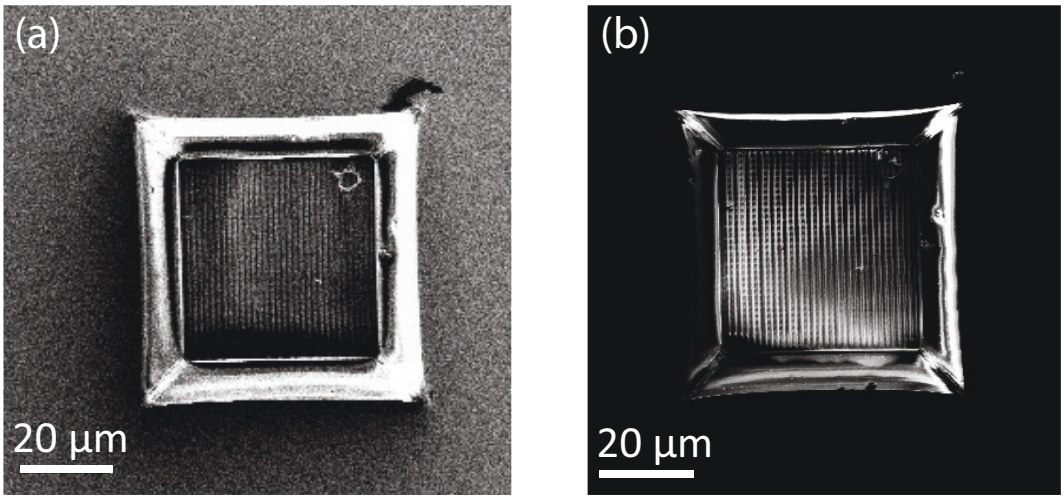

Fig. 4.8 (a) SEM image of a nickel infiltrated woodpile template. (b) High contrast image showing the top layers of the woodpile microstructure.

Fig. 4.8(a) shows the SEM images of the nickel infiltrated woodpile polymer PC template i.e. inversed woodpile nickel MPC. It should be noted that the image was not very clear and also a magnified view of the inversed woodpile MPC was not possible because of the charging effects (the bright illumination forming in the frame in Fig. 4.8(a)) in SEM caused by the top layers and the frame of the polymer PC template. This is due to the fact that the top layers of the PC template were not filled with metal (as can be understood from Fig. 4.6(b)) and hence lacks electrical conductivity. To obtain a clear view of the top layers the same image shown in Fig. 4.8(a) was taken again with greatly reducing the brightness of the sample under the SEM and enhancing the contrast. The polymer rods at the top layer can be clearly viewed in Fig. 4.8(b) due to their greater thickness as obtained by the multiline laser scanning fabrication of woodpile PC template.

4.4 Broad band enhanced absorption in inversed woodpile metallic photonic crystals

In this section, we outline the distinct optical properties of the inversed woodpile nickel MPCs with experimental and theoretical characterisation. We provide experimental demonstration of multiple enhanced absorption peaks over a broad spectral range within the inversed woodpile MPC structures and also support our results with theoretical calculations.

4.4.1 Experimental characterisations

To characterise the optical properties of the MPCs we employed FTIR microscopy for reflection and transmission measurements. A Nicolet Nexus FTIR spectrometer with a continuum IR microscope (Thermo Nicolet, Madison, WI, U.S.A.) was used in our experiments. The reflective 32x NA 0.65 objective (Reflechromat, Thermo Nicolet) provided a hollow light cone with an angle range of 18^{o} to 41^{o}. The incident light on the sample was unpolarised.

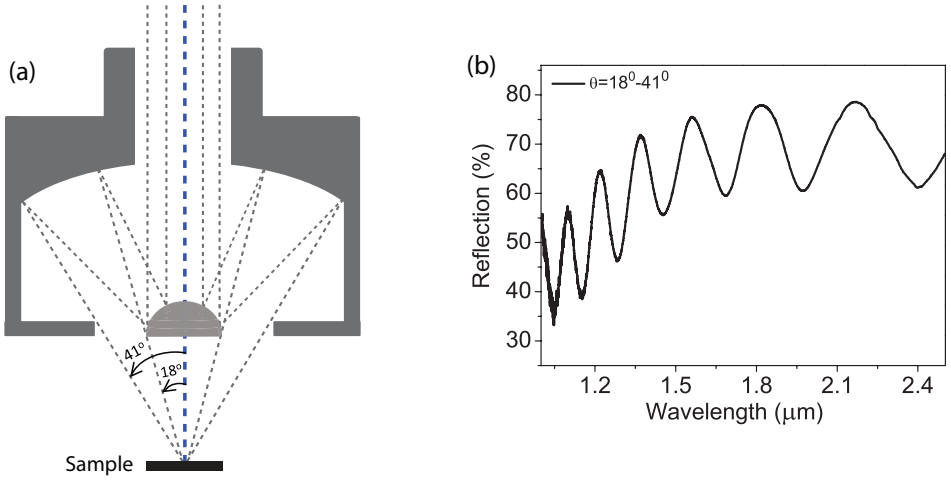

Fig. 4.9 FTIR reflection measurement of the inversed woodpile nickel MPC sample (a) Schematic illustration of the cross-section of the reflective FTIR microscope objective, symmetric around its axis (blue dashed line), depicting the hollow light cone (18^{o} to 41^{o}). (b) FTIR measurement shows multiple strong reflection dips over a broad spectrum.

Fig. 4.9(b) shows the reflection spectra of the inversed woodpile nickel MPC microstructure sample over a broad spectral range. The reflection spectra of the MPC sample were normalised to the reflection of the flat nickel surface outside the sample. The measurement shows a maximum of 80% reflection with multiple reflection dips starting from long wavelengths of 2.4 µm, 1.97 µm and 1.68 µm and so on to the shorter wavelengths. On the other hand a transmission measurement was also carried out for the sample; however, almost no transmission was detected. This clearly suggests that the strong dips in the measured broad reflection spectra i.e. within the wide band gap are caused by the enhanced absorptions within the inversed woodpile MPC.

4.4.2 Theoretical characterisations

To compare the experimental results, we perform numerical calculations based on the finite element method in frequency domain (CST MWS). The dispersive properties of the bulk nickel were adopted from the handbook of optical constants of solids [120]. The same geometrical parameters were assumed in the theoretical calculations as the MPC structural parameters considered in the experiments. The refractive index of IP-L was set to 1.52. A linearly polarized plane wave with an angle of incidence of 25^{o} (to account for the average angle of incidence in the experimental measurement) was used as the source of excitation for the transmission/reflection calculation and periodic boundary conditions were applied in the lateral directions.

Fig. 4.10 shows the calculated reflection and transmission spectra of the MPC structure for the 25^{o} angle of incidence. We observe some important characteristics in our calculation. Firstly, there exist sharp dips in the reflection spectra and secondly, even in the calculated results, the transmission over the entire spectral domain was minimal; only a maximum of 2.9% transmission was

observed at the wavelength of 1.72 μm. Due to this small magnitude, the transmission was not detected within the experimental measurements.

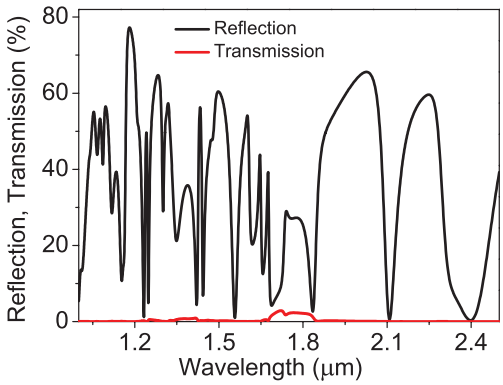

Fig. 4.10 Calculated reflection and transmission spectra of the inversed woodpile nickel MPC with angle of incidence of 25°.

The calculated reflection dips are much higher in strength compared to the experimentally measured ones and caused by the enhanced absorption within the MPC structure. In the experimental measurements with a finite wide opening angle the reflection dips becomes broadened in the spectral width and weakened in magnitude due to the averaging effects. This is also confirmed in the experimental measurement carried out with an opening angle of 18° to 41° as can be found in Fig. 4.9(b). The spectral positions of the calculated reflection dips presented in Fig. 4.10 are fairly comparable to the measured reflection dips in Fig. 4.9(b). Some discrepancies can result from the structural imperfections and also from the broad angle of incidence FTIR spectroscopy measurement.

The comparable results of the experimental and theoretical spectra demonstrate the efficiency of our fabrication method for realising high quality 3D MPC microstructures. In addition, by scaling down the geometrical parameters of the dielectric woodpile PC templates MPC structures with smaller feature sizes could also be achievable.

4.4.3 Enhanced absorptions in the inversed woodpile metallic photonic crystals

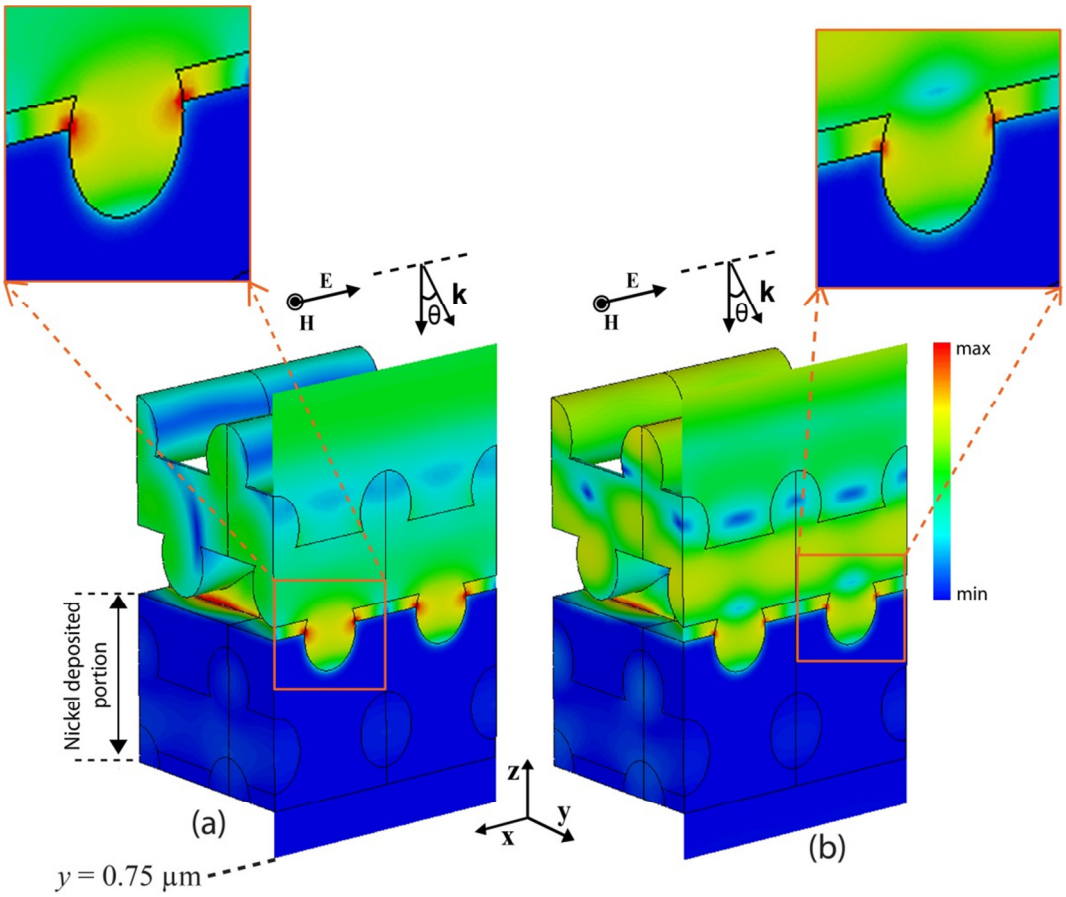

Fig. 4.11 (a) Amplitude plot of the electric field distributions of the reflection dip within the nickel inversed woodpile MPC at λ=2.40 µm (b) Amplitude plot of the electric field distributions of the reflection dip at λ=2.10 µm. The scale bar applies to both figures.

To investigate the absorption peaks within the inversed woodpile nickel MPC structure we investigate the electric field distributions for the first three reflection dips (absorption peaks) starting from the one at the longest wavelength as these reflection dips are fairly comparable to the experimentally measured ones. Fig. 4.11(a) shows the amplitude plot of the electric field distributions for a 25^{o} angle of incidence at the wavelength of 2.40 µm in a 3D format. A cut plane in the *x-z*

cross-section at a certain position of y=0.75 µm within the MPC structure was used to view the interior field distributions. It can be seen that the electric fields couple very strongly to the dielectric cavity formed in the top portion of the deposited nickel film. The fields are strictly bound to the metallic surfaces within the cavity. The polarisation direction of the incident fields and the orientation of the highly enhanced and confined fields within the cavity clearly suggest that the sharp reflection dip formed at the wavelength of 2.40 µm is due to the excitation of the localised cavity plasmon resonance. We then look at the electric fields plot at the second reflection dip at the wavelength of 2.10 µm in the x-z cut plane at the same position of y as in Fig. 4.11(a). The amplitude plot of the electric fields in Fig. 4.11(b) depicts almost a similar type of electric field distributions as in Fig. 4.11(a) where a strong localized field enhancement can be observed. This again suggests an enhanced light-matter interaction with the excitation of localized plasmon resonances and hence, enhanced absorption.

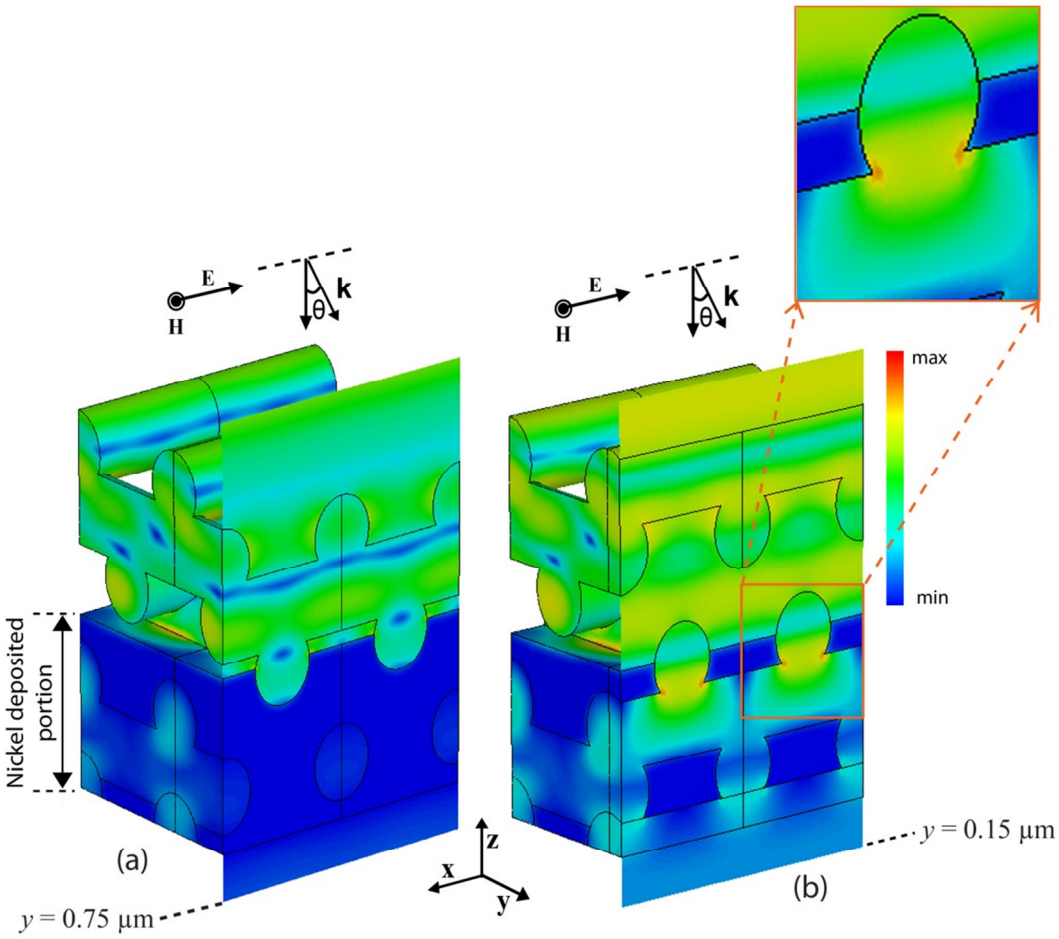

Fig. 4.12 (a) Amplitude plot of the electric field distributions of the reflection dip within the nickel inversed woodpile MPC at λ=1.84 µm (b) Amplitude plot of the electric field distributions at λ=1.84 µm in a different position from (a) within the nickel MPC. The scale bar applies to both figures.

Fig. 4.12(a) shows the electric field distributions of the third reflection dip at the wavelength of 1.84 µm in the *x*-*z* cut plane at the same position of *y*=0.75 µm as in Fig. 4.11. However, no significant field enhancement was observed for this reflection dip. We take another amplitude plot of the field distributions in the *x*-*z* cut plane at a different position of *y*=0.15 µm. Interestingly, a weak field enhancement was observed at the metal-dielectric interface within the cavity formed in the first layer as depicted in Fig. 4.12(b). However, the fields are not totally confined within the cavity rather decouple from the cavity at the end, which indicates the nature of a propagating mode. Indeed, Fig. 4.10 shows that

there exists a transmission peak (although weak in magnitude, the finite transmission indicates a pass band, i.e. propagating modes) at the vicinity of the third reflection dip at the wavelength of 1.84 μm. This suggests that the reflection dip (absorption peak) at the wavelength of 1.84 μm is caused by the enhanced light-matter interaction for the propagating mode at the photonic band edge. For further clarification we have also checked that this propagating nature of the mode does not exist for the first and second reflections dips at the wavelengths of 2.4 μm and 2.1 μm respectively within any *x*-*z* cross-sectional planes of the MPC structure. This certainly confirms that the enhanced absorption at the wavelength of 1.84 μm is due to the periodicity induced enhanced light-matter interaction at the vicinity of the photonic band edge within the MPC environment. Thus the inversed woodpile nickel MPC structure contains unique features of resonant absorptions driven by localised plasmon resonances and also periodicity induced enhanced light-matter interactions within the MPC environment.

4.5 Chapter conclusions

In summary, we have demonstrated a unique low cost fabrication method for realising high quality 3D inversed woodpile MPC microstructures. Our fabrication method presents the novelty of combining the state-of-the-art DLW lithography method for dielectric PC template fabrication and electrodeposition method for metal deposition. The optical properties of the fabricated inversed woodpile nickel MPCs were characterised with experimental measurements and robust optical absorptions were demonstrated. The optical properties of the inversed woodpile nickel MPCs were also characterised with detailed numerical simulations and good agreements were found with the experimental results ensuring the high quality of our MPC microstructures. We have demonstrated enhanced optical absorption over a broad spectral range within our inversed woodpile nickel MPCs. Such MPC structures could be very useful for efficient tailored thermal radiation

emission. In addition, we have also demonstrated resonant optical absorption by localised plasmon resonances associated with robust field enhancement within our 3D MPC structures. Our MPC designs could thus also be useful for applications in plasmonic solar cells.

Our fabrication method for the inversed woodpile MPC is indeed very unique in the sense that the DLW method allows the realisation of polymer PC templates with arbitrary geometries and the electrodeposition method allows the deposition of a range of different metals. Thus, the combination of these two unique methods has the potential of realising 3D MPCs of arbitrary geometries with different metals.

Chapter 5

Nonlinear nanoshell plasmonic waveguides

5.1 Introduction

The true realisation of integrated nanophotonics requires the manipulation and guiding of light with subwavelength mode confinement, zero cross-talk and high nonlinearity. Subwavelength plasmonic waveguides based on surface plasmon polaritons (SPPs) are considered as building blocks for miniaturised nanophotonics circuits [35, 88, 121, 122]. However, total energy confinement and high nonlinearity are still challenging to be achieved in current plasmonic waveguide designs.

Different kinds of plasmon modes other than SPPs at flat metal-dielectric interfaces can also exist in complex metallic nano-structures. The plasmon modes in confined physical geometries can be very different from the SPP resonances on the flat metal-dielectric interfaces. Resonant localised hybrid plasmon modes have been found in spherical metallic nanoshells with embedded dielectric cores [42, 123]. More interestingly, it has been shown that hybrid plasmon modes can also exist in cylindrical metallic nanotubes [124, 125]. In conductive nano-shells (Fig.

5.1) localised plasmon modes can exist at the inner and outer surfaces of the shell and can couple with each other to generate hybrid plasmon modes. The fundamental properties of the hybrid plasmon modes in metallic nanotubes were first analysed by the plasmon hybridisation theory [124] in the electrostatic limit. Later, the retardations effects on such hybrid plasmon modes within the metallic nanoshells were discussed with the retarded plasmon hybridisation theory (RPHT) in our work [125]. These plasmon modes in cylindrical metallic nanoshells can either be stationary or propagating (having a nonzero propagating wavevector along the axis of the metallic nanoshell cylinder) in nature. The potential application of the propagating plasmons lies within their waveguide features.

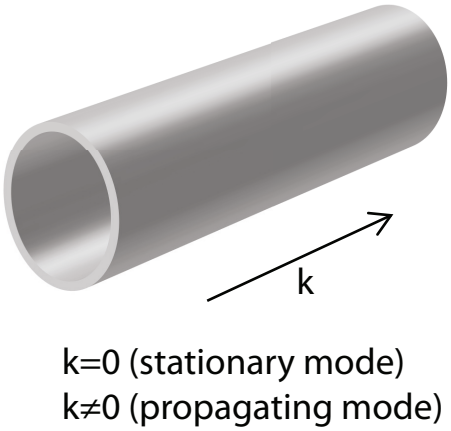

Fig 5.1 Schematic of a metallic nanoshell cylinder.

In this work, we present a novel concept of an ultrahigh nonlinear nanoshell subwavelength plasmonic waveguide based on the propagating plasmon modes in cylindrical metallic nanoshells. The nanoshell plasmonic waveguide consists of a subwavelength elliptic nonlinear core embedded in a metallic nanoshell cladding. The concept for elliptical shape of the nonlinear core for the nanoshell plasmonic waveguide has emerged from the direct laser writing (DLW) fabrication method. DLW fabrication in photosensitive linear and nonlinear (such as chalcogenide glasses) resins can result in elliptic shaped dielectric nanorods which is due to the ellipsoidal focal shape of the fabricating laser within the DLW system (as

previously discussed in Chapter 4). The nonlinear nanoshell plasmonic waveguide provides a unique feature of total energy confinement with moderate propagation length.

Nonlinearity in subwavelength optical waveguides is emerging as another vital feature for realising all-optical high speed signal processing [126]. However, ever since optical waveguides emerged as vital components for communications, the design of waveguides for high nonlinearity and mode energy confinement has been limited by two factors: the effective mode area and the nonlinear index coefficient n_2 of the waveguide bulk material itself. To greatly enhance the Kerr nonlinearity, a dramatic reduction of the effective mode area is required. A major problem of the current dielectric nonlinear waveguides is the inability of confining the mode beyond the fundamental diffraction limit. On the other hand, plasmonic waveguides provide mode confinement beyond the diffraction limit; however, they are not explored for potential applications in nonlinear optics. Here, we propose that our nanoshell plasmonic waveguide can possess an ultrahigh Kerr nonlinearity and thus has the potential to be a unique candidate for realising novel nonlinear optical devices. Our results show that instead of scaling down the actual physical size of the waveguide cross-section, altering geometrical and physical parameters of the device can dramatically change the distribution of the fields to induce the ultrahigh nonlinearity [127].

The uniqueness of the nonlinear nanoshell plasmonic waveguide is that it possesses three distinctive features. Firstly, it creates a subwavelength cross sectional confinement of the plasmon mode with an effective mode area as small as 0.0196 μm^{-2}. Secondly, nearly 100% of the total mode energy can be confined within the subwavelength waveguide. Thirdly, the vectorial nature of the electromagnetic (EM) fields within the cylindrical subwavelength waveguide results in significant increase of the optical Kerr nonlinearity which reaches up to 4.1×104 $W^{-1}m^{-1}$ [127]. Our results show that this new class of nonlinear nanoshell plasmonic waveguides could lead to the realisation of truly ultra-compact, high-

density, integrated nanophotonic devices. The ability of combining the total mode energy confinement and the ultrahigh nonlinearity in a single nanophotonic component allows the nonlinear nanoshell subwavelength plasmonic waveguide to be potentially used in nonlinear optical switching [46, 52], plasmonic modulation [53, 54], higher order nonlinear signal generation [128], micro-fluidic sensing, and nano-lasers [56, 57] etc. Importantly, our considered plasmonic waveguide is also realisable with current fabrication technology.

This chapter is divided into six sections. Section 5.1 introduces the novel concept of our metallic nanoshell plasmonic waveguide. Section 5.2 discusses the subwavelength mode confinement ability of the nanoshell plasmonic waveguide and discusses its unique property of total energy confinement over other plasmonic and dielectric waveguides. Section 5.3 discusses the mode characteristics of the nanoshell plasmonic waveguide. Section 5.3.1 highlights the dispersive properties of the nanoshell plasmonic waveguide. Section 5.3.2 concentrates on the effects of the metallic shell thickness on the mode confinement characteristics.

Nonlinearity in optical waveguides is a very attractive feature for various potential photonics applications. However, dielectric waveguides are constrained to possess high optical nonlinearity due to their poor mode confinement ability. In Section 5.4 we discuss the scope of our plasmonic waveguide possessing ultrahigh Kerr nonlinearity. The vectorial profile of the plasmon mode, the variation of the optical properties with geometrical alterations and the effect of dispersions are investigated in details.

Chalcogenide glasses are novel type of materials which also possess very high nonlinear index coefficient among available highly nonlinear materials. Chalcogenide glasses can be processed to yield subwavelength nanowires. In Section 5.5 we discuss the potential applications of chalcogenide nanowires as

core elements in our nanoshell plasmonic waveguides with an ultrahigh nonlinearity. Section 5.6 provides the conclusions of this chapter.

5.2 Total energy confinement in nanoshell plasmonic waveguides

Confining the mode energy totally within the waveguide cross-section becomes a great challenge when approaching the subwavelength regime. Due to the fundamental diffraction limit, the mode energy cannot be confined to dielectric waveguides with subwavelength core sizes. Taking as an example, we consider a silicon waveguide, embedded in air, with a 200 nm core width and an aspect ratio of 3. The profile of the fundamental mode within the waveguide operating at a free-space wavelength of 1.55 μm is numerically calculated (COMSOL Multiphysics) and depicted in Fig. 5.2(a). The energy density distribution at the waveguide cross-section illustrates the good mode confinement. However, dielectric waveguides can only confine light to wavelength-sized dimensions due to the fundamental diffraction limit. As can be found in Fig. 5.2(b), for the same waveguide of half the size (100 nm core width and with the same aspect ratio) the mode energy is no longer tightly confined to the sub-wavelength core with most of the energies spreading out into the nearby environment. This limits dielectric waveguides attaining a small effective mode area and also raises practical issues for the development of high-density integrated nanophotonic chips, due to the coupling of these modes with other nearby components. For comparison, the waveguide shown in Fig. 5.2(a) has 77.4% mode energy inside the silicon core, whereas, the waveguide shown in Fig. 5.1(b) contains less than 1% (0.22%) of mode energy inside the silicon core.

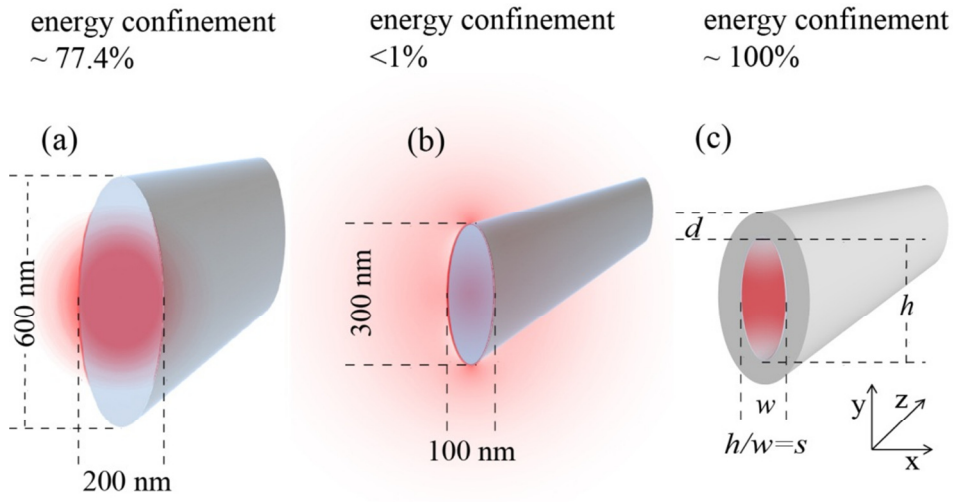

Fig. 5.2 Concept of the nanoshell plasmonic waveguide and associated total energy confinement. (a, b) Mode energy density distribution of a silicon waveguide with an aspect ratio of 3, calculated numerically for a 200 nm and a 100 nm core width respectively. (c), Mode energy distributions for a nanoshell plasmonic waveguide with a silicon core with w=100 nm, and a silver nanoshell of d=50 nm and an aspect ratio of s=3.

On the other hand, plasmonics provides an unmatchable ability to confine fields far beyond the diffraction limit [4, 35, 124]. SPPs can facilitate guiding light with concentrated EM energies at the metal-dielectric interfaces [35, 51, 88]. However, confining the mode energy completely within the waveguides physical region is very important for realising compact integrated nanophotonic components with zero-crosstalk, which has not been addressed in both the current dielectric and plasmonic waveguide designs [126, 129, 130].

Our geometry of interest shown in Fig. 5.2(c) is a metallodielectric plasmonic waveguide where a cylindrical nonlinear dielectric core is embedded within a silver metallic nanoshell [43, 80]. The core has a cross sectional width w, height h, an aspect ratio s (where s is defined as h/w) and the nonlinear core is considered as silicon with a bulk refractive index of 3.48 and a nonlinear refractive index coefficient n_2 of 14.5×10^{-18} m^2/W [131]. The silver metallic shell was considered to have a complex refractive index $n + ik$ of 0.145263+11.3587i [132] and has a

thickness of *d*. The eigenmodes were extracted numerically with the finite element based eigenmode solver (COMSOL Multiphysics) within the plasmonic waveguide at the telecommunications free-space wavelength of 1.55 μm. Fig. 5.2(c) demonstrates the mode energy distribution for the plasmonic waveguide with the same core size as in Fig. 5.2(b) but with a 50 nm silver coating. The mode energy is tightly confined within the dielectric core of the waveguides as such almost all the mode energies reside within the waveguide. Due to the ellipsoidal symmetry of the waveguide structure the single fundamental mode is x polarised and thus the strong discontinuity of the normal component of the electric fields at the metal-dielectric interface creates an ultrahigh mode confinement. For plasmonic waveguides, the total amount of mode's energy residing within the waveguide's physical region along with the subwavelength confinement is one of the important features. The nanoshell plasmonic waveguide contains 97.7% of its mode energy within the dielectric core and 99.9% of its mode energy is confined within the waveguide including the metallic shell. This is clearly a distinguishing feature of the nanoshell plasmonic waveguide over the current plasmonic waveguide geometries. For example, the state-of-the-art silicon nanowire waveguides [129, 130] and hybrid plasmonic waveguides [88] do not possess such total confinement. The nanoshell plasmonic waveguide with total energy confinement at deep subwavelength scale has the potential to be used as the building blocks to realise ultra-compact integrated nanophotonic devices with minimal cross-talk.

5.3 Mode characteristics of nanoshell plasmonic waveguide

5.3.1 Dispersion characteristics of the nanoshell plasmonic waveguide

Here we investigate the dispersive properties of the plasmonic waveguide to understand the fundamental features of the plasmon modes. We characterise the dispersive properties of the plasmon modes in the nanoshell waveguide as compared to the basic SPPs in flat metal-dielectric interface. The SPP modes were considered for a flat silver-silicon interface and the geometry of the nanoshell plasmon waveguide was the same as in Fig. 5.2(c). Due to the lacking of experimentally measured data in the long wavelengths and to express the dispersive properties in terms of the bulk plasma frequency ω_p we adopt the Drude dispersive model to characterise the fundamental properties of silver. COMSOL Multiphysics numerical tool was used to extract the eigen frequencies of the plasmon modes. The silver metal was considered with a bulk Drude plasma frequency of 1.37×10^{16}/s and a damping frequency of 2.73×10^{13}/s [80]. Fig. 5.3 shows the dispersions of the nanoshell plasmonic waveguide modes for a 100 nm width silicon core with a comparison to the SPP modes of a silver-silicon interface.

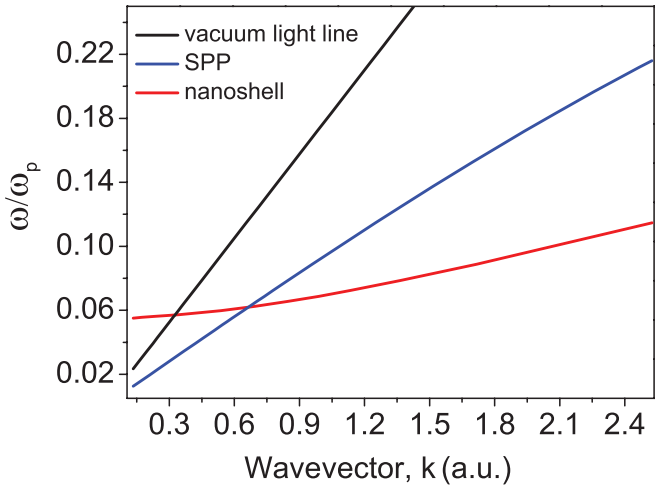

Fig. 5.3 Dispersion relations of the plasmon mode in the nanoshell plasmonic waveguide with a silicon core (red) and SPP mode at the silicon-silver interface (blue).

Interestingly, the frequencies of the plasmon modes of the nanoshell plasmonic waveguide falls on the both sides of the vacuum light line capable of supplying wavevectors either smaller or greater than the vacuum wavevector. This effectively states that the modes on the right hand side of the light line (with $k>\omega/c$) are nonradiative and the modes falling on the left side of the light line (with $k<\omega/c$) are radiative while the SPP modes on flat metal-dielectric interfaces are nonradiative only [3] as discussed in section 1.2.1. Moreover, the dispersion curve of the nanoshell plasmonic waveguide is quite flat compared to that of the SPPs for the same bulk materials (i.e. silicon and silver). Furthermore, it is obvious from Fig. 5.3 that nanoshell plasmonic waveguides can provide higher wavevectors quite flexibly than the SPPs at the same frequency. As the high wavevectors within a waveguide yield small effective wavelengths, the nanoshell plasmonic waveguides can be used to realise miniaturised photonic components for nano-photonic chips.

5.3.2 Effect of metallic shell thickness on energy confinement

The dependence of the mode confinement on the nanoshell thickness d is further illustrated by the normalised electric field shown in Figs. 5.4(a)-5.4(c). For a metallic shell with thickness < 50 nm the coupling between the plasmons of the inner and outer surfaces of the metallic shell becomes stronger and results in hybridisation of the plasmon modes causing the fields to spread outside of the nanoshell as depicted in Figs. 5.4(a) and 5.4(b). On the other hand, Fig. 5.4(c) demonstrates that for metallic shell thickness ≥ 50 nm, the coupling between the plasmons of the two surfaces becomes almost negligible and the mode is strictly confined within the dielectric core.

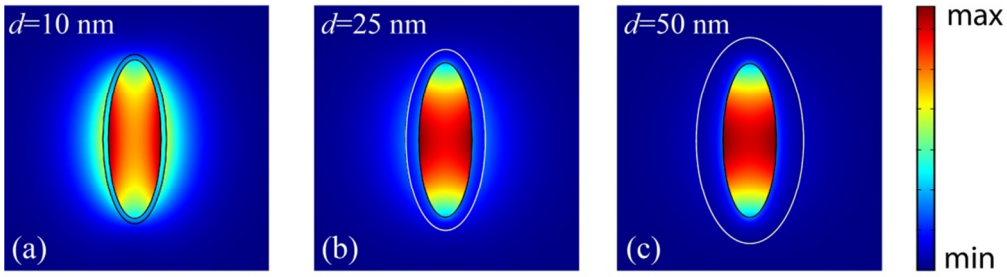

Fig. 5.4 Effect of the shell thickness on the mode confinement. (a) The normalised electric field |**E**| of the plasmon mode for a 10 nm thick silver shell on the silicon core, showing large leaking of the fields outside of the waveguide. (b) |**E**| for a 25 nm silver shell, showing less field leakage. (c) |**E**| for a 50 nm thick silver shell, showing minimal field leakage and leading to nearly total confinement of the fields to the nonlinear core region.

5.4 Ultrahigh nonlinearity in silicon core nanoshell plasmonic waveguides

5.4.1 Nonlinear waveguides

The exciting promise of integrated nanophotonics has led to the development of miniaturised, highly nonlinear and highly confined photonic components. Recent advancement in the state-of-the-art nanofabrication facilities have led to the development of optical waveguides with subwavelength features and inhomogeneous cross-sections, providing enhanced optical nonlinearities and small effective mode areas [126, 129, 130]. However, dielectric nonlinear waveguides have reached their maximum potential in achieving high nonlinearity due to the limitation of mode confinement beyond the diffraction limit. Our results show experimentally realisable [43, 80] geometrical alterations of the plasmonic waveguide can dramatically change the distribution of the fields from the induced dispersion and yield an ultrahigh Kerr nonlinearity. We theoretically demonstrate that our subwavelength nanoshell plasmonic waveguide with a nonlinear silicon core can possess an ultrahigh Kerr nonlinearity up to 4.1×10^{4} $W^{-1}m^{-1}$ at λ=1.55 μm. The optical properties are explored with detailed numerical simulations and are explained in terms of their dispersive properties.

5.4.2 Vectorial mode profiles of the plasmonic waveguide and enhanced nonlinearity

It has been demonstrated that the definition for the effective nonlinearity with weak guidance approximation [133] fails for today's state-of-the-art subwavelength inhomogeneous cross sections i.e. for strong guidance nonlinear optical waveguides. The subwavelength plasmonic waveguide holds its vectorial

nature by having non-negligible longitudinal components of the modal fields which is depicted in Fig. 5.6.

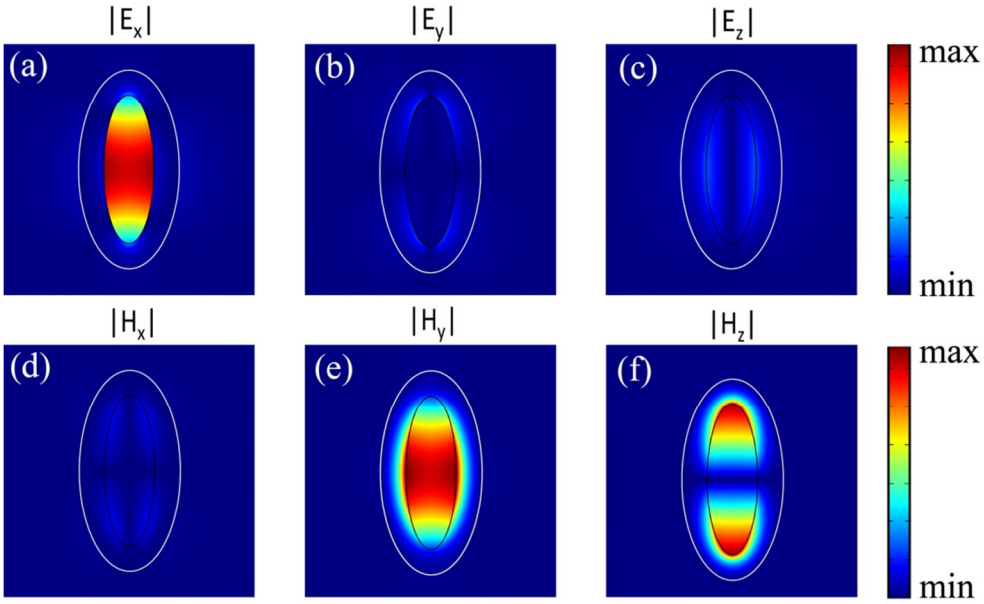

Fig. 5.5 Vectorial plots of the modal fields of the nanoshell plasmonic waveguide with a silicon core of width w=100 nm, silver nanoshell of thickness d=50 nm and aspect ratio of s=3. (a-c) Spatial distributions of the absolute values of E_x, E_y, E_z, components. (d-f) Spatial distributions of the absolute values of H_x, H_y, and H_z components.

The vectorial nature of the modal fields requires that a full vectorial model should be adopted to accurately predict the Kerr optical nonlinearity. A number of formulations have been developed to correctly predict the effective nonlinearity in such small core waveguides [129, 134-136]. A generalised full vectorial-based nonlinear Schrodinger equation (VNSE) was developed to accurately predict the pulse propagation within subwavelength and inhomogeneous nonlinear waveguides [134] and experimental results [137] have already confirmed the added accuracy for correctly predicting the Kerr nonlinearity over conventional models. According to the vectorial model, the Kerr nonlinear optical coefficient of a single-mode highly birefringent waveguide is given by [134]

$$\gamma = k_0 \frac{\bar{n}_2}{A_{eff}}, \tag{5.1}$$

where

$$A_{eff} = \frac{\left| \int \left(\mathbf{E} \times \mathbf{H}^* \right) . \hat{z} \, dA \right|^2}{\int \left| \left(\mathbf{E} \times \mathbf{H}^* \right) . \hat{z} \right|^2 dA}, \tag{5.2}$$

and

$$\bar{n}_2 = \left(\frac{\varepsilon_0}{\mu_0} \right) \frac{\int n^2(x,y)\, n_2(x,y) \left[2|\mathbf{E}|^4 + \left| \mathbf{E}^2 \right|^2 \right] dA}{3 \int \left| \left(\mathbf{E} \times \mathbf{H}^* \right) . \hat{z} \right|^2 dA}, \tag{5.3}$$

where **E** and **H** are the electric and magnetic vector fields of the propagating mode and n(x,y) and n_2(x,y) are the linear and nonlinear refractive index distributions with respect to the waveguide cross-sections. The effective mode area A_{eff} represents a statistical measure for the mode energy density distribution. The effective mode area also reflects the full vectorial nature of the modal fields as opposed to the scalar field definition [133]. The statistical definition for A_{eff} provides the complete EM mode area compared to its counterparts [88] which are completely inaccurate to express the nonlinearity within a waveguide. The effective nonlinear refractive index coefficient $\bar{n}_2$ is weighted with respect to the modal field distributions over the inhomogeneous waveguide cross-sections. Equation 5.3 is directly used here to calculate $\bar{n}_2$. In all our considered waveguide geometries the strength of the electric fields within the metallic regions are much less than that in the dielectric core, and as the effective Kerr nonlinearity measures on the 4$^{\text{th}}$ power strength of the electric fields we can neglect any nonlinear contribution of the metallic portions of the waveguides.

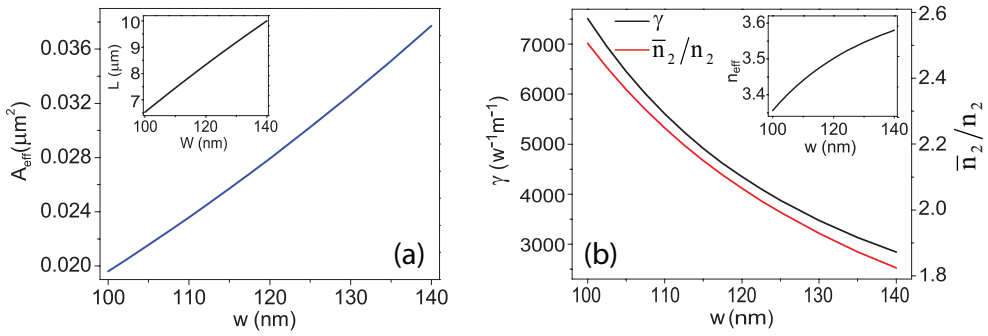

Fig. 5.6 Calculated effective mode area, Kerr nonlinearity (γ) and normalised effective nonlinear index coefficient ($\bar{n}_2/n_2$) of the plasmon mode for d=50 nm and s=3. (a) Calculated A_{eff} of the plasmonic waveguide for varying w. Inset: The propagation lengths of the plasmon mode for varying core width. (b) Calculated γ and $\bar{n}_2/n_2$ of the nanoshell plasmonic waveguide. Inset: Calculated effective mode indices (n_{eff}) over a range of w.

It is clear from Fig. 5.6(a) that the mode possesses an ultra-small effective mode area due to the plasmonic confinement of the system. For a core width of 100 nm, A_{eff} of the nanoshell plasmonic waveguide is 0.0196 μm^2, which, to the best of our knowledge, is the smallest effective mode area (based on the statistical measure) so far for optical waveguides at the wavelength of 1.55 μm. The inset of Fig. 5.6(b) shows the propagation length of the plasmon mode is less than that of the SPP modes (~24.5 μm at 1.55 μm wavelength) at silver-silicon interface. These higher losses arise from the strong localisation of the fields within the metallic nanostructure. However, the highly subwavelength localisation and total energy confinement of the nanoshell plasmonic waveguides make them unique candidates for photonic integration on the nanoscale. Further decrease of the core width leads to smaller effective mode areas and larger nonlinearity, however, this also greatly increases the propagation loss. Here we have restricted the results to a regime where the propagation length is of practical use.

Even though the nonlinearity γ is inversely proportional to A_{eff}, surprisingly, our results show that γ increases at a faster rate than the decreasing rate of A_{eff}. The reason behind this enhanced increasing rate is that the effective nonlinear index coefficient $\bar{n}_2$ of the nanoshell plasmonic waveguide is much larger than the bulk

n_2, which has not been reported before. Figs. 5.6(a) and 5.6(b) show that as the core width decreases from 140 nm to 100 nm [43], A_{eff} decreases 0.52 times while $\bar{n}_2$ increases 1.37 times (from 1.82 to 2.506 times the bulk silicon n_2). Thus, the combined effect of A_{eff} and $\bar{n}_2$ enhances the optical nonlinearity γ to 2.64 times and reaches a highly enhanced value of 7514 $W^{-1}m^{-1}$. Undoubtedly, $\bar{n}_2$ plays an intriguing role to stimulate the γ value of the nanoshell plasmonic waveguide which can demonstrate an ultrahigh optical nonlinearity.

5.4.3 Ultrahigh nonlinearity with geometrical alteration

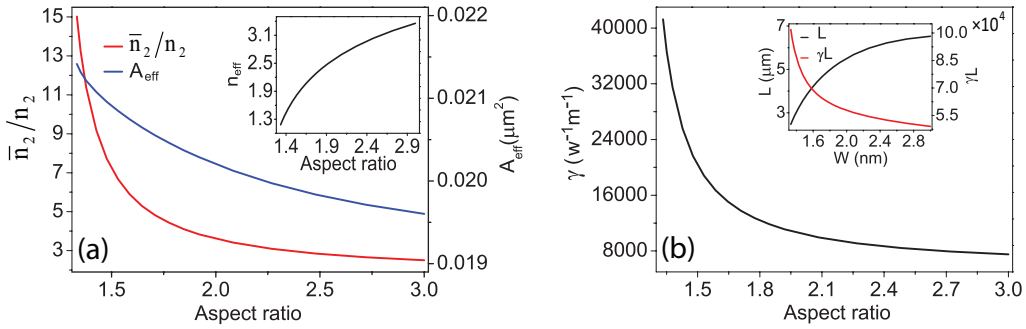

Fig. 5.7 Characteristics of the effective nonlinear index coefficient ($\bar{n}_2/n_2$), mode area A_{eff}, and Kerr nonlinearity γ for d=50 nm and varying s while the nonlinear silicon core cross-sectional area was kept the same as the smallest core size depicted in Fig. 5.6. (a) The normalised $\bar{n}_2$ and A_{eff} for decreasing aspect ratios of plasmon waveguide. Inset: the n_{eff} versus aspect ratio s. (b) Kerr nonlinearity as a function of aspect ratios of the plasmonic waveguide with a silicon core. Inset: propagation length L and product of γ and L as a figure of merit.

We now turn our attention to the dependence of this nonlinear enhancement on geometrical properties via the variation of the waveguide core aspect ratio s. The cross-sectional area of the nonlinear core was kept constant over the entire range of the variation of the aspect ratios which is equal to the cross-sectional area smallest nonlinear core (with a core width of 100 nm) presented in Fig. 5.6. Here we restrict our results to the modes with an effective mode index n_{eff}>1 where the plasmon mode wavevector k_{mode}>k_0 ($k_{mode}\rightarrow n_{eff}k_0$ [27]). Fig. 5.7(a) shows that

$\bar{n}_2/n_2$ increases from 2.51 to 15.03 as the aspect ratio decreases from 3 to 1.333. Once again, the ultra-small but almost constant values of A_{eff} clearly confirm that it is not A_{eff} that plays the dominating role to significantly enhance the nonlinearity rather it is $\bar{n}_2$ of the waveguide core. Fig. 5.7(b) shows that γ reaches an ultrahigh value of 41251.05 $W^{-1}m^{-1}$ for an aspect ratio of 1.333. For a fair comparison of the enhancement of γ we compare with other highly nonlinear optical waveguides with the same waveguide core material. Our results show that this ultrahigh value of γ in our plasmonic waveguide is 25 times higher than that of the state-of-the-art nonlinear silicon-on-insulator slot waveguide [129]. It is important to note that even at this ultrahigh nonlinearity the mode contains 99.1% of energy within the entire waveguide region. It is the strong lateral localisation of the nanoshell plasmonic waveguide that provides almost all the mode energy confined within the tiny silicon core with immense nonlinearity. In contrast, other geometries such as the hybrid plasmonic waveguide [88] contain only 15 to 20% of the mode energy within the low index dielectric region for the mode confinement. As a result, our nanoshell plasmonic waveguide geometry is more suitable for ultrahigh nonlinear interactions with nearly total energy confinement as well as minimal cross-talk at a subwavelength scale.

It can also be noticed from the inset of Fig. 5.7(b) that the propagation length decreases with a reduction of aspect ratios, giving a trade-off between ultrahigh nonlinearity and propagation length. As a figure of merit, we plot the product of the nonlinearity and propagation length in the inset of Fig. 5.7(b) which shows a gain of a factor of two for decreasing aspect ratios. Further decrease of the aspect ratio of the nonlinear core leads to even greater enhancement of the Kerr nonlinearity, however, in this regime; the propagation length of the mode becomes less than the wavelength of operation. Thus we have not included these results here.

5.4.4 Origin of the ultrahigh nonlinearity

To understand further the physical reason for the dramatic enhancement of the optical nonlinearity of the nanoshell plasmon waveguide we inspect the variation of the magnitude of the modal fields. The effective nonlinear coefficient $\overline{n}_2$ is inversely proportional to the integral of square of the power flow along the propagation direction as can be followed form equation 5.3. The denominator in Equation 5.3 determines the enhancement of $\overline{n}_2$ and can be written as

$$\int \left| \left(\mathbf{E} \times \mathbf{H}^* \right) . \hat{z} \right|^2 dA = \int \left| E_x H_y^* - E_y H_x^* \right|^2 dA . \tag{5.4}$$

For the nanoshell plasmonic waveguide the mode is x polarised and thus the modal fields E_x and H_y are strongly dominant over the E_y and H_x fields respectively. Thus the second term inside the integral of the right hand side of the above equation involves the product of the weak modal fields and thus can be ignored. So, Equation 5.4 can be re-written as

$$\int \left| \left(\mathbf{E} \times \mathbf{H}^* \right) . \hat{z} \right|^2 dA \approx \int \left| E_x \right|^2 \left| H_y^* \right|^2 dA . \tag{5.5}$$

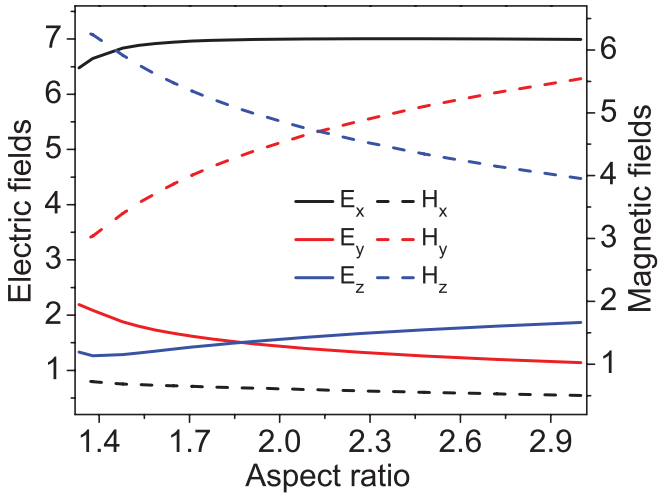

Fig. 5.8 Magnitude of the modal field components of the plasmon mode for d=50 nm and varying s while the nonlinear core cross-sectional area was kept same as in Fig. 5.7.

The z component of the power flow relies on the lateral components E_x and H_y. Fig. 5.8 depicts the magnitudes of the modal fields for the changing aspect ratios i.e. for the varying wavevector. The field components $E_i(i = x, y, z)$ were normalized to $|\mathbf{E}|$ (i.e. $\int E_i dA / \int |\mathbf{E}| dA$) for each values of the aspect ratios. The E_x component is dominant over the other components of the electric fields over the whole aspect ratio range. On the other hand, both the H_y and H_z components contribute for the high aspect ratio. However, as the aspect ratio decreases, H_z becomes dominant over H_y, as can be found in Fig. 5.8 for the aspect ratio of 1.333. The reduced magnitude of H_y drastically weakens the energy flow along the propagation direction and effectively yields a much higher value of $\bar{n}_2$ for the low aspect ratio. The increase of H_z component of the magnetic field for low aspect ratios is reasonable from the variation of the effective mode index n_{eff} shown in the inset of Fig. 5.7(a). This feature states that the n_{eff} value of the plasmon mode reduces for decreasing aspect ratios, indicating the reduction of the plasmon mode wavevector, i.e. it approaches the stationary limit (i.e. $k_{\text{mode}} \rightarrow 0$) when the aspect ratio is reduced.

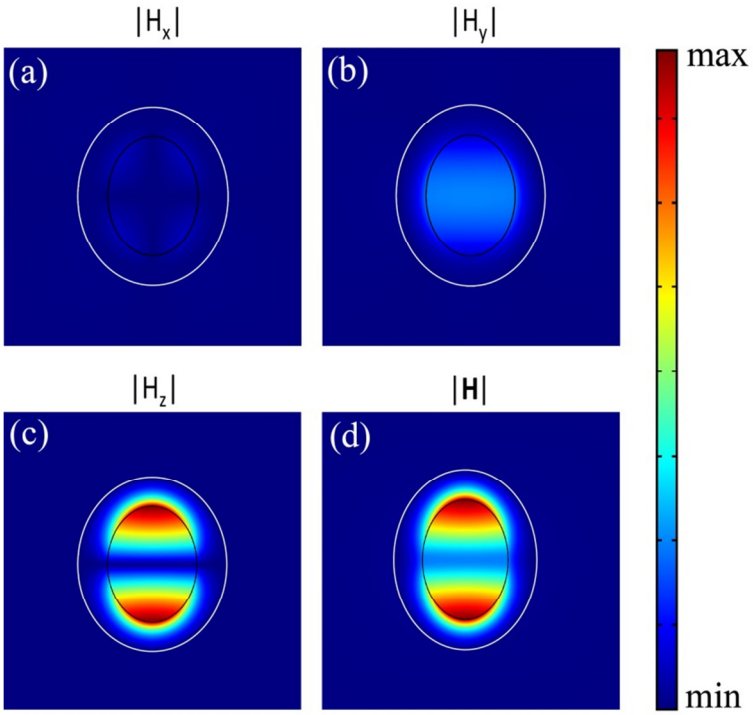

Fig. 5.9 (a,b,c) Spatial distributions of the H_x, H_y and H_z components of the magnetic fields respectively of the plasmon mode for an aspect ratio of 1.333. (d) Spatial distribution of the absolute value of the magnitude field **H** which resembles to H_z as it is the dominating component at low aspect ratio.

In the limit of $k_{mode} \rightarrow 0$, the mode becomes stationary and the current density flows only along the azimuthal direction within the metallic nanoshell cross section. This rotational current flow in the two dimensions causes the magnetic fields to be directed purely along the propagation direction. Fig. 5.8 evidently demonstrates the growing dominance of H_z over H_y for reducing plasmon wave vector (i.e. for approaching to the stationary limit) and illustrates the enhancement of the optical nonlinearity. Figs. 5.9(a)-5.9(d) show the distributions of the magnetic field components and the magnitude of the corresponding total magnitude fields at the lowest aspect ratio of 1.333 and depict the dominance of H_z over H_y.

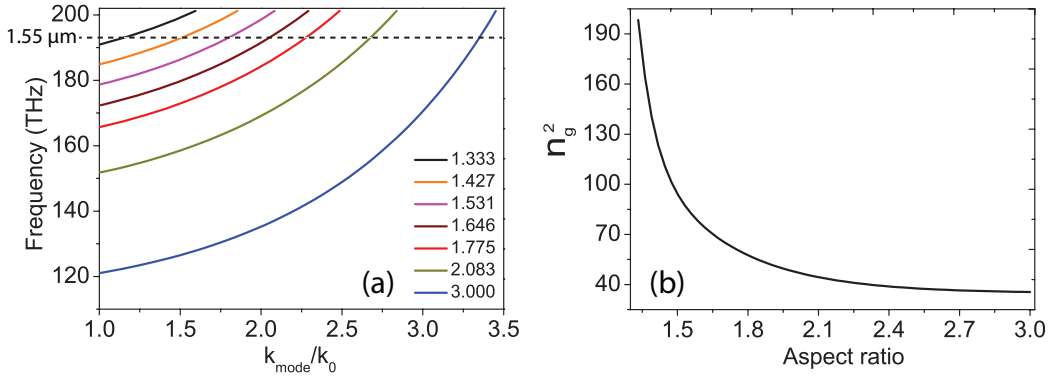

Fig. 5.10 Dispersion relation of the plasmon mode approaching the stationary limit at 1.55 µm for d=50 nm and varying s while the nonlinear core cross-sectional area was kept same as in Fig. 5.7. (b) Square of the group index as a function of s for the plasmonic waveguide with a silicon core.

An alternative explanation of the enhancement of the effective nonlinear coefficient $\bar{n}_2$ can be derived by analysing the dispersive properties of the nanoshell plasmonic waveguide for varying aspect ratios. We investigate the dispersive properties of the nanoshell plasmonic waveguide by using the eigenmodes and analyse the relation with the group velocity [138]. Fig. 5.10(a) depicts the dispersion of the plasmon modes for a range of aspect ratios. Interestingly, for the transition from high to low aspect ratios, where the plasmon modes approach the stationary limit, the dispersion curves flatten out. As pointed out in Fig. 5.10(a) at the wavelength of 1.55 µm the dispersion curve is almost flat for the low aspect ratio of 1.333 which indicates a very small group velocity in contrast to the high group velocity for the high aspect ratio of 3. The square of the group index ($n_g \rightarrow c/v_g$) of the nanoshell plasmon modes over the varying values of the aspect ratio, shown in Fig. 5.10(b), exactly replicates the trend of the optical Kerr nonlinearity in Fig. 5.7(b), illustrating the role of the reduction of the group velocity for the ultrahigh nonlinearity. This large group index greatly prolongs the nonlinear interaction between light and matter i.e. induces the enhanced nonlinear index coefficient $\bar{n}_2$ of the system and hence, yields the ultrahigh Kerr nonlinearity.

5.5 Kerr nonlinearity in chalcogenide core nanoshell plasmonic waveguide

Novel nonlinear optical materials are always of interest to the photonics community for their potential applications in telecommunications. Although a number of high refractive index materials along with high nonlinearity are available, the expensive and stringent fabrication methods for producing miniaturised components with those nonlinear materials hinder the rapid development of nanophotonic devices for telecommunications. Moreover, the promising applications of the nonlinear materials require high optical transmission in the near infrared (NIR) wavelengths [139].

Chalcogenide glasses are considered as one of the most promising materials due to their distinctive properties of high refractive index, high optical nonlinearity, and high optical transmission which allow them to be used as the building blocks for the realisation of future integrated nanophotonic chips. Moreover, these materials are photosensitive and can be polymerised with state-of-the-art DLW fabrication method [117, 140]. This allows realising novel nanophotonic devices of chalcogenide glasses with flexible and cheap fabrication procedures rather than expensive fabrication methods such as the electron beam/ion beam lithography.

Recently, a remarkable experimental study has demonstrated the realisation of $\lambda/12$ resolution of chalcogenide nanowires [111]. Using a DLW method chalcogenide nanowires of width as small as 68 nm was achieved [111]. This kind of highly nonlinear photonic nanowires opens new window for subwavelength nonlinear optical waveguides. Here, we theoretically explore the potential applications of such chalcogenide nanowires for highly nonlinear subwavelength plasmonic waveguides. The chalcogenide nanowires have elliptical cross-sections due to the elongated nature of the laser focal spot in DLW fabricating system and this exactly fits the geometry of our nanoshell nonlinear plasmonic waveguide.

Chalcogenide glass has linear refractive index of 2.405 and nonlinear coefficient n_2 of $6.1\times10^{-18}m^2/W$ [141]. We calculate the effective mode area, propagation length, effective mode index and Kerr nonlinearity within the chalcogenide nanowire based nanoshell plasmonic waveguides for varying core sizes at the wavelength of 1.55 µm. The chalcogenide nanowire cross-section is assumed to have an aspect ratio of three and the silver shell thickness on top of the chalcogenide nanowire is considered to be 50 nm. The chalcogenide nanowires with different aspect ratios can be realised experimentally via the multiple line laser scanning in the DLW fabrication method [112, 117].

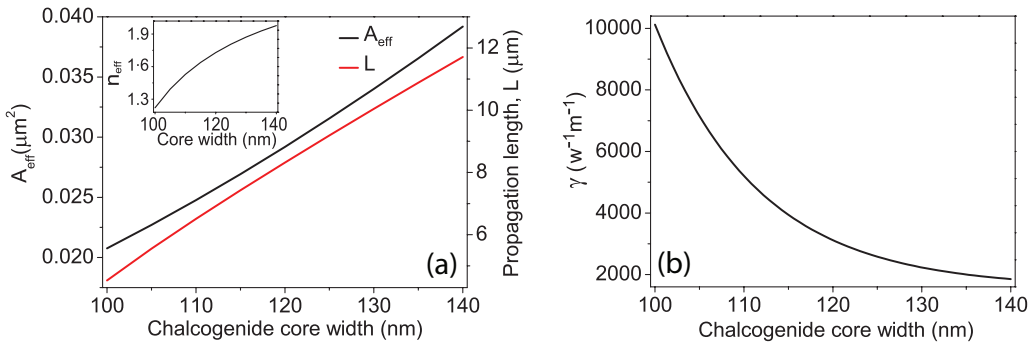

Fig. 5.11 (a) Calculated effective mode area (A_{eff}) and propagation length (L) of the plasmonic waveguide for varying chalcogenide core width. Inset: The effective mode index (n_{eff}) as a function of the core width. (b) Kerr nonlinearity (γ) for varying core width.

Fig. 5.11(a) shows that the chalcogenide nanowire based nanoshell plasmonic waveguide can possess effective mode area as small as 0.208 μm^2 for a 100 nm core width. Scaling down the chalcogenide core size less than 100 nm would reduce the effective mode area at the wavelength of 1.55 µm. However, we restrict the calculation results in the limit of $n_{eff}>1$. Moreover, beyond this regime the propagation loss becomes significant. Fig. 5.11(b) shows that for a smallest waveguide core size of 100 nm, an ultrahigh Kerr nonlinearity of 10226 $W^{-1}m^{-1}$ is achievable.

5.6 Chapter conclusion

In summary, we have demonstrated a novel class of plasmonic waveguide with deep subwavelength mode confinement. For the first time, we have shown that nearly 100% mode energy confinement is achievable in a metallic nanoshell nonlinear plasmonic waveguide. In comparison to the existing state-of-the-art dielectric and plasmonic waveguide geometries this is, indeed, an important improvement for realising zero cross-talk nanophotonic components towards the integrated photonic circuits.

We have theoretically demonstrated that an ultrahigh nonlinearity up to 41,251 $W^{-1}m^{-1}$ can be achieved due to the significant enhancement of the effective nonlinear index coefficient along with the subwavelength confinement by controlling the geometrical properties of the plasmonic waveguide. The combined properties of the enhanced nonlinearity, the subwavelength mode area and complete mode energy confinement forms an excellent nanoplasmonic platform for the realisation of high-density photonic integration of nonlinear optical switching [46, 52], higher order nonlinear signal generation [128] all-optical modulators [67], nano-lasers [56, 57] and gain assisted plasmonic propagation [142].

Chapter 6

Experimental demonstration of linear nanoshell plasmonic waveguides

6.1 Introduction

In this chapter we report on experimental demonstration of the linear nanoshell plasmonic waveguides as a step towards the nonlinear nanoshell plasmonic waveguides. The plasmon resonances in metallo-dielectric cylindrical nanorods were reported in previous works [43]. External electromagnetic (EM) radiation with electric fields perpendicular to the nanoshell cylinder axis can facilitate the excitation of the two-dimensional (2D) cross-sectional plasmon distribution and induce enhanced optical absorption [43]. However, those plasmon resonances are stationary (nonpropagating or localised) plasmon modes. Along with the stationary plasmons, propagating plasmon modes (i.e. with a nonzero wavevector) can also exist within the metallic shell surfaces with wavevectors along the cylinder axis [124, 125]. The waveguiding abilities of such propagating plasmon modes are discussed in details in Chapter 5. Here, we experimentally demonstrate the existence of the propagating plasmon modes in metallic nanoshells. The plasmon modes within elliptical metallic shells are also highly polarisation

sensitive (as discussed in section 5.2 of Chapter 5) and here we successfully characterise the polarisation sensitivity with the excitations of linearly polarised (TE and TM) light. This is an important advancement towards the realisation of the potential applications of these nanoshell plasmonic waveguides. We fabricate polymer nanorods with the direct laser writing (DLW) method and coat them with thin silver films by the electroless silver deposition method (modified Tollens method) [143]. We present some preliminary results for the experimental confirmation of the propagating plasmon modes in metallic nanoshells with the Fourier transform infrared (FTIR) microscopy characterisation. We also support our experimental findings with detailed theoretical calculations. The dispersive features of the propagating plasmons are also analysed thoroughly.

This chapter is divided into six sections. In Sections 6.2 and 6.3 we discuss the realisation of the linear nanoshell plasmonic waveguides with the combination of fabricating dielectric polymer nanorods by the DLW fabrication method and the deposition of thin silver film onto the polymer rod surface with the electroless silver deposition methods. In Section 6.4 we demonstrate the experimental confirmation of propagating plasmon modes within the linear nanoshell plasmonic waveguides. The polarisation sensitivity for exciting the propagating plasmon modes within the nanoshell plasmonic waveguide is also addressed.

In Section 6.5 we provide the theoretical insight for the mode characteristics of the linear nanoshell plasmonic waveguides and discuss their dispersive features. We also show good agreements between our experimental and theoretical results. We discuss the chapter conclusions in Section 6.6.

6.2 Fabrication of dielectric gratings with direct laser writing

Here, we fabricate 2D periodic dielectric nanorod gratings with the DLW fabrication method. DLW fabrication method has been discussed in detail in Chapter 4. The microstructures were fabricated with IP-L photoresist (Nanoscribe Gmbh) on a borosilicate glass substrate. We fabricate suspended gratings supported by two massive frames at the two ends of the polymer rods. A thinner frame was also fabricated at the middle of the polymer rods for further stabilisation. The fabricated polymer rods have a periodicity of 3.0 µm and length of 15 µm. The polymer rods experience rapid proximity effects and combine with the adjacent rods for smaller lattice periods. Although three-dimensional (3D) woodpile microstructures fabricated by DLW method have been realised with an in-layer lattice constant less than 1.0 µm, it should be noted such structures are made of a 3D connected networks of the parallel dielectric rods which provides mechanical strength to avoid the proximity effects and structural distortion. Fig. 6.1 shows the reflection and transmission optical microscope images of fabricated polymer rod gratings with DLW method.

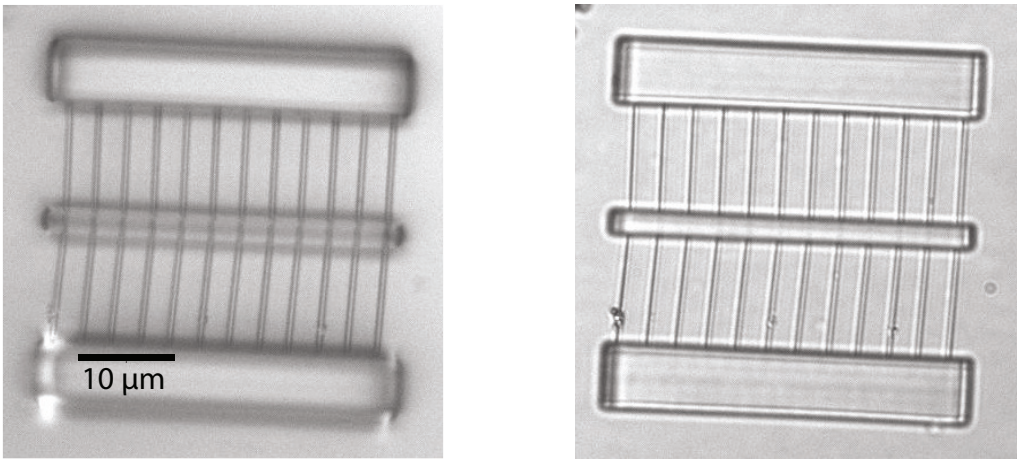

Figure 6.1 (a) Reflection optical microscope image of a fabricated polymer nanorod grating. (b) Transmission optical microscope image of the same microstructure shown in (a).

6.3 Metallic coating with electroless silver deposition

We adopt an electroless silver deposition method for thin silver layer coating on the dielectric polymer rods. This deposition method is based on the modified Tollens reaction [143]. For the electroless silver deposition, an aqueous solution of silver nitrate was prepared which comprises ammonia as the stabilisation of silver, aldehydes as the mild reduction agents and a strong base (e.g. NaOH or KOH) as the reduction reaction catalyst. The object which is to be coated with silver is immersed into the silver solution where the silver is reduced and deposited. The basic reaction for the silver reduction is as follows

$$Ag(NH_3)^{2+} + RCHO + OH^- \rightarrow Ag + RCOO^- + NH_3 + H_2O$$

where $Ag(NH_3)^{2+}$ is the diammine-silver complex formed by the reaction between the ammonia and silver nitrate and RCHO represents the aldeyde group. Glucose has been used in this work as the source of aldehyde groups. The deposition of silver in such process is in general very fast and can produce good quality thick silver films. However, fast deposition of silver might also be a problem for thin film coating. For the deposition of thin silver films on dielectric microstructures, the kinetics of the silver reduction reaction can be slowed down by adding Arabic Gum to the aqueous solution of silver nitrate. This chemical has already been used in other electroless deposition for inducing a slower reduction rate [144]. This modified Tollens method has the ability to deposit silver films with much less surface roughness and to produce films with thickness in the 30-40 nm range.

The following recipe was followed for the electroless silver deposition solution.

2.5M aqueous $Ag(NO_3)$ Solution - 8 mL

30%weight NH_4OH solution - 5 mL

32g/L NaOH solution - 3 mL

50g/L Arabic gum aqueous solution - 12 mL

45g/L Glucose aqueous solution - 4 mL

All the components were mixed in a glass beaker. Before starting the deposition process, the borosilicate glass substrate containing the dielectric microstructure fabricated by DLW was treated by O_2 plasma. The glass substrate was then immersed into the silver solution. In every 4 minutes the substrate was taken out from the solution and was rinsed with distilled water in order to remove aggregation of silver nanoparticles to assure a homogeneous and thin silver coating. This procedure was repeated for a total duration of 90 minutes. The resulting coating was rinsed with distilled water and ethanol and finally was dried in oven at 80°C. The densely packed silver nanoparticles in the electroless deposition have sizes in the range of 40 to 50 nm with a mean crystalline silver diameter of 43 nm [143]. Hence, the effective thickness of the silver film is assumed as 37 nm. The silver nanoparticles in the film were well connected, assuring high electrical conductivity. Fig. 6.2 shows the deposited silver film on our 2D polymer rods grating microstructure.

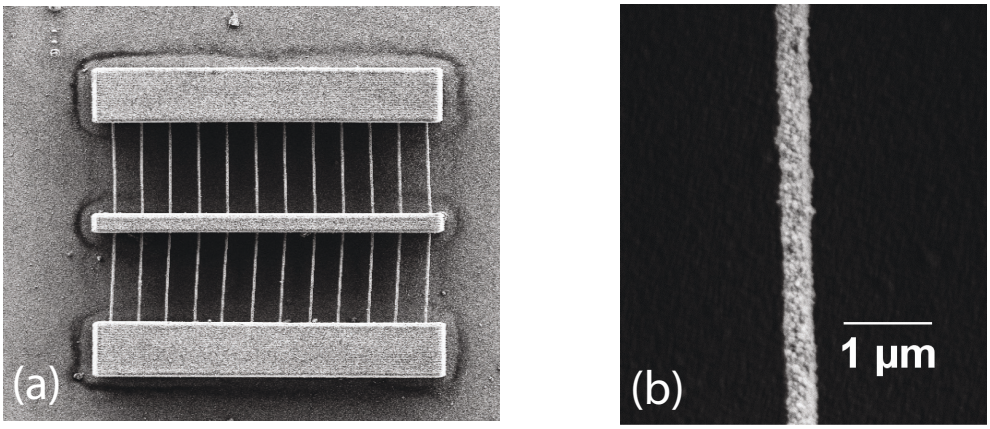

Fig. 6.2 (a) SEM image of electroless silver coated polymer rod gratings (b) Magnified view of the silver nanoparticles coated polymer rods.

6.4 Experimental characterisation of the plasmon modes within the metallic nanoshells

To characterise the optical properties of the thin silver film coated polymer nanorods grating we perform the FTIR microscopy measurement with linearly polarised lights. One problem of our electroless silver coating is its inability for selective coating. As can be seen from Fig. 6.2 the silver film was also deposited to the glass substrate beneath the polymer rod gratings. This had restricted any transmission measurement by the FTIR microscopy. However, we were able to perform reflection measurement with a finite opening angle of 18^{o} to 41^{o}.

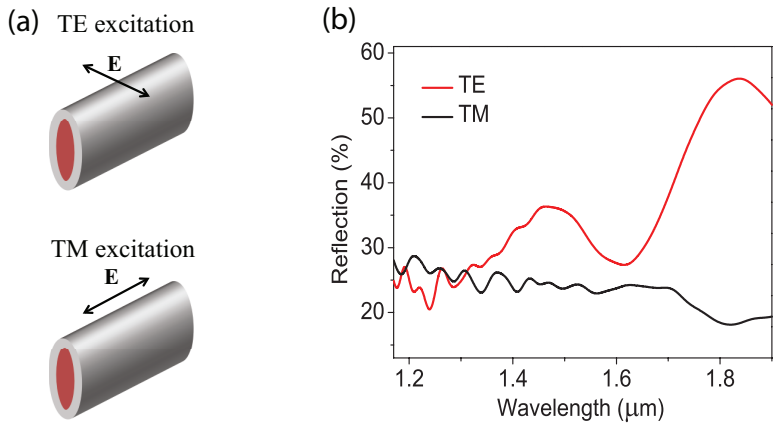

Fig. 6.3 FTIR microscopy measurements for reflection spectra with the two orthogonal linearly polarized incident beams. (a) The excitation scheme of the plasmon mode of the nanoshell plasmonic waveguide for TE (electric fields perpendicular to the nanoshell cylinder axis) excitation and TM (electric field parallel to the nanoshell cylinder axis) excitation (b) The TE measurement shows a reflection dip at λ=1.615 μm. The TM measurement does not show such a phenomenon.

Fig. 6.3 shows that the reflection spectra for the TE measurement (electric field perpendicular to the nanoshell cylinder axis) possess a reflection dip at 1.615 µm. However, for the TM measurement no such reflection dip was observed. We argue that the resonant reflection dip for the TE measurement is due to the optical absorption caused by the propagating plasmons on the surface of the silver nanoshells and support these experimental results with the theoretical calculation in the next section.

6.5 Theoretical characterisation

Here, at first, we investigate the mode characteristics of the nanoshell plasmonic waveguide with a subwavelength linear dielectric core. The refractive index of the linear dielectric core (IP-L photoresist, Nanoscribe Gmbh) was set to 1.52 and the dispersive properties of the silver metal were expressed with Drude dispersive model. We check the modal properties of the plasmon mode with the eigenmode solver (COMSOL Multiphysics).

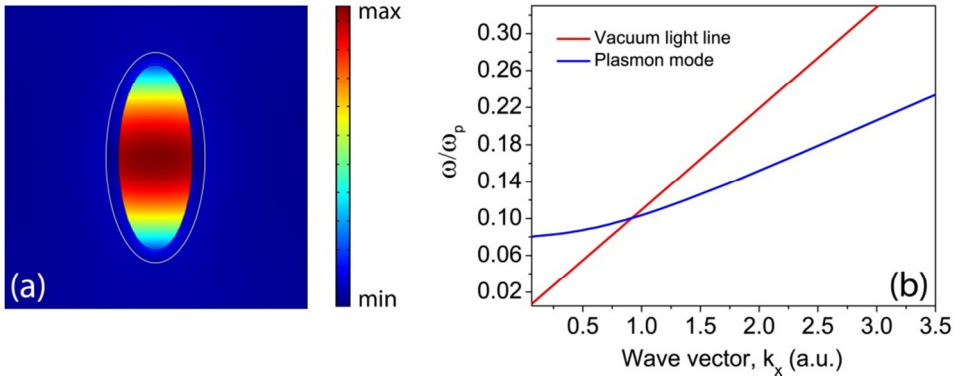

Fig. 6.4 (a) Calculated electric field distributions of the plasmon mode at λ=1.619 µm for the silver film coated dielectric nanorods with a core width of 220 nm, a core height of 550 nm and a silver nanoshell thickness of 37 nm thickness. The white line illustrates the boundary between the silver nanoshell and the air background. (b) Dispersion relation of the plasmon mode of the silver film coated nanorods for the same parameters used in (a).

Fig. 6.4 shows the plasmon mode characteristics within the nanoshell plasmonic waveguide. The effective mode index n_{eff} (k_{mode}/k_0) is 0.50. The effective mode index n_{eff}<1 states that the plasmon mode wavevector k_{mode} is lower in magnitude than the free space wavevector k_0. The fundamental characteristics of such modes can be further understood form their dispersion relations. The dispersion curves presented in Fig. 6.4(a) which shows that these plasmon modes stay on the left side of the vacuum light line stating their radiative nature. Thus these modes can be termed as leaky modes and can be excited externally. The excitation scheme is demonstrated in Fig. 6.5(a). To excite the plasmon modes, the incident wave polarisation needs to match with the plasmon mode polarisation. An incident TE mode with perpendicular incidence to the nanoshell waveguide does not contain any wavevector component along the nanoshell waveguide axis to excite the propagating plasmon modes rather it will excite the stationary mode. However, incident TE radiation with an angle to the perpendicular direction provides wavevector component k_x (where k_x<k_0) along the nanoshell waveguide axis and thus can efficiently excite the propagating plasmon modes with $k_{mode}=k_x$ as shown in Fig. 6.5(a). For an incidence with angle θ, the incident radiation will contain a wavevector component $k_x=k_0 sin\theta$. The excited plasmon modes will decay over their propagation length and will create an absorption peak of the incident radiation.

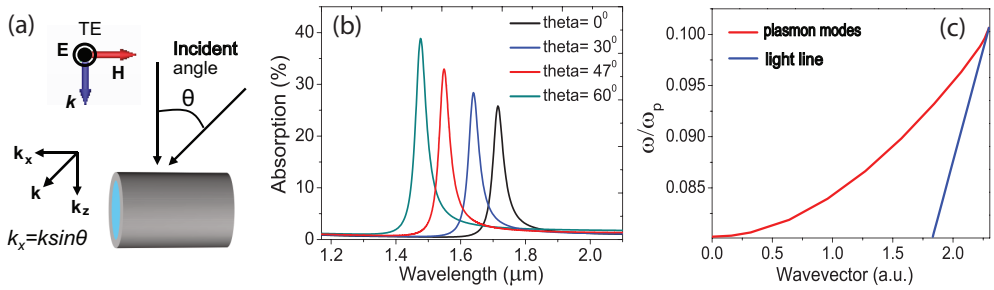

Fig. 6.5 (a) Schematic of the angle of incidence excitation of the propagating plasmon modes with the parallel component k_x of the incident wavevector k_0. (b) Absorption peaks of the incident radiation for incidences with different angles (c) The dispersion relation for the plasmon modes.

To confirm this we run transmission/reflection calculations based on finite element numerical simulations with CST MWS studio software and record any absorption peaks within the spectra. The incident wave is a linearly polarized plane wave with electric field perpendicular to nanoshell waveguide axis (TE mode, i.e. electric field is parallel to the plasmon mode field distribution) and the angle of incidence was varied over a range. The periodicity of the nanoshell waveguide grating is 1.0 μm. It has been demonstrated earlier [43] that nonlocal parameter, such as the periodicity of the nanoshells does not affect the spectral positions of the local plasmon modes. Therefore, modes here are induced purely by the local geometry of the nanoshells. It can be seen in Fig. 6.5(b) that absorption peaks arise due to the excitation of the plasmon modes by external EM radiation with oblique incidence. The amount of the absorption depends of the coupling efficiency of the incident radiation to the plasmon mode which is mainly related to the metallic nanoshell thickness of the plasmonic waveguide. Thinner metallic nanoshells cause more efficient coupling and higher absorption. For normal incidence (θ=0) only the stationary plasmon mode (k_{mode} = 0) is excited but for an incidence with an angle the wavevector component k_x matches the propagating plasmon wavevector k_{mode} and thus excites. It should be noted that as we continuously increase the incident angle θ, k_x increases and excites the high frequency plasmon modes. For an incidence angle of 30^o, the plasmon resonance occurs at the wavelength of 1.619 μm, with a plasmon mode effective index, n_{eff} of ~0.50 ($n_{eff} = k_x/k_0 = k_0 \sin 30^o/k_0$). This exactly matches the effective mode index of the plasmon mode calculated by the eigenmode solver at the wavelength of 1.619 μm as shown in Fig. 6.4 and confirms the validity of our theoretical calculations. Fig. 6.5(c) shows the dispersion relation for the propagating plasmons with the wavevector component k_x extracted from the calculated spectral positions of the absorption peaks for different incidence angles. As mentioned earlier, these plasmon modes with wavevector $k_x < k_0$ lies at the left hand side of the light line and demonstrates their radiative nature. Furthermore, to confirm the polarisation sensitivity of the plasmon modes, we also run simulations for TM

modes (the electric fields parallel to the waveguide axis) with oblique incidence. No such absorption peaks were observed. This is due to the fact that for the oblique incidence with a TM mode, although the incident wave carries a wavevector component k_x along the nanoshell waveguide axis, it does not match the polarisation of the plasmon mode and hence does not excite this mode.

Now, to compare with our experimental results, we recall from Fig. 6.3(b) that a reflection dip at 1.615 μm exists in the experimentally measured reflection spectra of the silver nanoshell coated polymer rods grating. As the measurement was carried out for an opening angle of 18^o to 41^o, we assume that the mid spectral position for the absorption peak would occur at 30^o angle of incidence. Indeed, it can be noticed from the theoretically calculated results in Fig. 6.5(b) that for a 30^o angle of incidence excitation of the propagating plasmon mode the optical absorption occurs at 1.619 μm. This is a good agreement between the experiment and the theory. The deviation of the measured spectra from the simulated results originates from the averaging effects of the measurements over the wide and finite opening angle of the FTIR measurements and the roughness of the deposited silver film due the finite size of the silver nanoparticles. Furthermore, the supporting frame (3.0 μm thick) fabricated at the middle of the grating sample and coated with silver as shown in Fig. 6.2(a) can act as a scattering source and drastically weaken the reflection signal measured by the FTIR microscope detector.

Fig. 6.6 shows the phase plot of the propagating plasmons within the linear nanoshell plasmonic waveguide for the TE mode at the incidence angle of 60^o.

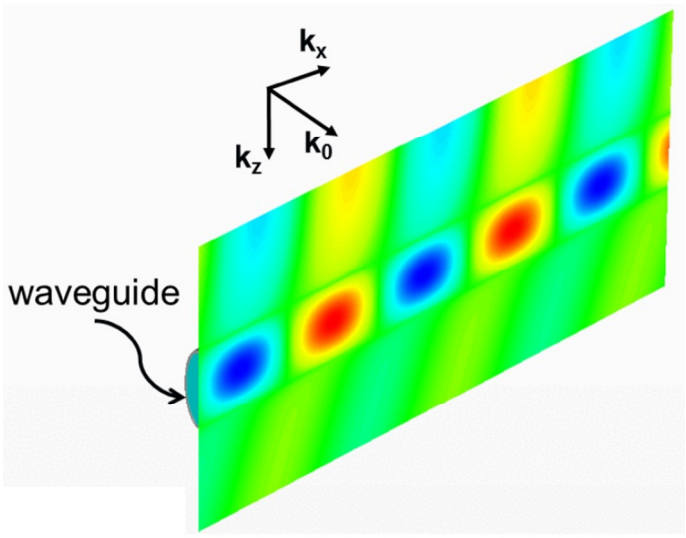

Fig. 6.6 Calculated phase plot of the electric fields of the plasmon mode depicting the propagating nature at 60^o of incidence and at the wavelength of 1.619 µm.

6.6 Chapter conclusion

In conclusion, we have experimentally demonstrated the existence of propagating plasmon modes in metallic nanoshells. The polarisation sensitivity of the plasmon modes was verified with experimental measurements. For the realisation of linear nanoshell plasmonic waveguides an electroless silver deposition was used for producing homogeneous and thin silver film coating on polymer dielectric nanorods fabricated via DLW. This metal coating is a significant step towards the realisation of the potential applications of nanoshell plasmonic waveguides.

We have also theoretically characterised the propagating plasmon modes within linear nanoshell plasmonic waveguide structures with detailed numerical simulations and good agreement was found with the experimental results. The results presented in this section are thus promising for the future nanoplasmonic devices for communications.

Chapter 7

Conclusions

7.1 Thesis conclusion

Optimisation of enhanced absorption in three-dimensional (3D) metallic photonic crystals (MPCs) and fabrication of high quality 3D MPCs is of significant importance for the realisation of tailored thermal emission, which has promising applications in thermo-photovoltaics. This thesis has presented a detailed and comprehensive theoretical study for the optimisation of enhanced absorption in 3D woodpile MPCs and experimental studies for the realisation of inversed woodpile 3D MPCs.

The major theoretical achievements for the optimisation of resonant absorption in 3D MPCs are:

1. The resonant dissipative behaviour within the 3D woodpiles MPCs was investigated with respect to the dispersive properties for geometrical alterations of the MPC structures. Dispersive features were analysed with band structure diagrams and the effect of induced low group velocities on absorption enhancement was investigated.

2. The optimisation of the resonant absorption within 3D woodpile MPCs was demonstrated through the modifications of MPC structural parameters. Great flexibility was observed to optimise the absorption band width, magnitude and spectral position with only a slight amount of structural modifications.

3. The resonant absorption within 3D MPCs was also analysed for different bulk materials. The effect of the distinct dispersive properties of different metals for optimising the spectral properties of the MPC structures was thoroughly discussed through numerical simulations. Resonant absorption with extreme narrow absorption band width as small as ~13 nm was reported for MPCs with finite number of layers.

The optimisation approach for enhanced absorption in 3D woodpile MPCs presented in this thesis can be of significant importance for achieving efficient modified thermal emission.

A novel experimental method was used for realising high quality 3D MPC microstructures via the state-of-the-art microfabrication facilities. Successful results were obtained in achieving 3D inversed woodpile nickel MPCs. The primary achievements of the experimental works are as follows.

1. DLW method was employed to fabricate high quality dielectric PC templates in photosensitive polymer resins. Multiline laser scanning method was also used for realising 3D polymer PC templates with appropriate filling ratios. The fabrication was successfully performed on conductive indium-tin-oxide (ITO) glass substrates.

2. Electrodeposition method was used as the unique means for infiltrating metals into the polymer PC microstructure templates fabricated by DLW. Commercially available, cheap electrodeposition materials were used to successfully deposit nickel metal into the PC templates. Electrodeposition

allowed good control over the growth rate of metal film on the conductive glass substrates through regulating the concentration of the electrolyte solution and current density. The deposition of the nickel film with desired thickness was possible to achieve.

3. High quality inversed woodpile nickel MPC structures operating in the optical wavelength regime were realised.

4. The optical properties of the inversed woodpile MPCs were characterised experimentally and good agreements were found with theoretically predicted results. This demonstrates the ability of the fabricating method for realising good quality MPCs.

5. Multiple enhanced optical absorption peaks over wide spectral range were observed within the fabricated nickel MPCs which offers promising applications in tailored thermal emissions.

6. Novel features of optical absorptions with robust plasmon resonances were also observed within the fabricated inversed woodpile nickel MPCs which has potential applications in plasmonic solar cells.

On the other hand, plasmonics waveguides offer the opportunity for revolutionising the next generation optical communication and information processing systems. The novel class of nonlinear nanoshell subwavelength plasmonic waveguide presented in this thesis provides significant advance in terms of total mode energy confinement and ultrahigh Kerr nonlinearity over the current subwavelength waveguide designs. The primary achievements of the nanoshell plasmonic waveguide from the theoretical investigations presented in this thesis are as follows:

1. A subwavelength confinement with mode area as small as 0.0196 μm^2 was demonstrated.

2. Total energy confinement (~100%) was predicted which is the first time theoretical demonstration within subwavelength optical waveguides. This unique property of the nanoshell plasmonic waveguide allows for achieving zero-cross talk nanophotonic elements for the true realisation of integrated nanophotonic chips.

3. Nonlinear properties within the subwavelength nanoshell plasmonic waveguide were thoroughly investigated and significant enhancement of the effective nonlinear index coefficient was observed due to the vectorial mode profiles of the plasmon mode. Further enhancement of the nonlinear properties was even observed for the geometrical alterations of the plasmonic waveguide. The rapid enhancement of the effective nonlinear index coefficient in combination with the small effective mode area yielded an ultrahigh Kerr nonlinearity up to $4.1\times10^{4}W^{-1}m^{-1}$.

4. The origin of the ultrahigh nonlinearity was explained in terms of the redistribution of the modal fields with the geometrical alterations. Further discussion on the ultrahigh nonlinearity of the plasmonic waveguide was provided in terms of their dispersive properties. Rapid enhancement of the nonlinearity was accurately predicted in terms of the reduction of the group velocity.

The outstanding property of the nonlinear subwavelength nanoshell plasmonic waveguide is its ability to possess total energy confinement with ultrahigh Kerr nonlinearity in a single platform. This has made it an outstanding candidate as a basic nanophotonic element for the realisation of future integrated nanophotonic chips.

An experimental demonstration of nanoshell plasmonic waveguides was also presented in this thesis. The linear nanoshell plasmonic waveguide was realised with the combination of the DLW method for fabricating dielectric nanorods and the electroless silver deposition for coating the dielectric nanorods with thin and

homogeneous silver film. The existence of the propagating plasmon modes within the nanoshell plasmonic waveguides were confirmed with the excitation of linearly polarised lights.

In summary, the research work presented in this thesis contains innovative and detailed studies on 3D MPCs for nanophotonic applications. The optimisation of the resonant absorption in 3D woodpile MPCs has been discussed and the realisation of 3D inversed woodpile nickel MPCs operating in the optical wavelengths has been demonstrated. Novel subwavelength nanoshell plasmonic waveguide design has been proposed with total energy confinement and ultrahigh Kerr nonlinearity. The existence of propagating plasmons has also been experimentally realised in nanoshell plasmonic waveguides. These exclusive results could play an effective role in the advancement of the future efficient thermo-photovoltaic systems, high speed communications and information processing.

7.2 Future outlook

The experimental method for achieving 3D MPCs can be further extended to realise microstructures with different metals. Nickel is lossy in the near infrared (NIR) to visible wavelengths regime. However, electrodeposition is also a potential chemical method for deposition of noble metals (such as gold). The ability of the DLW method for the fabrication of dielectric PC templates in small feature sizes and the infiltration of gold into 3D dielectric polymer templates could result in inversed MPCs operating in the near infrared (NIR) to visible wavelengths region. Moreover, gold MPCs can also support plasmon resonances in such wavelengths regime which could lead to very interesting and useful optical properties. In this presented thesis the 3D polymer template was left unremoved after the metal deposition for the realisation of the inversed woodpile MPC. Removal of the polymer template by possible chemical or thermal

treatment would allow the investigation of pure metallic microstructures. Furthermore, inclusion of nonlinear materials into the metallic template could lead to novel optical properties.

The experimental demonstration of plasmon modes into metallic nanoshells in the presented thesis does not contain any nonlinear characterisation. Future investigations would have the opportunity to characterise robust nonlinear optical properties with introducing highly nonlinear materials into the nanoshell plasmonic waveguide core. Indeed, highly nonlinear chalcogenide glasses are ideal candidates for the realisation of ultrahigh nonlinear plasmonic waveguides due to the unique feature of realising chalcogenide nanowires with DLW fabrication method. In addition, further optimisation can be done to improve the electroless silver coating for improved optical properties. Other metal deposition methods such as chemical vapour deposition (CVD) and atomic layer deposition (ALD) can also be implemented to improve the quality of the metal film on the dielectric surface. Introduction of gain materials (such as quantum dots) into the nonlinear nanoshell plasmonic waveguide would definitely open a new window for the extensive research on the realisation for plasmonic nanolasers, switches and modulators.

Bibliography

1. E. Yablonovitch, "Inhibited spontaneous emission in solid-state physics and electronics," Physical Review Letters **58**, 2059-2062 (1987).

2. S. John, "Strong localization of photons in certain disordered dielectric superlattices," Physical Review Letters **58**, 2486-2489 (1987).

3. H. Raether, "Surface plasmons on Smooth and Rough Surfaces and on Gratings," (Springer, Berlin, 1988).

4. E. Ozbay, "Plasmonics: Merging photonics and electronics at nanoscale dimensions," Science **311**, 189-193 (2006).

5. M. Schnell, P. Alonso-González, L. Arzubiaga, F. Casanova, L. E. Hueso, A. Chuvilin, and R. Hillenbrand, "Nanofocusing of mid-infrared energy with tapered transmission lines," Nature Photonics **5**, 283-287 (2011).

6. H. A. Atwater, and A. Polman, "Plasmonics for improved photovoltaic devices," Nature Materials **9**, 205-213 (2010).

7. H. Kosaka, T. Kawashima, A. Tomita, M. Notomi, T. Tamamura, T. Sato, and S. Kawakami, "Superprism phenomena in photonic crystals," Physical Review B - Condensed Matter and Materials Physics **58**, R10096-R10099 (1998).

8. J. Serbin, and M. Gu, "Experimental evidence for superprism effects in three-dimensional polymer photonic crystals," Advanced Materials **18**, 221-224 (2006).

9. P. Tran, "Optical switching with a nonlinear photonic crystal: A numerical study," Optics Letters **21**, 1138-1140 (1996).

10. S. John, and M. Florescu, "Photonic bandgap materials: Towards an all-optical micro-transistor," Journal of Optics A: Pure and Applied Optics **3**, S103-S120 (2001).

11. S. Y. Lin, E. Chow, J. Bur, S. G. Johnson, and J. D. Joannopoulos, "Low-loss, wide-angle Y splitter at ~1.6 μm wavelengths built with a two-dimensional photonic crystal," Optics Letters **27**, 1400-1402 (2002).

12. S. Boscolo, M. Midrio, and T. F. Krauss, "Y junctions in photonic crystal channel waveguides: High transmission and impedance matching," Optics Letters **27**, 1001-1003 (2002).

13. J. D. Joannopoulos, S. G. Johnson, R. D. Meade, and J. N. Winn, "Photonic crystals, Molding the flow of light, 2nd ed," (Princeton University Press, Princeton, 2008).

14. K. M. Ho, C. T. Chan, and C. M. Soukoulis, "Existence of a photonic gap in periodic dielectric structures," Physical Review Letters **65**, 3152-3155 (1990).

15. Z. Zhang, and S. Satpathy, "Electromagnetic wave propagation in periodic structures: Bloch wave solution of Maxwells equations," Physical Review Letters **65**, 2650-2653 (1990).

16. K. Sakoda, "Optical Properties of Photonic Crystals," (Springer, Berlin, 2005).

17. J. M. Bendickson, J. P. Dowling, and M. Scalora, "Analytic expressions for the electromagnetic mode density infinite, one-dimensional, photonic band-gap structures," Physical Review E - Statistical Physics, Plasmas, Fluids, and Related Interdisciplinary Topics **53**, 4107-4121 (1996).

18. S. Y. Lin, J. G. Fleming, E. Chow, J. Bur, K. K. Choi, and A. Goldberg, "Enhancement and suppression of thermal emission by a three-dimensional photonic crystal," Physical Review B - Condensed Matter and Materials Physics **62**, R2243-R2246 (2000).

19. C. Kittel, "Introduction to Solid State Physics, 5th ed," (John Wiley and Sons Inc., New York, 1976).

20. J. R. Reitz, F. J. Milford, and R. W. Christy, "Foundations of Electromagnetic Theory," (Pearson education, Inc, Massachusets, 1993).

21. D. J. Griffiths, "Introduction to Electrodynamics, 3rd ed," (Pearson Education, Inc, Massachusets, 1993).

22. S. Y. Lin, J. Moreno, and J. G. Fleming, "Three-dimensional photonic-crystal emitter for thermal photovoltaic power generation," Applied Physics Letters **83**, 380-382 (2003).

23. S. Y. Lin, J. G. Fleming, and I. El-Kady, "Three-dimensional photonic-crystal emission through thermal excitation," Optics Letters **28**, 1909-1911 (2003).

24. P. Nagpal, S. E. Han, A. Stein, and D. J. Norris, "Efficient low-temperature thermophotovoltaic emitters from metallic photonic crystals," Nano Letters **8**, 3238-3243 (2008).

25. J. G. Fleming, S. Y. Lin, I. El-Kady, R. Biswas, and K. M. Ho, "All-metallic three-dimensional photonic crystals with a large infrared bandgap," Nature **417**, 52-55 (2002).

26. J. H. Lee, Y. S. Kim, K. Constant, and K. M. Ho, "Woodpile metallic photonic crystals fabricated by using soft lithography for tailored thermal emission," Advanced Materials **19**, 791-794 (2007).

27. S. Y. Lin, J. G. Fleming, and I. El-Kady, "Highly efficient light emission at λ = 1.5 μm by a three-dimensional tungsten photonic crystal," Optics Letters **28**, 1683-1685 (2003).

28. S. John, and R. Wang, "Metallic photonic-band-gap filament architectures for optimized incandescent lighting," Physical Review A - Atomic, Molecular, and Optical Physics **78**, 043809 (2008).

29. Y.-S. Kim, and S.-Y. Lin, "Analysis of photon recycling using metallic photonic crystal," Journal of Applied Physics **102**, 063107 (2007).

30. I. El-Kady, M. M. Sigalas, R. Biswas, K. M. Ho, and C. M. Soukoulis, "Metallic photonic crystals at optical wavelengths," Physical Review B - Condensed Matter and Materials Physics **62**, 15299-15302 (2000).

31. D. Bohm, and D. Pines, "A collective description of electron interactions. I. magnetic interactions," Physical Review **82**, 625-634 (1951).

32. D. Pines, and D. Bohm, "A collective description of electron interactions: II. Collective vs individual particle aspects of the interactions," Physical Review **85**, 338-353 (1952).

33. R. H. Ritchie, "Plasma Losses by Fast Electrons in Thin Films," Physical Review **106**, 874-881 (1957).

34. J. R. Sambles, G. W. Bradbery, and F. Yang, "Optical excitation of surface plasmons: an introduction," Contemporary Physics **32**, 173-183 (1991).

35. W. L. Barnes, A. Dereux, and T. W. Ebbesen, "Surface plasmon subwavelength optics," Nature **424**, 824-830 (2003).

36. E. Kretschmann, and H. Raether, "Radiative decay of non-radiative surface plasmons excited by light," Z. Naturforsch. Teil A **23**, 2135-2136 (1968).

37. A. Otto, "Excitation of nonradiative surface plasma waves in silver by the method of frustrated total reflection.," Z. Phys **216** (1968).

38. B. Hecht, H. Bielefeldt, L. Novotny, Y. Inouye, and D. W. Pohl, "Local excitation, scattering, and interference of surface plasmons," Physical Review Letters **77**, 1889-1892 (1996).

39. H. Ditlbacher, J. R. Krenn, N. Felidj, B. Lamprecht, G. Schider, M. Salerno, A. Leitner, and F. R. Aussenegg, "Fluorescence imaging of surface plasmon fields," Applied Physics Letters **80**, 404-406 (2002).

40. R. H. Ritchie, E. T. Arakawa, J. J. Cowan, and R. N. Hamm, "Surface-plasmon resonance effect in grating diffraction," Physical Review Letters **21**, 1530-1533 (1968).

41. S. Coyle, M. C. Netti, J. J. Baumberg, M. A. Ghanem, P. R. Birkin, P. N. Bartlett, and D. M. Whittaker, "Confined plasmons in metallic nanocavities," Physical Review Letters **87**, 1768011-1768014 (2001).

42. E. Prodan, "A Hybridization Model for the Plasmon Response of Complex Nanostructures," Science **302**, 419-422 (2003).

43. J. Li, M. M. Hossain, B. Jia, D. Buso, and M. Gu, "Three-dimensional hybrid photonic crystals merged with localized plasmon resonances," Optics Express **18**, 4491-4498 (2010).

44. C. Radloff, and N. J. Halas, "Plasmonic Properties of Concentric Nanoshells," Nano Letters **4**, 1323-1327 (2004).

45. T. W. Ebbesen, C. Genet, and S. I. Bozhevolnyi, "Surface-plasmon circuitry," Physics Today **61**, 44-50 (2008).

46. T. Nikolajsen, K. Leosson, and S. I. Bozhevolnyi, "Surface plasmon polariton based modulators and switches operating at telecom wavelengths," Applied Physics Letters **85**, 5833-5835 (2004).

47. J. A. Schuller, E. S. Barnard, W. Cai, Y. C. Jun, J. S. White, and M. L. Brongersma, "Plasmonics for extreme light concentration and manipulation," Nature Materials **9**, 193-204 (2010).

48. V. E. Ferry, L. A. Sweatlock, D. Pacifici, and H. A. Atwater, "Plasmonic nanostructure design for efficient light coupling into solar cells," Nano Letters **8**, 4391-4397 (2008).

49. D. F. P. Pile, T. Ogawa, D. K. Gramotnev, T. Okamoto, M. Haraguchi, M. Fukui, and S. Matsuo, "Theoretical and experimental investigation of strongly localized plasmons on triangular metal wedges for subwavelength waveguiding," Applied Physics Letters **87**, 061106 (2005).

50. E. Moreno, S. G. Rodrigo, S. I. Bozhevolnyi, L. Martín-Moreno, and F. J. García-Vidal, "Guiding and focusing of electromagnetic fields with wedge plasmon polaritons," Physical Review Letters **100**, 023901 (2008).

51. S. I. Bozhevolnyi, V. S. Volkov, E. Devaux, J. Y. Laluet, and T. W. Ebbesen, "Channel plasmon subwavelength waveguide components including interferometers and ring resonators," Nature **440**, 508-511 (2006).

52. C. Min, and G. Veronis, "Absorption switches in metal-dielectric-metal plasmonic waveguides," Optics Express **17**, 10757-10766 (2009).

53. J. A. Dionne, K. Diest, L. A. Sweatlock, and H. A. Atwater, "PlasMOStor: A metal-oxide-si field effect plasmonic modulator," Nano Letters **9**, 897-902 (2009).

54. W. Cai, J. S. White, and M. L. Brongersma, "Compact, high-speed and power-efficient electrooptic plasmonic modulators," Nano Letters **9**, 4403-4411 (2009).

55. C. Delacour, S. Blaize, P. Grosse, J. M. Fedeli, A. Bruyant, R. Salas-Montiel, G. Lerondel, and A. Chelnokov, "Efficient directional coupling between silicon and copper plasmonic nanoslot waveguides: Toward metal-oxide-silicon nanophotonics," Nano Letters **10**, 2922-2926 (2010).

56. R. F. Oulton, V. J. Sorger, T. Zentgraf, R. M. Ma, C. Gladden, L. Dai, G. Bartal, and X. Zhang, "Plasmon lasers at deep subwavelength scale," Nature **461**, 629-632 (2009).

57. M. T. Hill, Y. S. Oei, B. Smalbrugge, Y. Zhu, T. De Vries, P. J. Van Veldhoven, F. W. M. Van Otten, T. J. Eijkemans, J. P. Turkiewicz, H. De Waardt, E. J. Geluk, S. H. Kwon, Y. H. Lee, R. Nötzel, and M. K. Smit, "Lasing in metallic-coated nanocavities," Nature Photonics **1**, 589-594 (2007).

58. M. I. Stockman, "Nanofocusing of optical energy in tapered plasmonic waveguides," Physical Review Letters **93**, 137401-137404 (2004).

59. A. J. Babadjanyan, N. L. Margaryan, and K. V. Nerkararyan, "Superfocusing of surface polaritons in the conical structure," Journal of Applied Physics **87**, 3785-3788 (2000).

60. D. K. Gramotnev, M. W. Vogel, and M. I. Stockman, "Optimized nonadiabatic nanofocusing of plasmons by tapered metal rods," Journal of Applied Physics **104**, 034311 (2008).

61. M. Durach, A. Rusina, M. I. Stockman, and K. Nelson, "Toward full spatiotemporal control on the nanoscale," Nano Letters **7**, 3145-3149 (2007).

62. K. C. Vernon, D. K. Gramotnev, and D. F. P. Pile, "Adiabatic nanofocusing of plasmons by a sharp metal wedge on a dielectric substrate," Journal of Applied Physics **101**, 104312 (2007).

63. H. Choi, D. F. P. Pile, S. Nam, G. Bartal, and X. Zhang, "Compressing surface plasmons for nano-scale optical focusing," Optics Express **17**, 7519-7524 (2009).

64. D. F. P. Pile, and D. K. Gramotnev, "Adiabatic and nonadiabatic nanofocusing of plasmons by tapered gap plasmon waveguides," Applied Physics Letters **89**, 041111 (2006).

65. P. Ginzburg, D. Arbel, and M. Orenstein, "Gap plasmon polariton structure for very efficient microscale-to-nanoscale interfacing," Optics Letters **31**, 3288-3290 (2006).

66. A. V. Krasavin, and N. I. Zheludev, "Active plasmonics: Controlling signals in Au/Ga waveguide using nanoscale structural transformations," Applied Physics Letters **84**, 1416-1418 (2004).

67. D. Pacifici, H. J. Lezec, and H. A. Atwater, "All-optical modulation by plasmonic excitation of CdSe quantum dots," Nature Photonics **1**, 402-406 (2007).

68. K. F. MacDonald, Z. L. Sámson, M. I. Stockman, and N. I. Zheludev, "Ultrafast active plasmonics," Nature Photonics **3**, 55-58 (2009).

69. A. Vial, A. S. Grimault, D. Macías, D. Barchiesi, and M. Lamy De La Chapelle, "Improved analytical fit of gold dispersion: Application to the modeling of extinction spectra with a finite-difference time-domain

method," Physical Review B - Condensed Matter and Materials Physics **71**, 085411-085417 (2005).

70. J. P. Dowling, M. Scalora, M. J. Bloemer, and C. M. Bowden, "The photonic band edge laser: A new approach to gain enhancement," Journal of Applied Physics **75**, 1896-1899 (1994).

71. N. A. R. Bhat, "Optical pulse propagation in nonlinear photonic crystals," Physical review. E, Statistical, nonlinear, and soft matter physics **64**, 056601-056616 (2001).

72. S. Y. Lin, J. G. Fleming, Z. Y. Li, I. El-Kady, R. Biswas, and K. M. Ho, "Origin of absorption enhancement in a tungsten, three-dimensional photonic crystal," Journal of the Optical Society of America B: Optical Physics **20**, 1538-1541 (2003).

73. C. Kittel, and H. Kroemer, "Thermal Physics " (W. H. Freeman and Company, San Francisco, 1980).

74. S. Y. Lin, J. G. Fleming, and I. El-Kady, "Experimental observation of photonic-crystal emission near a photonic band edge," Applied Physics Letters **83**, 593-595 (2003).

75. G. Veronis, R. W. Dutton, and F. Shanhui, "Metallic photonic crystals with strong broadband absorption at optical frequencies over wide angular range," Journal of Applied Physics **97**, (2005).

76. H. Y. Sang, Z. Y. Li, and B. Y. Gu, "Engineering the structure-induced enhanced absorption in three-dimensional metallic photonic crystals," Physical Review E - Statistical, Nonlinear, and Soft Matter Physics **70**, 066611-066616 (2004).

77. K. Cheng-Yu, and L. Shih-Yuan, "Opaline metallic photonic crystals possessing complete photonic band gaps in optical regime," Applied Physics Letters **92**, 121919 (2008).

78. S. Y. Lin, D. X. Ye, T. M. Lu, J. Bur, Y. S. Kim, and K. M. Ho, "Achieving a photonic band edge near visible wavelengths by metallic coatings," Journal of Applied Physics **99**, 083104 (2006).

79. A. Tal, Y. S. Chen, H. E. Williams, R. C. Rumpf, and S. M. Kuebler, "Fabrication and characterization of three-dimensional copper metallodielectric photonic crystals," Optics Express **15**, 18283-18293 (2007).

80. M. S. Rill, C. Plet, M. Thiel, I. Staude, G. Von Freymann, S. Linden, and M. Wegener, "Photonic metamaterials by direct laser writing and silver chemical vapour deposition," Nature Materials **7**, 543-546 (2008).

81. J. K. Gansel, M. Thiel, M. S. Rill, M. Decker, K. Bade, V. Saile, G. Von Freymann, S. Linden, and M. Wegener, "Gold helix photonic metamaterial as broadband circular polarizer," Science **325**, 1513-1515 (2009).

82. J. Q. Lu, and A. A. Maradudin, "Channel plasmons," Physical Review B **42**, 11159-11165 (1990).

83. I. V. Novikov, and A. A. Maradudin, "Channel polaritons," Physical Review B - Condensed Matter and Materials Physics **66**, 354031-3540313 (2002).

84. D. F. P. Pile, and D. K. Gramotnev, "Channel plasmon-polariton in a triangular groove on a metal surface," Optics Letters **29**, 1069-1071 (2004).

85. D. K. Gramotnev, and D. F. P. Pile, "Single-mode subwavelength waveguide with channel plasmon-polaritons in triangular grooves on a metal surface," Applied Physics Letters **85**, 6323-6325 (2004).

86. E. Moreno, F. J. Garcia-Vidal, S. G. Rodrigo, L. Martin-Moreno, and S. I. Bozhevolnyi, "Channel plasmon-polaritons: Modal shape, dispersion, and losses," Optics Letters **31**, 3447-3449 (2006).

87. G. Veronis, and S. Fan, "Guided subwavelength plasmonic mode supported by a slot in a thin metal film," Optics Letters **30**, 3359-3361 (2005).

88. R. F. Oulton, V. J. Sorger, D. A. Genov, D. F. P. Pile, and X. Zhang, "A hybrid plasmonic waveguide for subwavelength confinement and long-range propagation," Nature Photonics **2**, 496-500 (2008).

89. A. Moroz, "Three-Dimensional Complete Photonic-Band-gap Structures in the Visible," Physical Review Letters **83**, 5274-5277 (1999).

90. T. A. Walsh, J. A. Bur, Y. S. Kim, T. M. Lu, and S. Y. Lin, "High-temperature metal coating for modification of photonic band edge position," Journal of the Optical Society of America B: Optical Physics **26**, 1450-1455 (2009).

91. V. Mizeikis, S. Juodkazis, R. Tarozaite, J. Juodkazyte, K. Juodkazis, and H. Misawa, "Fabrication and properties of metalo-dielectric photonic crystal structures for infrared spectral region," Optics Express **15**, 8454-8464 (2007).

92. Z. Y. Li, I. El-Kady, K. M. Ho, S. Y. Lin, and J. G. Fleming, "Photonic band gap effect in layer-by-layer metallic photonic crystals," Journal of Applied Physics **93**, 38-42 (2003).

93. G. Von Freymann, S. John, M. Schulz-Dobrick, E. Vekris, N. Tétreault, S. Wong, V. Kitaev, and G. A. Ozin, "Tungsten inverse opals: The influence of absorption on the photonic band structure in the visible spectral region," Applied Physics Letters **84**, 224-226 (2004).

94. D. Sullivan, "Electromagnetic simulation using the FDTD method," (IEEE press, New York, 2000).

95. A. Taflove, and S. Hagness, "Computational Electrodynamics: The Finite-Difference Time-Domain Method, 3rd edn," (Norwood, Artech House, 2005).

96. M. M. Hossain, G. Chen, B. Jia, X. H. Wang, and M. Gu, "Optimization of enhanced absorption in 3D-woodpile metallic photonic crystals," Optics Express **18**, 9048-9054 (2010).

97. S. E. Han, A. Stein, and D. J. Norris, "Tailoring self-assembled metallic photonic crystals for modified thermal emission," Physical Review Letters **99**, 053906 (2007).

98. A. A. Kroklin, and P. Halevi, "Influence of weak dissipation on the photonic band structure of periodic composites," Physical Review B - Condensed Matter and Materials Physics **53**, 1205-1214 (1996).

99. J. H. Lee, J. C. W. Lee, W. Leung, M. Li, K. Constant, C. T. Chan, and K. M. Ho, "Polarization engineering of thermal radiation using metallic photonic crystals," Advanced Materials **20**, 3244-3247 (2008).

100. M. Chen, S. Y. Lin, H. C. Chang, and A. S. P. Chang, "Physical origin of the resonant mode deep inside the stop band of a metallodielectric photonic crystal," Physical Review B - Condensed Matter and Materials Physics **78**, 085110 (2008).

101. M. Straub, and M. Gu, "Near-infrared photonic crystals with higher-order bandgaps generated by two-photon photopolymerization," Optics Letters **27**, 1824-1826 (2002).

102. M. Deubel, G. Von Freymann, M. Wegener, S. Pereira, K. Busch, and C. M. Soukoulis, "Direct laser writing of three-dimensional photonic-crystal templates for telecommunications," Nature Materials **3**, 444-447 (2004).

103. F. Hallermann, C. Rockstuhl, S. Fahr, G. Seifert, S. Wackerow, H. Graener, G. V Plessen, and F. Lederer, "On the use of localized plasmon polaritons in solar cells," Physica Status Solidi (A) Applications and Materials **205**, 2844-2861 (2008).

104. D. Duche, P. Torchio, L. Escoubas, F. Monestier, J. J. Simon, F. Flory, and G. Mathian, "Improving light absorption in organic solar cells by plasmonic contribution," Solar Energy Materials and Solar Cells **93**, 1377-1382 (2009).

105. T. V. Teperik, F. J. García De Abajo, A. G. Borisov, M. Abdelsalam, P. N. Bartlett, Y. Sugawara, and J. J. Baumberg, "Omnidirectional absorption in nanostructured metal surfaces," Nature Photonics **2**, 299-301 (2008).

106. H. B. Sun, S. Matsuo, and H. Misawa, "Three-dimensional photonic crystal structures achieved with two-photon-absorption photopolymerization of resin," Applied Physics Letters **74**, 786-788 (1999).

107. S. Maruo, O. Nakamura, and S. Kawata, "Three-dimensional microfabrication with two-photon-absorbed photopolymerization," Optics Letters **22**, 132-134 (1997).

108. S. Wu, J. Serbin, and M. Gu, "Two-photon polymerisation for three-dimensional micro-fabrication," Journal of Photochemistry and Photobiology A: Chemistry **181**, 1-11 (2006).

109. M. Thiel, M. Decker, M. Deubel, M. Wegener, S. Linden, and G. Von Freymann, "Polarization stop bands in chiral polymeric three-dimensional photonic crystals," Advanced Materials **19**, 207-210 (2007).

110. M. D. Turner, G. E. Schrõder-Turk, and M. Gu, "Fabrication and characterization of three-dimensional biomimetic chiral composites," Optics Express **19**, 10001-10008 (2011).

111. E. Nicoletti, D. Bulla, B. Luther-Davies, and M. Gu, "Generation of λ/12 Nanowires in chalcogenide glasses," Nano Letters **11**, 4218–4221 (2011).

112. I. Staude, M. Thiel, S. Essig, C. Wolff, K. Busch, G. Von Freymann, and M. Wegener, "Fabrication and characterization of silicon woodpile photonic crystals with a complete bandgap at telecom wavelengths," Optics Letters **35**, 1094-1096 (2010).

113. G. Von Freymann, A. Ledermann, M. Thiel, I. Staude, S. Essig, K. Busch, and M. Wegener, "Three-dimensional nanostructures for photonics," Advanced Functional Materials **20**, 1038-1052 (2010).

114. K. M. Ho, C. T. Chan, C. M. Soukoulis, R. Biswas, and M. Sigalas, "Photonic band gaps in three dimensions: New layer-by-layer periodic structures," Solid State Communications **89**, 413-416 (1994).

115. H. S. Sözüer, and J. P. Dowling, "Photonic band calculations for woodpile structures," J. Mod. Opt. **41**, 231-239 (1994).

116. J. Li, B. Jia, and M. Gu, "Engineering stop gaps of inorganic-organic polymeric 3D woodpile photonic crystals with post-thermal treatment," Optics Express **16**, 20073-20080 (2008).

117. E. Nicoletti, D. Bulla, B. Luther-Davies, and M. Gu, "Planar defects in three-dimensional chalcogenide glass photonic crystals," Optics Letters **36**, 2248-2250 (2011).

118. M. C. Netti, S. Coyle, J. J. Baumberg, M. A. Ghanem, P. R. Birkin, P. N. Bartlett, and D. M. Whittaker, "Confined surface plasmons in gold photonic nanocavities," Advanced Materials **13**, 1368-1370 (2001).

119. Y. Q. Ye, Y. Jin, and S. He, "Omnidirectional, polarization-insensitive and broadband thin absorber in the terahertz regime," Journal of the Optical Society of America B: Optical Physics **27**, 498-504 (2010).

120. E. D. Palik, "Handbook of optical constants of solids," (Academic press, San Diego, 1998).

121. S. I. Bozhevolnyi, V. S. Volkov, E. Devaux, and T. W. Ebbesen, "Channel plasmon-polariton guiding by subwavelength metal grooves," Physical Review Letters **95**, 1-4 (2005).

122. B. Steinberger, A. Hohenau, H. Ditlbacher, A. L. Stepanov, A. Drezet, F. R. Aussenegg, A. Leitner, and J. R. Krenn, "Dielectric stripes on gold as surface plasmon waveguides," Applied Physics Letters **88** (2006).

123. E. Prodan, and P. Nordlander, "Plasmon hybridization in spherical nanoparticles," The Journal of Chemical Physics **120**, 5444 (2004).

124. A. Moradi, "Plasmon hybridization in metallic nanotubes," Journal of Physics and Chemistry of Solids **69**, 2936-2938 (2008).

125. M. D. Turner, M. M. Hossain, and M. Gu, "The effects of retardation on plasmon hybridization within metallic nanostructures," New Journal of Physics **12**, 083062 (2010).

126. C. Koos, P. Vorreau, T. Vallaitis, P. Dumon, W. Bogaerts, R. Baets, B. Esembeson, I. Biaggio, T. Michinobu, F. Diederich, W. Freude, and J. Leuthold, "All-optical high-speed signal processing with silicon-organic hybrid slot waveguides," Nature Photonics **3**, 216-219 (2009).

127. M. M. Hossain, M. D. Turner, and M. Gu, "Ultrahigh nonlinear nanoshell plasmonic waveguide with total energy confinement," Optics Express **19**, 23800-23808 (2011).

128. Y. Pu, R. Grange, C. L. Hsieh, and D. Psaltis, "Nonlinear optical properties of core-shell nanocavities for enhanced second-harmonic generation," Physical Review Letters **104** (2010).

129. C. Koos, L. Jacome, C. Poulton, J. Leuthold, and W. Freude, "Nonlinear silicon-on-insulator waveguides for all-optical signal processing," Optics Express **15**, 5976-5990 (2007).

130. M. A. Foster, A. C. Turner, M. Lipson, and A. L. Gaeta, "Nonlinear optics in photonic nanowires," Optics Express **16**, 1300-1320 (2008).

131. H. Yamada, M. Shirane, T. Chu, H. Yokoyama, S. Ishlda, and Y. Arakawa, "Nonlinear-optic silicon-nanowire waveguides," Japanese Journal of Applied Physics, Part 1: Regular Papers and Short Notes and Review Papers **44**, 6541-6545 (2005).

132. P. B. Johnson, and R. W. Christy, "Optical constants of the noble metals," Physical Review B **6**, 4370-4379 (1972).

133. G. P. Agrawal, "Nonlinear Fiber Optics, 4th ed," (Academic press, San Diego, 2007).

134. V. Shahraam Afshar, and T. M. Monro, "A full vectorial model for pulse propagation in emerging waveguides with subwavelength structures part I: Kerr nonlinearity," Optics Express **17**, 2298-2318 (2009).

135. M. A. Foster, K. D. Moll, and A. L. Gaeta, "Optimal waveguide dimensions for nonlinear interactions," Optics Express **12**, 2880-2887 (2004).

136. M. D. Turner, T. M. Monro, and S. Afshar V, "A full vectorial model for pulse propagation in emerging waveguides with subwavelength structures part ii: Stimulated Raman Scattering," Optics Express **17**, 11565-11581 (2009).

137. A. V. Shahraam, W. Q. Zhang, H. Ebendorff-Heidepriem, and T. M. Monro, "Small core optical waveguides are more nonlinear than expected: experimental confirmation," Optics Letters **34**, 3577-3579 (2009).

138. I. W. Hsieh, X. Chen, J. I. Dadap, N. C. Panoiu, R. M. Osgood Jr, S. J. McNab, and Y. A. Vlasov, "Cross-phase modulation-induced spectral and temporal effects on co-propagating femtosecond pulses in silicon photonic wires," Optics Express **15**, 1135-1146 (2007).

139. S. Mingaleev, and Y. Kivshar, "Nonlinear photonic crystals toward all-optical technologies," Optics and Photonics News **13**, 48-51+62 (2002).

140. E. Nicoletti, G. Zhou, B. Jia, M. J. Ventura, D. Bulla, B. Luther-Davies, and M. Gu, "Observation of multiple higher-order stopgaps from three-dimensional chalcogenide glass photonic crystals," Optics Letters **33**, 2311-2313 (2008).

141. J. M. Laniel, N. Hô, R. Vallée, and A. Villeneuve, "Nonlinear-refractive-index measurement in As2S3 channel waveguides by asymmetric self-phase modulation," Journal of the Optical Society of America B: Optical Physics **22**, 437-445 (2005).

142. S. Xiao, V. P. Drachev, A. V. Kildishev, X. Ni, U. K. Chettiar, H. K. Yuan, and V. M. Shalaev, "Loss-free and active optical negative-index metamaterials," Nature **466**, 735-738 (2010).

143. A. Antonello, B. Jia, Z. He, D. Buso, G. Perotto, L. Brigo, G. Brusatin, M. Guglielmi, M. Gu, and A. Martucci, "Optimized electroless silver coating for otical and plasmonic applications," Plasmonics (2012).

144. T. Textor, M. M. G. Fouda, and B. Mahltig, "Deposition of durable thin silver layers onto polyamides employing a heterogeneous Tollens' reaction," Applied Surface Science **256**, 2337-2342 (2010).

Author's publications

Journal articles

M. M. Hossain, A. Antonello, and M. Gu, "Experimental demonstrations of propagating plasmons in metallic nanoshells" Optics Express **20**, 17044–17049 (2012).

M. M. Hossain and M. Gu, "Broadband optical absorptions in inversed woodpile metallic photonic crystals", Optical Materials Express **2**, 996-1002, (2012).

M. M. Hossain, M. D. Turner, and M. Gu, "Ultrahigh nonlinear nanoshell plasmonic waveguide with total energy confinement", Optics Express **19**, 23800-23808 (2011).

M. D. Turner, M. M. Hossain, and M. Gu, "The effects of retardation on plasmon hybridization within metallic nanostructures", New Journal of Physics **12,** 083062 (2010).

M. M. Hossain, G. Chen, B. Jia, X. H. Wang, and M. Gu, "Optimization of enhanced absorption in 3D-woodpile metallic photonic crystals", Optics Express **18**, 9048-9054 (2010).

J. Li, M. M. Hossain, B. Jia, and M. Gu, "Rectangular-cavity resonances enhanced absorption in metallic-nanoshelled 2D rod arrays and 3D photonic crystals", New Journal of Physics **12**, 043012 (2010).

J. Li, M. M. Hossain, B. Jia, D. Buso, and M. Gu, "Three-dimensional hybrid photonic crystals merged with localized plasmon resonances", Optics Express **18**, 4491-4498 (2010).

Conference paper

M. M. Hossain, M. D. Turner, and M. Gu, "Ultrahigh nonlinearity in nanoshell plasmonic waveguides", 11th CUDOS workshop, Shoal Bay, Newcastle, NSW, Australia, 31st January - 3rd February, (2012).

M. M. Hossain, M. D. Turner, A. Antonello, and M Gu, "Plasmonic nanostructures for photonic applications", 10th CUDOS workshop, Shoal Bay, Newcastle, NSW, Australia, 14th - 17th February, (2011).

M. M. Hossain, M. D. Turner, B. Jia, and M Gu, "Plasmonic nano-structures for waveguiding with subwavelength confinement", 19th Australian Institute of Physics Congress, Melbourne, Australia, 5th - 9th December, (2010).

M. M. Hossain, B. Jia, and M. Gu, "Optimisation of enhanced absorption in woodpile metallic photonic crystals", 9th CUDOS Workshop, Lake Crackenback, NSW, Australia, 2nd - 5th February, 2010 (2009).

M. M. Hossain, B. Jia, G. Zhou, and M. Gu, "Enhanced absorption in woodpile metallic photonic crystals for modified thermal emission", Australasian Conference on Optics, Lasers and Spectroscopy (ACOLS), Adelaide, Australia, 29th November - 3rd December (2009).

M. M. Hossain, J. Li, D. Buso, B. Jia, G. Zhou, and M. Gu, "Three dimensional metallic photonic crystals towards complete photonic band gap", Nanophotonics Down Under 2009 - Devices and Applications, Melbourne, Australia, 21st - 24th June, (2009).

M. M. Hossain, J. Li, D. Buso, B. Jia, G. Zhou, and M. Gu, "Characterisation of three dimensional metallic photonic crystals from near-infrared to visible", The 8th International Photonic and Electromagnetic Crystal Structures (PECS VIII) Conference, Sydney, Australia, 5th - 9th April (2009).

J. Li, D. Buso, M. M. Hossain, B. Jia, and M. Gu, "Metallodielectric three-dimensional woodpile photonic crystals in the near-infrared wavelength range", The 8th International Photonic and Electromagnetic Crystal Structures (PECS VIII) Conference, Sydney, Australia, 5th - 9th April (2009).

M. M. Hossain, J. Li, D. Buso, B. Jia, G. Zhou, and M. Gu, "All-metallic three-dimensional photonic crystals for telecommunications", 8th CUDOS Workshop, Lake Crackenback, NSW, Australia, 10th - 13th February (2009).

J. Li, D. Buso, M. M. Hossain, B. Jia, and M. Gu, "Realisation of near-infrared three-dimensional metallodielectric photonic crystals", 8th CUDOS Workshop, Lake Crackenback, NSW, Australia, 10th - 13th February (2009).